MAGNETIC, ELECTRICAL AND MAGNETOTRANSPORT PROPERTIES OF CrO_2 and VO_2-BASED THIN FILMS AND HETEROSTRUCTURES

by

XUEYU ZHANG

ARUNAVA GUPTA, COMMITTEE CHAIR

SHANE C. STREET
GREGORY J. SZULCZEWSKI
SHANLIN PAN
PATRICK R. LECLAIR

A DISSERTATION

Submitted in partial fulfillment of the requirements
for the degree of Doctor of Philosophy
in the Department of Chemistry
in the Graduate School of
The University of Alabama

TUSCALOOSA, ALABAMA

2013

Copyright Xueyu Zhang 2013
ALL RIGHTS RESERVED

ABSTRACT

In this dissertation, thin films of two promising rutile oxide materials (CrO_2 and VO_2) are studied. Additionally, magnetic tunnel junctions (MTJs) with these two materials as ferromagnetic (CrO_2) and barrier layer (VO_2) are fabricated and their properties are investigated. The CrO_2 thin films are successfully grown on TiO_2 (001) substrates by atmospheric pressure chemical vapor deposition (APCVD). Their structural and magnetic properties have been examined. The Stoner-Wohlfarth model is used to extract the distribution of the effective anisotropy field in the CrO_2 (001) films for providing a better understanding of the out-of-plane magnetic behavior. The unexpected in-plane magnetic behavior is explained by the possible existence of stripe or vortex domain structures in the films. Besides CrO_2, VO_2 thin films and CrO_2/VO_2 heterostructures have been grown on TiO_2 substrates of different orientations - (100), (110) and (001) - and their electrical and magnetic properties are studied. Finally, MTJs with CrO_2 as the ferromagnetic electrode, heteroepitaxial VO_2 as the barrier layer, and Co as the counter electrode are fabricated, and their transport and magnetic properties are investigated. The bias, temperature and barrier thickness dependence of the tunneling magnetoresistance (TMR) of these CrO_2/VO_2-based MTJs are presented. The Simmons and Brinkman models are used to estimate the barrier height of the tunneling device. In addition, the magnetic behavior of the MTJs at different temperatures is studied.

DEDICATION

This thesis is dedicated to everyone who helped and guided me through the trials and tribulations of creating this manuscript. In particular, my family and close friends who stood by me throughout the time taken to complete this work.

LIST OF ABBREVIATIONS AND SYMBOLS

a, b, c	Lattice constants, unit cell directions
d	Crystal lattice spacing
e	Charge of an electron (1.6×10^{-19} C)
E	Energy
h	Planck's constant (6.626×10^{-34} J·s)
$\hbar$	Reduced Planck's constant (h/2π)
H	Applied magnetic field
H_k	Anisotropy field
H_k^{eff}	Effective anisotropy fields
I	Current
J	Current density
K	Non-shape anisotropy
K_c	Magnteocrystalline anisotropy
K_d	Shape anisotropy
K_{eff}	Mean effective anisotropy
K_s	Surface anisotropy
K_σ	Strain anisotropy

m	Mass of an electron (9.1×10^{-31} kg)
P	Spin polarization
r	Roughness
R_P	Resistance of an MTJ in parallel configuration
R_{AP}	Resistance of an MTJ in anitparallel configuration
V	Voltage
t	Film thickness
θ	Angle of incidence of X-ray beam
θ_c	Critical angle
φ	Barrier height
$\Delta\varphi$	Barrier asymmetry
ρ	Resistivity
σ	Conductivity
ac	Alternating current
AFM	Atomic force microscopy
AMR	Anisotropic magnetoresistance
APCVD	Atmospheric pressure chemical vapor deposition
CDF	Cumulative distribution function
CIP	Current in-plane
CPP	Current perpendicular to plane
dc	Direct current
DOS	Density of states

FM	Ferromagnetic
FWHM	Full width at half maximum
GMR	Giant magnetoresistance
MRAM	Magnetic random access memory
MTJ	Magnetic tunnel junction
PR	Photoresist
PVD	Physical vapor deposition
RF	Radio frequency
SQUID	Superconducting quantum interference device
TMR	Tunnel magnetoresistance
VSM	Vibrating sample magnetometer
XRD	X-ray Diffraction
XRR	X-ray reflectometry

ACKNOWLEDGMENTS

It is my great pleasure to have this opportunity to express my sincere gratitude to everyone who helped me with my research project during my Ph.D. studies. The first person I would like to thank is my advisor, Dr. Arunava Gupta, who introduced me to the field of thin films and spintronics. I benefited a lot from his rich experience and critical thinking regarding film growth and characterization, but more importantly, learned from his sound research attitude and efficient way of analyzing and solving problems. I would like to thank all my committee members, Dr. Patrick R. LeClair, Dr. Shanlin Pan, Dr. Shane C. Street, Dr. Gregory J. Szulczewski, for their suggestions, input and support of both this dissertation and my academic progress. In addition, I would like to give my thanks to Dr. Gary Mankey for his generous help in use of the sputtering system and Dr. Peter Visscher for his guidance in modeling.

I would like to thank all my lab mates and group members: Dr. Krishna Chetry, Dr. Manjit Pathak, Dr. Matthias Althammer, Dr. Karthik Ramasamy, Dr. Ningzhong Bao, Dr. Hideo Sato, Dr. Liming Shen, Dr. Dipanjan Mazumdar, Mr. Ziyou Zhou, Ms. Neha Pachauri, Ms. Archana S. Panikar, Mr. Nariman Naghibolashrafi, Mr. Mehmet Kenan, Ms. Sahar Keshavarz, for all the help and support they provided for my work.

I would like to thank Dr. Alton Highsmith and Mr. John Hawkins, for training me on the characterization equipment and micro-fabrication facility at the MINT Center.

I would like to give my special thanks to my family and friends in China, especially to my husband, Xing Zhong, for their continuous love, encouragement and support.

This work was supported by NSF under Grant No. DMR-0706280.

CONTENTS

ABSTRACT ... ii

DEDICATION ... iii

LIST OF ABBREVIATIONS AND SYMBOLS ... iv

ACKNOWLEDGMENTS ... vii

LIST OF TABLES ... xii

LIST OF FIGURES ... xiii

1. INTRODUCTION ... 1

1.1 Introduction to Spintronics ... 2

1.1.1 History ... 3

1.1.2 Magnetoresistance Effects in Spintronics ... 5

1.1.3 Spintronics Applications ... 8

1.2 Materials for Spintronics Devices ... 10

1.2.1 Chromium Dioxide (CrO_2) ... 11

1.2.2 Vanadium Dioxide (VO_2) ... 13

2. EXPERIMENTAL TECHNIQUES ... 16

2.1 Techniques for thin film deposition and device fabrication ... 16

2.1.1 Atmospheric pressure chemical vapor deposition (APCVD) ... 17

2.1.2 Magnetron Sputtering ... 20

2.1.3 UV-photolithography ... 21

2.1.4 Ion Milling ... 24

2.2 Structural and morphology characterization 25

2.2.1 X-ray diffraction (XRD) and X-ray reflection (XRR) 26

2.2.2 Atomic force microscopy (AFM) 28

2.3 Magnetic measurements 29

2.3.1. Vibrating sample magnetometer (VSM) 30

2.3.2. Alternating gradient magnetometer (AGM) 31

2.3.3. Superconducting quantum interference device (SQUID) 32

2.4 Transport property measurements 34

3. CrO_2 THIN FILMS ON (001)-ORIENTED TiO_2 SUBSTRATES 36

3.1 Introduction 36

3.2 Structures of CrO_2 thin films on TiO_2 (001) substrates 37

3.3 Magnetic properties of CrO_2 thin films on TiO_2 (001) substrates 40

3.4 Conclusion 47

4. VO_2 THIN FILMS AND CrO_2/VO_2 HETEROSTRUCTURES ON (100), (110) AND (001)-ORIENTED TiO_2 SUBSTRATES 49

4.1 Introduction 49

4.2 VO_2 thin films on (100), (110) and (001)-oriented TiO_2 substrates 50

4.3 CrO_2/VO_2 heterostructures on (100), (110) and (001)-oriented TiO_2 substrates 55

4.4 Conclusion 58

5. SPIN TRANSPORT IN CrO_2-Based MAGNETIC TUNNEL JUNCTIONS 60

5.1 Introduction 60

5.2 Device fabrication 61

5.3 Spin transport in CrO_2/Cr_2O_3/Co junctions 64

5.4 Spin transport in CrO_2/VO_2/Co junctions 67

5.4.1. TMR 67

5.4.2. Barrier height 71

5.4.3. M-H loops 77

5.5 Conclusion 78

6. SUMMARY 80

REFERENCES 85

LIST OF TABLES

Table 1. Comparison of the metal-insulator-transition properties of differently oriented VO_2 thin films of 30 nm thickness 55

Table 2. Lattice parameters of Rutile VO_2, CrO_2 and TiO_2 materials 56

Table 3. Comparison of film roughness and magnetization of CrO_2/VO_2 structures on (100), (110) and (001)-oriented TiO_2 substrates 58

LIST OF FIGURES

Figure 1. Giant magnetoresistance of Fe/Cr multilayers with various thickness of Cr at 4.2 K 4

Figure 2. Principles of GMR (when nonmagnetic layer is metallic) and TMR (when nonmagnetic layer is insulating) effects in (a) Parallel alignment and (b) Antiparallel alignment. 6

Figure 3. Current-in-plane (CIP) and current-perpendicular-to-the-plane (CPP) geometries of GMR structures 7

Figure 4. (a) Structure of a simple spin valve and (b) Structure of a spin valve with a synthetic antiferromagnet 8

Figure 5. Schematic of a simplified MRAM structure 9

Figure 6. Unit cell of chromium dioxide (CrO_2) crystal 12

Figure 7. DOS of CrO_2 for (a) Majority spin and (b) Minority spin electrons 13

Figure 8. Metal-insulator-transition (MIT) of VO_2 14

Figure 9. Schematic diagram of the APCVD system 18

Figure 10. Deposition rate of CrO_2 thin film on TiO_2 (001) substrate. The dotted line is a guide to the eye 19

Figure 11. Working principle of magnetron sputtering 21

Figure 12. Dry etching using (a) Positive photoresist and (b) Negative photoresist during a photolithography process 23

Figure 13. Working principle of ion milling 25

Figure 14. Schematic drawing of X-ray diffractometer 26

Figure 15. (a) Schematic drawing for the principles of Bragg's Law and (b) An example of XRD plot of a CrO_2 (001) film on TiO_2 substrate. 27

Figure 16. (a) Schematic drawing illustrating the principles of XRR and (b) An example of XRR plot of a Co film of 50 nm thickness on SiO_2 substrate 28

Figure 17. (a) Schematic drawing of AFM system and (b) An example of AMF image of a VO_2 film on TiO_2 (001) substrate (tapping mode is used and image size is 2×2 μm) 29

Figure 18. Schematic drawing of VSM system. 31

Figure 19. Schematic drawing of AGM system. 32

Figure 20. Schematic drawing of the SQUID magnetometer 33

Figure 21. Schematic drawing of home-made transport measurement system 34

Figure 22. (a) Diagram of four-point probe methods for a measurement junction and (b) Electrical circuit diagram of four-point probe method 35

Figure 23. (a) XRD patterns using Cu K-α radiation of CrO_2 (001) films with various thicknesses from 20 to 250 nm. (b) Off-axis XRD patterns for (101) peaks from the film and the substrate. Dotted lines represent the bulk 2θ peak positions for CrO_2 (002) and (101) planes. No peaks observed for 2θ angles are omitted from the plot. (c) ϕ-scan of a 100 nm film when it is tilted to sample the (101) planes 39

Figure 24. Reduced magnetization-field (H-M) curves when the external field is applied out-of-plane for CrO_2 (001) thin films of various thickness from 13 nm to 250 nm 40

Figure 25. Extracted (dots) and fitted (lines) CDF curves of various thicknesses from 13 nm to 250 nm 42

Figure 26. Saturation moment of CrO_2 (001) films as a function of thickness 43

Figure 27. Extracted (dots) and fitted (lines) non-shape anisotropy constants for CrO_2 (001) films of various thickness from 13 to 250 nm 45

Figure 28. Reduced magnetization-field (H-M) curves when the external field is applied in-plane of CrO_2 (001) thin films with various thickness from 13 nm to 250 nm 47

Figure 29. XRD patterns of VO_2 film on (a) (100), (b) (110) and (c) (001) TiO_2 substrates 51

Figure 30. AMF image of VO_2 films on (a) (100), (b) (110) and (c) (001) TiO_2 substrate. The three different oriented films have the same thickness of about 30 nm 52

Figure 31. Roughness as a function of film thickness for VO_2 thin films on TiO_2 substrates with various orientations. 53

Figure 32. Resistance as a function of temperature of VO_2 thin films on (a) (100), (b) (110) and (c) (001) TiO_2 substrates. The thickness of all films is about 30 nm 54

Figure 33. Magnetic hysteresis loops of CrO_2/VO_2 bilayer structures on (a) (100), (b) (110) and (c) (001) TiO_2 substrates. The thickness of CrO_2 layer for all bilayer structures is about 50 nm. 57

Figure 34. The fabrication process of the CrO_2-based MTJs (a) Growth of bottom electrode, (b) Define of junction and (c) Growth of top electrode 63

Figure 35. Temperature dependence of the bottom electrode resistance for $CrO_2(110)/Cr_2O_3/Co$ junction. 64

Figure 36. Temperature dependence of the junction resistance in a 8×8 μm^2 $CrO_2(110)/Cr_2O_3/Co$ junction. 65

Figure 37. TMR of a 8×8 μm^2 $CrO_2(110)/Cr_2O_3/Co$ junction measured at 78 K. 66

Figure 38. Bottom electrode and junction resistance of CrO_2/VO_2 (4.5 nm)/Co MTJ as a function of temperature. The insert shows a resistance drop around 340 K 68

Figure 39. TMR of CrO_2/VO_2 (4.5 nm)/Co junction (8×8 μm^2) with applied voltage of (a) 0.4 mV and (b) 340 mV 69

Figure 40. Bias dependence for a MTJs of 8×8 μm^2 with 4.5 nm epitaxial VO_2 barrier, at T=78 K 70

Figure 41. Temperature dependence for MTJs of 8×8 μm^2 with 4.5 nm epitaxial VO_2 barrier, for V<0.5 mV 71

Figure 42. Thickness dependence of TMR in $CrO_2/VO_2/Co$ MTJs (8×8 μm^2), measured at 78 K with 1 mV bias voltage. The error bars represent the uncertainty of thickness obtained from XRR measurement and junction resistance from R-T measurement. 72

Figure 43. Schematic energy diagram with barrier height φ, barrier asymmetry Δφ and barrier thickness d 73

Figure 44. Simmons fitting of the current density against the bias voltage of a 8×8 μm^2 junction 74

Figure 45. Brinkman fitting of the current against the bias voltage of a 8×8 μm^2 junction 76

Figure 46. Brinkman fitting of the conductance against the bias voltage a 8×8 μm^2 junction......77

Figure 47. Hysteresis loops of $CrO_2/VO_2/Co$ junction at different temperatures..........................78

CHAPTER 1

INTRODUCTION

Dating back to the 4th century BC, magnetic materials have been utilized by mankind for centuries. However, people had not realized that magnetism is closely related to the angular momentum (spin) of electrons until the early 20th century (Uhlenbeck and Goudsmit in 1925). Furthermore, spintronics (aka magnetoelectronics) did not become a hot topic in both research and industry field until the late 1980s, when giant magnetoresistance (GMR) was discovered.[1-4] Compared with conventional electronics that focus on the manipulation of the charge of electrons, spintronics can provide new device functionalities through control of the electron spin. By applying external electrical and magnetic fields, the control of both spin and charge dynamics can be realized in spintronics. However, the performance of spintronics devices greatly relies on the degree to which the electron spins are aligned in a particular direction (spin polarization). Spin polarized electrons can be generated by either traditional optical techniques or the newly adopted electrical spin filtering method, which is more favorable for device applications. The general goal of spintronics is to fabricate high-performance devices that are not feasible with conventional electronics, and then study their transport properties on the basis of understanding the interaction between the particle spin and its solid-state environment.[5-8]

Presently, the most common spintronic devices are based on magnetic tunnel junctions (MTJs). They are basically a type of highly sensitive magnetic field detector and their basic

structure is a thin insulating tunnel barrier sandwiched between two ferromagnetic electrodes. The resistance of MTJs is strongly dependent on the relative magnetization directions of the two electrodes.[9,10] In addition, the choice of the barrier layer and the interactions between the barrier layer and electrodes also play an important role in determining the transport properties and the efficiency of the constructed spintronics devices. To achieve desirable properties and high efficiency of spintronics devices, a range of insulator and semiconductor materials have been considered as barrier layer in the fabrication of devices.[6,11]

The objective of this dissertation is to conduct fundamental studies of the properties of chromium dioxide (CrO_2) and vanadium dioxide (VO_2), which are considered to be desirable bottom electrode and barrier layers, respectively, in spintronics devices. In addition, magnetic tunnel junctions are fabricated based on these oxide materials and their magnetotransport properties will be investigated.

1.1 Introduction to Spintronics

Spintronics is a multidisciplinary field involving various areas such as magnetism, semiconductor physics, optics and superconductivity. Over the past decades, the field of spintronics has experienced very rapid development. The principles underlying spintronic devices have been actively studied and their commercial applications have been realized in recent years.[6,12-14] In this section, the history of spintronics will be briefly reviewed and the two most important and widely used effects in spintronics (Giant Magnetoresistance and Tunneling Magnetoresistance) will be presented. In addition, several important spintronics

applications, such as spin valve and magnetoresistive random-access memory (MRAM), will be discussed.

1.1.1 History

In 1936, Mott developed a two current model of conductivity for transition metals, which provided a basic understanding of the resistance of ferromagnetic metals.[15] In his theory, the spin-up electrons and spin-down electrons do not mix with each other in scattering processes if the temperature remains sufficiently low. The net current is the sum of these two independent electron currents with different spin orientations that gives the net current and leads to a spin polarized current in ferromagnetic metals. This theory showed a direct connection between the magnetic properties and the electrical conductivity. Following Mott's research, Valet and Fert modified this two current model further by taking into account the interactions between adjacent interfaces and provided an explanation of various magnetoresistive phenomena in magnetic multilayers.[16] They also calculated the separate volume and interface contributions to the spin-dependent scattering using magnetoresistance data.

The discovery of giant magnetoresistance (GMR) effects in 1988 opened the door to new exploration of the spintronics field and immediately triggered much attention on the transport properties of magnetic multilayers. GMR effects were first observed in Fe/Cr multilayers by the group of Albert Fert [3] and in Fe/Cr/Fe trilayers by the group of Grunberg [17]. The giant magnetoresistance of Fe/Cr multilayers with various thicknesses of Cr is shown in Fig. 1. The resistance of the system changes with the direction of the magnetic moments in the ferromagnetic layers. The system has the lowest resistance when the magnetic moments in ferromagnetic layer are aligned, while it shows the highest resistance when the moments are anti-

aligned. The realization of a large GMR effect at room temperature by Parkin *et al*. [12], using simple sputtering method, had a significant influence in turning fundamental studies to practical applications in various fields, such as magnetic recording, spin valve and galvanic isolator. A detailed review of GMR will be given in section 1.1.2.

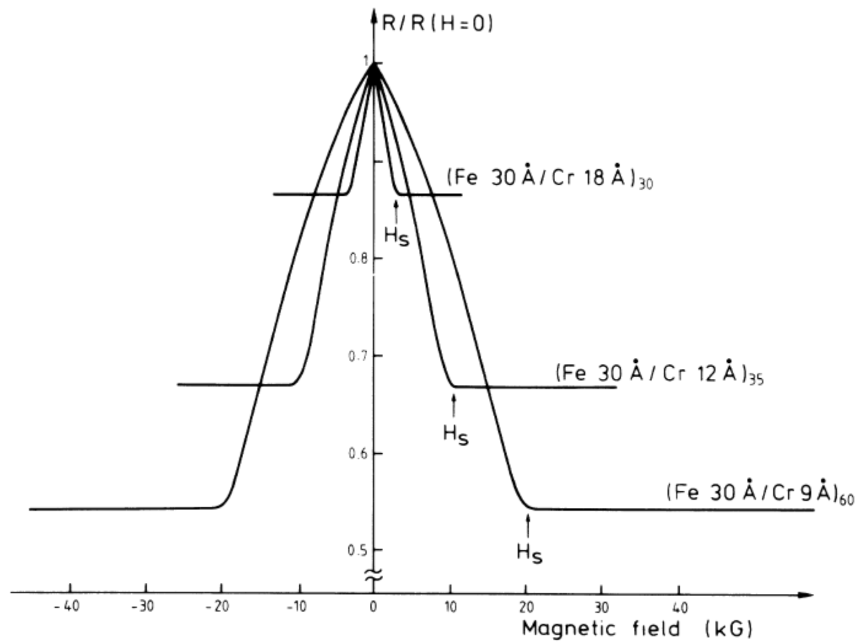

Figure 1. Giant magnetoresistance of Fe/Cr multilayers with various thickness of Cr at 4.2 K. Reproduced with permission from ref. [3].

Another important milestone in spintronics development is the discovery of tunneling magnetoresistance (TMR). In 1975, Julliere's group [18] discovered the TMR effect for the first time. The resistance in their Fe/Ge-O/Co junctions showed a 14% change at 4.2 K with a change in relative magnetization of the magnetic electrodes. Later, Miyazaki's group [19] and Moodera's group [9] adopted a Fe/Al_2O_3/Fe junction and successfully realized a TMR effect of about 18% at room temperature, which indicated a potential for practical use and therefore attracted much attention to this emerging field. Since 2004, magnesium oxide (MgO) has become a popular material used as tunnel barrier in TMR junctions due to their possible high

TMR effect over few hundred percent, which was first theoretically predicted by Butler and Mathon's groups.[20,21] In 2001, Bowen [22] reported a significant TMR effect shown in their Fe/MgO/FeCo junctions and experimentally proved the prediction of its high TMR effect. In 2004, the Fe/MgO/Fe junctions with over 200% TMR at room temperature were fabricated by Yuasa *et al*. [23] and Parkin *et al* [24]. At present, room temperature TMR effect of up to 600% has been realized by Ikeda's [25] group in their CoFeB/MgO/CoFeB junctions. A detailed review of TMR will be provided in 1.1.2.

1.1.2 Magnetoresistance Effects in Spintronics

Both giant magnetoresistance (GMR) and tunneling magnetoresistance (TMR) effects are quantum mechanical phenomena and are of great importance to the development of spintronics. In the current perpendicular to the plane (CPP) geometry, GMR and TMR devices in their basic form have similar sandwich structures that consist of two ferromagnetic layers separated by a nonmagnetic layer. The electrical resistance of these structures can change significantly with relative magnetization orientation of the ferromagnetic layers. If the magnetization is in a parallel alignment, the resistance of the structure is low. On the other hand, if the magnetization is in an antiparallel alignment, the structure goes to a high resistance state. The effect is called GMR when the thin spacer layer is metallic, while it is called TMR when a very thin insulating layer is used as a barrier layer in the structures. The underlying principles of GMR and TMR effects are shown in Fig. 2.

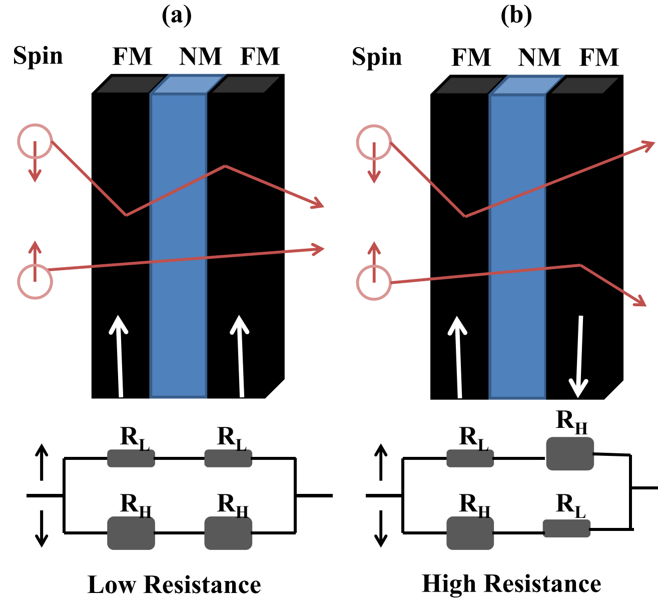

Figure 2. Principles of GMR (when nonmagnetic layer is metallic) and TMR (when nonmagnetic layer is insulating) effects in (a) Parallel alignment and (b) Antiparallel alignment.

The magnetoresistance ratio for both GMR and TMR effects is defined by the resistance of the two configurations as:

$$GMR(TMR) = \frac{R^{P} - R^{AP}}{R^{P} + R^{AP}} \tag{1.1}$$

where R^P is the resistance of the system for parallel configuration and R^{AP} is the resistance of the system for antiparallel configuration.[18,26]

Besides CPP geometry, GMR devices can also be implemented to have current in the plane (CIP), as shown in Fig. 3.

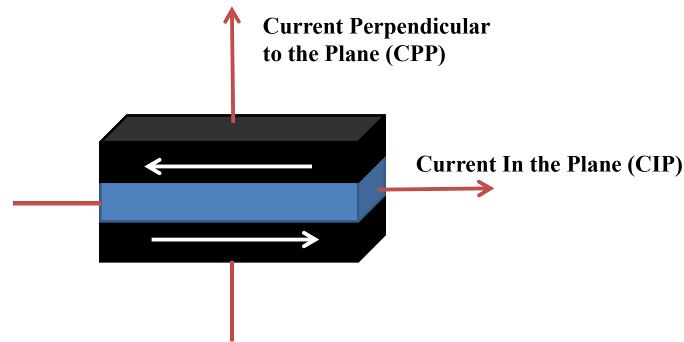

Figure 3. Current-in-plane (CIP) and current-perpendicular-to-the-plane (CPP) geometries of GMR structures.

Many of the current GMR applications use the CIP configuration since it is easier to realize in practice as compared to CPP configuration. However, the CPP configuration is theoretically desirable in spintronics devices since it can result in much larger GMR effects, and relates more closely to the physics of GMR effects.

Another important magnetoresistance effect in spintronics devices is TMR. A TMR device can be considered as an extension of CPP GMR device, in which the electrons tunnel across a very thin insulating barrier layer and travel from one electrode to another. The tunneling resistance varies depending on the relative magnetic orientations of the ferromagnetic electrodes. Through recent studies, the TMR effect has been demonstrated to achieve a larger magnetoresistance than GMR effect and has potential applications in magnetic memory devices.

The TMR effects can be rudimentarily understood by Julliere's model that is based on two assumptions[18]:

(1) Spin orientation of electrons is conserved during the tunneling process. This means the electrons of one particular spin state only tunnel to the unfilled spin states of the same spin

orientation. The spin-dependent tunneling can be considered to have two independent channels for up- and down-spin electrons.[27]

(2) The conductance of each channel is proportional to the product of the density of states (DOS) of the two ferromagnetic electrodes.[27]

Therefore, the magnetoresistance ratio of TMR systems can be calculated as:

$$MR = \frac{2P_1P_2}{1 - P_1P_2} \tag{1.2}$$

where P_1 and P_2 are the spin polarization of electrons in the two ferromagnetic electrodes defined by the difference in DOS of up-spin ($D_\uparrow$) and down-spin ($D_\downarrow$) electrons:

$$P = \frac{D_\uparrow - D_\downarrow}{D_\uparrow + D_\downarrow} \tag{1.3}$$

1.1.3 Spintronics Applications

The magnetoresistance effect in spintronics can be utilized in many fields, such as magnetic sensors, spin valves, magnetic read heads in hard drives, and nonvolatile magnetic random access memory. [26,28,29]

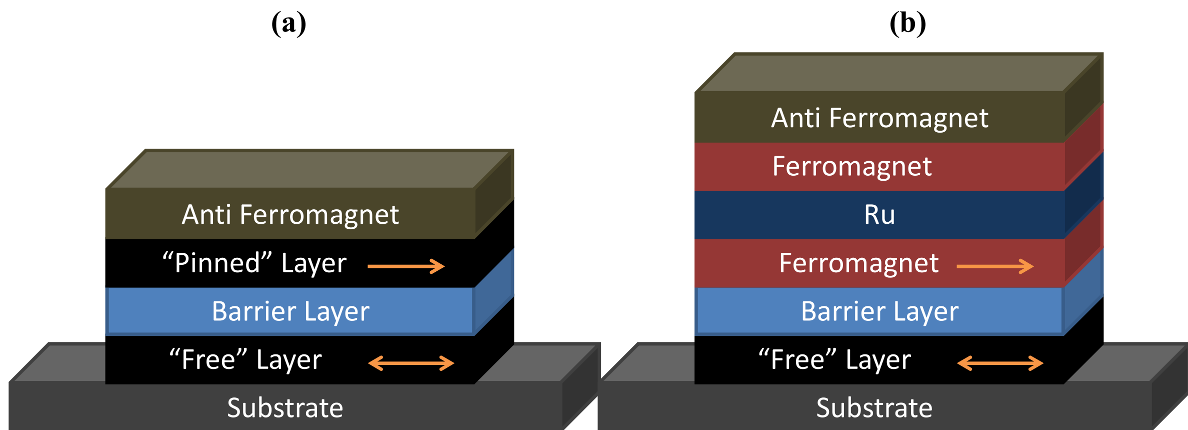

Figure 4. (a) Structure of a simple spin valve and (b) Structure of a spin valve with a synthetic antiferromagnet.

Spin valve is one of the most important applications of spintronics. A spin valve is a GMR-based device that has a sandwich structure consisting of two ferromagnetic layers and a nonmagnetic layer.[30] The structure of a typical spin valve is shown in Fig. 4 (a). One of the ferromagnetic layers is "pinned", in which the magnetization orientation is fixed and cannot be easily changed with the applied magnetic field. Another layer is "free", in which the magnetization orientation is sensitive to a small magnetic field. To further improve the efficiency of the spin valve, two methods are usually utilized. The first method is to use an antiferromagnetic layer, or a synthetic antiferromagnetic layer, to provide more effective pinning. In this way, the interface between the antiferromagnetic layer and one of the ferromagnetic layers can help to resist magnetization changes for one field direction for an antiferromagnetic layer or both for a synthetic antiferromagnetic layer. A synthetic antiferromagnet, which has a nonmagnetic conductor such as ruthenium (Ru) to separate the two magnetic layers with antiparallel magnetization, is shown in Fig. 4(b). [31] The synthetic antiferromagnet is less sensitive to the applied field than a simple pinned layer and can help the structures to achieve higher magnetoresistance changes. The second method is to form a nano-oxide layer (NOL) at the surface of the magnetic layer. The surface scattering of a NOL layer can effectively reduce the background resistance and thus increase the magnetoresistance change of the device.[32]

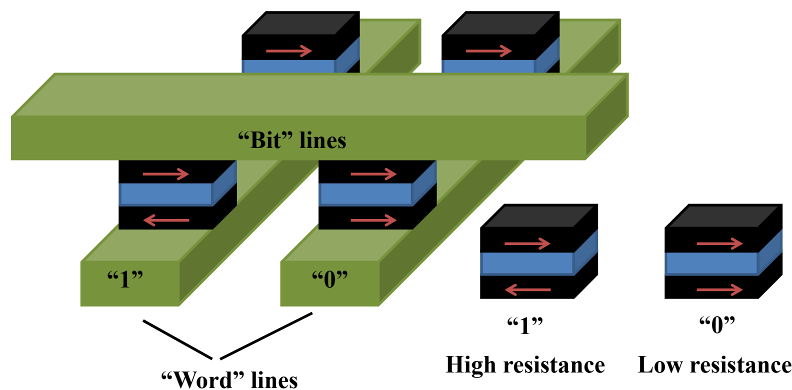

Figure 5. Schematic of a simplified MRAM structure.

A variant of the spin valve used in hard drives is the magnetoresistive random-access memory (MRAM). MRAM cell works as a spin valve to store information. As compared to conventional RAM, MRAM offers the advantages of faster writing times, lower energy for writing and higher writing endurance. A simplified MRAM cell structure is shown in Fig. 5. The data reading of MRAM can be realized by detecting electrical resistance changes of the cell that result from the magnetization orientations of the two ferromagnetic layers. When magnetizations of the two magnetic layers have the same orientation, the resistance of the cell is low and the resulting current is high. This is considered as the “1” state of the cell. On the other hand, the cell is assigned as the “0” state when the magnetizations have opposite orientations and the resistance of the system is high. For data written in MRAM, a current passes through a pairs of write lines arranged at right angles to each other and produces an induced magnetic field at specific cells to change the orientation of the magnetic layers. However, a major drawback of MRAM is potential false writes due to the overlaps of induced field over a small area. To avoid this problem, a new technology referred to as spin transfer torque (STT) has been developed. By transferring a torque to the nearby layer, STT can significantly reduce the amount of current required during the write process and thus decrease the chances of false writes. [33]

1.2 Materials for Spintronics Devices

The search for materials remains a challenge in the development of spintronics devices. The materials used for ferromagnetic layers and barrier layers play a very important role in determining the performance and functionality of the fabricated spintronics devices. For practical usage, a favorable ferromagnetic material would be highly spin polarized and have a Curie temperature above room temperature. On the other hand, a barrier layer needs the material to

have unique properties that may offer new functionality to the device and be able to integrate with the ferromagnetic layer as well to improve the device performance. In this section, we will discuss two promising candidates for ferromagnetic layers and barrier layers, chromium dioxide and vanadium dioxide, respectively.

1.2.1 Chromium Dioxide (CrO_2)

When considering materials with high spin polarization, half-metals are attractive due to their unusual electronic structures and properties. A half metal works as a metal for electrons of one spin orientation and its spin bands are intercepted by the Fermi level, while it acts as a semiconductor or insulator for electrons of the opposite spin orientation and has a band gap at the Fermi level.

There are several types of half-metals, including oxides, sulfides and Heusler alloys. As compared to other types, the ferromagnetic oxides tend to have simpler crystal structure. [34-36] Chromium dioxide (CrO_2) is one of the most widely studied oxide half-metals. It has a tetragonal rutile structure as shown in Fig. 6. Each oxygen atom is surrounded by three chromium atoms and each chromium atom is octahedrally coordinated by eight oxygen neighbors. There are two short apical bonds (0.189 nm) and four longer bonds (0.191 nm) connecting chromium and oxygen atoms. The space group of CrO_2 is *P*42/mnm and the lattice parameters are a=b=0.4422 nm and c=0.2917 nm.

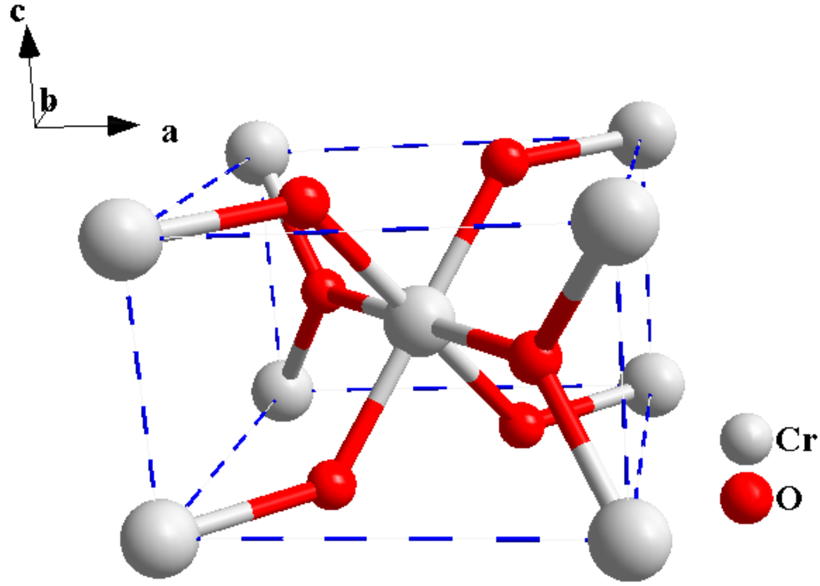

Figure 6. Unit cell of chromium dioxide (CrO_2) crystal.

The density of states of CrO_2 for both majority and minority spins are illustrated in Fig. 7.[37] As expected, the Fermi level intercepts the spin band for majority spins (spin up), while there is a band gap of about 1.8 eV for minority spins (spin down). By taking DOS of the spin up electrons at Fermi level as 1 and DOS of spin down electrons as 0, the spin polarization of CrO_2 can be theoretically calculated as high as about 100%:

$$P = \frac{D_{\uparrow} - D_{\downarrow}}{D_{\uparrow} + D_{\downarrow}} = \frac{1-0}{1+0} = 100\% \tag{1.4}$$

This almost complete spin polarization of CrO_2 near the Fermi level has already been experimentally confirmed, at least for low temperatures. [38-40] Using Julliere's model, we can expect that the magnetoresistance of structures with CrO_2 as ferromagnetic layer can ideally be very large:

$$MR = \frac{2P_1P_2}{1-P_1P_2} = \frac{2\times100\%\times100\%}{1-100\%\times100\%} = \infty \tag{1.5}$$

where we assume using CrO_2 for both ferromagnetic layers, thus P_1=100% and P_2=100% .

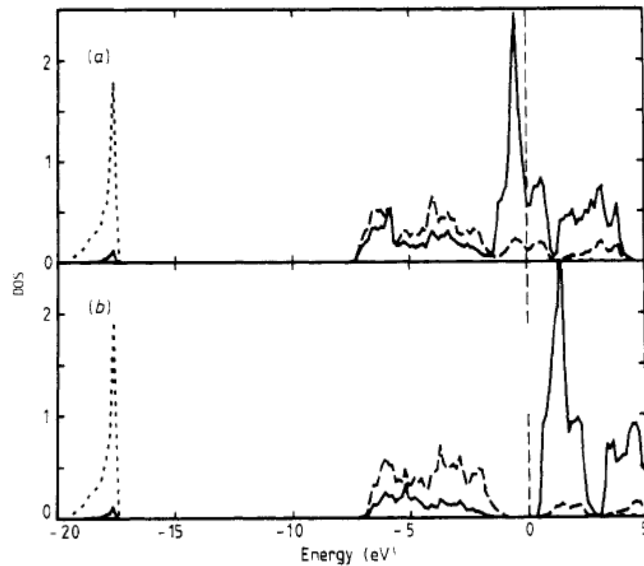

Figure 7. DOS of CrO_2 for (a) Majority spin and (b) Minority spin electrons Reproduced with permission from ref. [37].

This unique property, together with its relatively high Curie temperature (398K), makes CrO_2 an ideal material for use as a ferromagnetic layer in spintronics devices and a model system for investigating half-metals.

1.2.2 Vanadium Dioxide (VO_2)

A range of insulator and semiconductor materials such as MgO, Al_2O_3 and Ge, have been utilized as the barrier layer in spintronics devices. Among the candidate insulator and semiconductor barrier materials, vanadium dioxide (VO_2) is amazingly versatile due to its unique structural transformation and metal-insulator transition (MIT) as a function of temperature. In the bulk, at temperatures > 68°C, VO_2 has a rutile tetragonal structure (*R* phase) in which each vanadium atom is located at the center of an oxygen octahedron. At lower temperatures, the VO_2 structure changes due to a monoclinic distortion (M_1 phase) of the rutile form (distorted rutile).

Along the rutile C_r axis, the alternate vanadium cations are paired, with shorter distances between pairs of V cations because of metal-metal bonding. The MIT of VO_2 is shown in Fig. 8.

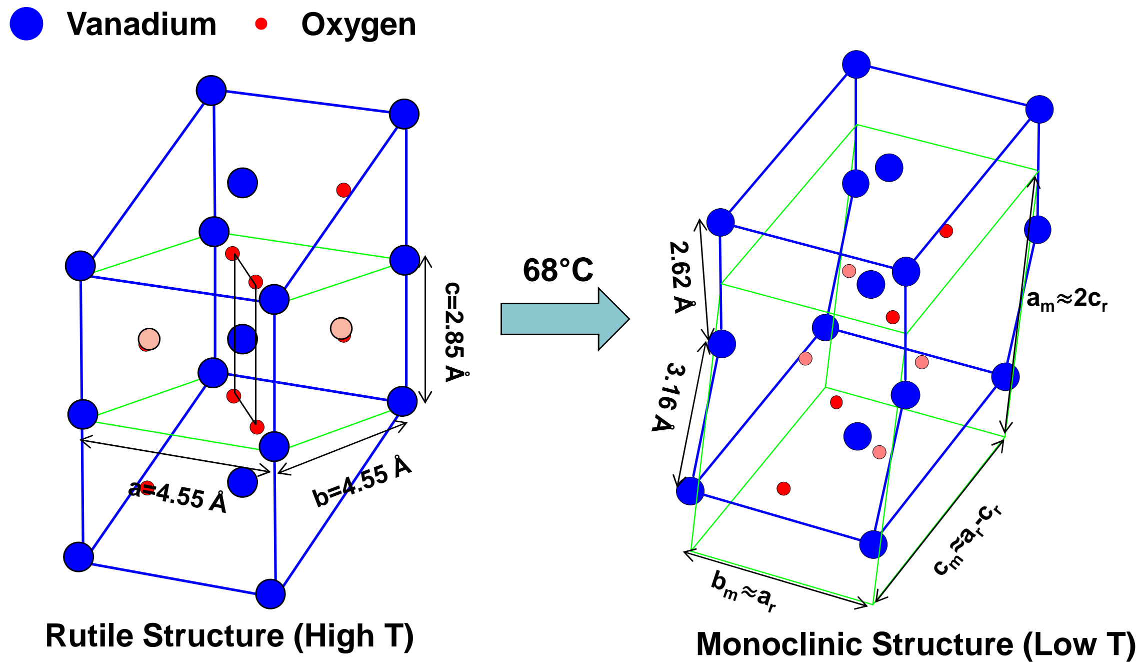

Figure 8. Metal-insulator-transition (MIT) of VO_2.

As the crystal structure changes from the *R* phase at high temperature to the M_I phase at low temperature, there are significant changes in both the electronic and optical properties of VO_2. [41,42] The *R* phase of VO_2 is a good conductor, while the M_I phase is an insulator in which the charge gap at the Fermi energy is about 0.7 eV. Typically, bulk VO_2 single crystals display a MIT at a transition temperature of 68°C with a transition width of only a few degrees. [41,43] During the MIT, as much as five orders of magnitude change in electrical resistivity and three orders of magnitude change in infrared transmission can be observed. [43-45]

In addition, both the rutile and the monoclinic phases of VO_2 are structurally compatible with the ferromagnetic rutile oxide CrO_2 due to their similar unit-cell lattice parameters. Since a phase transformation and significant transport property changes occur across the MIT of VO_2, it can be potentially used as a unique barrier layer in TMR and/or CPP-GMR devices. Accompanied with the large change in the resistance of the VO_2 barrier layer at the transition temperature, a change in the magneto-transport characteristics from TMR to CPP-GMR is expected. This desirable feature of VO_2 could lead to new effects to be exploited for storage and memory devices. The most important attributes of such devices that use VO_2 as the barrier layer are their potentially high operation speed and low power consumption, since ultrafast switching of VO_2 thin film between the conducting and insulating states can occur in the device with only a small temperature change.[46,47]

In this dissertation, we will investigate these two promising materials for MTJs. The structural and magnetic properties of CrO_2 thin films on TiO_2 substrates will be discussed in chapter 3. In addition, the electrical and magnetic properties of VO_2 thin films and CrO_2/VO_2 heterostructures on TiO_2 will be presented in chapter 4. Finally, the fabrication and transport properties of MTJs with CrO_2 bottom electrodes and VO_2 barrier layers will be investigated in chapter 5.

CHAPTER 2

EXPERIMENTAL TECHNIQUES

In this chapter, the experimental techniques used in this dissertation and their working principles are briefly discussed. The relevant techniques can be categorized as:

(1) Thin film deposition and device fabrication: CrO_2 and VO_2 films are deposited by atmospheric pressure chemical vapor deposition (APCVD) method. Cobalt (Co), ruthenium (Ru) and silicon dioxide (SiO_2) films are deposited by magnetron sputtering as top electrode and insulation layers, respectively. The MTJs are patterned by UV-photolithography and etched by ion milling.

(2) Lattice structural and surface morphology characterization: the lattice parameters, film epitaxy and film thickness are measured by X-ray diffraction and reflectivity (XRD and XRR). The grain features and surface roughness of the films are examined by atomic force microscopy (AFM).

(3) Magnetic properties measurements: the hysteresis loops of CrO_2 films and CrO_2/VO_2-based heterostructures are measured by vibrating sample magnetometer (VSM), alternating gradient magnetometer (AGM) and superconducting quantum interference device (SQUID).

(4) Electrical transport properties measurement: resistance vs. temperature, resistance vs. field and current vs. voltage.

2.1 Techniques for thin film deposition and device fabrication

In this section, experimental techniques involved in our film deposition and device fabrication are discussed. Chemical vapor deposition techniques for CrO_2 and VO_2 thin film growth at atmospheric pressure are introduced. The top electrodes and insulating barriers are deposited by magnetron sputtering method, whose working principle is also reviewed. In addition, micro-fabrication methods used to fabricate micron-scale junctions, including UV-photolithography and ion milling, are introduced and the critical instrument parameters of our tools are reported.

2.1.1 Atmospheric pressure chemical vapor deposition (APCVD)

Atmospheric pressure chemical vapor deposition (APCVD) is a simple but powerful technique for the growth of thin films with high quality. It is relatively inexpensive to set up an APCVD system since no high vacuum or other sophisticated equipment are needed. In addition, this method can work for a large variety of materials and is widely used in the semiconductor industry.[48] Our home-built APCVD system for CrO_2 and VO_2 thin film deposition is shown schematically in Fig. 9. This system has two heating zones, the temperatures of which can be independently controlled by separate ovens. One of the ovens is used for evaporating the precursor while the other one is used for providing the optimal substrate temperature for film deposition. The thermally activated chemical reaction results in film deposition and oxygen is used as the carrier gas to bring the precursor vapor to the substrate zone and as the oxidation source.[49]

In the case of CrO_2 deposition, the CrO_2 films are grown on TiO_2 substrates with different crystalline orientations using CrO_3 as precursor. The deposition condition for CrO_2 (001) films

are similar as the ones for CrO_2 (100) and (110) films, which have been reported by Miao et al.[50] The films are grown at about 400°C substrate temperature, while maintaining the precursor at about 260°C. During deposition, a 100 sccm oxygen flow transports the sublimed CrO_3 vapor from the precursor zone to the substrate zone, where the vapor decomposes on the substrate and form CrO_2 thin film with the evolution of O_2. The CrO_2 (001) film grows slowly for the first 15 minutes due to nucleation and lateral diffusion limitations and subsequently deposits at a linear rate of about (5.2±0.2) nm/min, as shown in Fig. 10. The error bars in the figure represent the uncertainty of the thicknesses obtained from the X-ray reflection measurements.

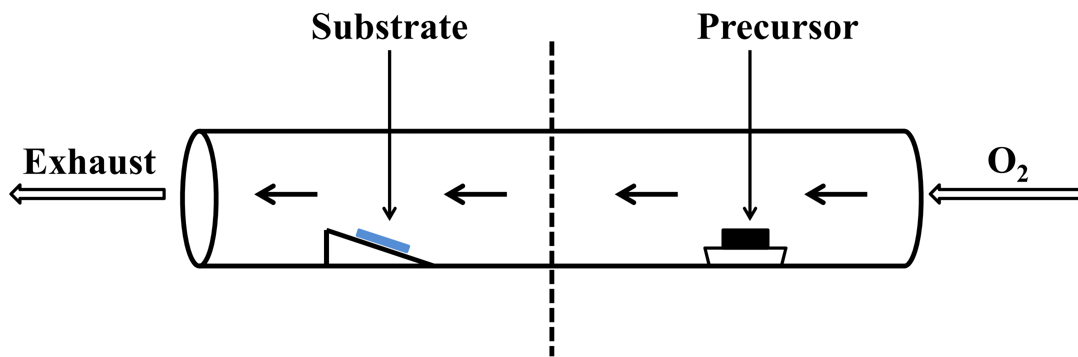

Figure 9. Schematic diagram of the APCVD system.

For VO_2 film deposition, the substrate in the deposition chamber is placed on a heater block with independent temperature control. The optimal heater (deposition) temperature for growth of VO_2 films on (100), (110) and (001)-oriented TiO_2 substrates has been determined to be about 380°C-450°C. Oxygen is again used as the carrier gas that transfers the vapor precursor to the deposition chamber. The flow rate of oxygen is maintained at 200 sccm for (100), (110) and

(110)-oriented VO_2 film deposition. A metal-organic precursor vanadyl-acetylacetonate ($VO(acac)_2$) is chosen as the precursor. Compared to other precursors, such as vanadium(IV) tetrachloride (VCl_4) and vanadium(V) oxytrichloride ($VOCl_3$), $VO(acac)_2$ has three advantages.[51] Firstly, $VO(acac)_2$ is much less toxic and corrosive than other precursors. Secondly, it does not require a separate oxidant during the deposition. In addition, it can more readily form high purity VO_2 thin films without residual carbon contamination.

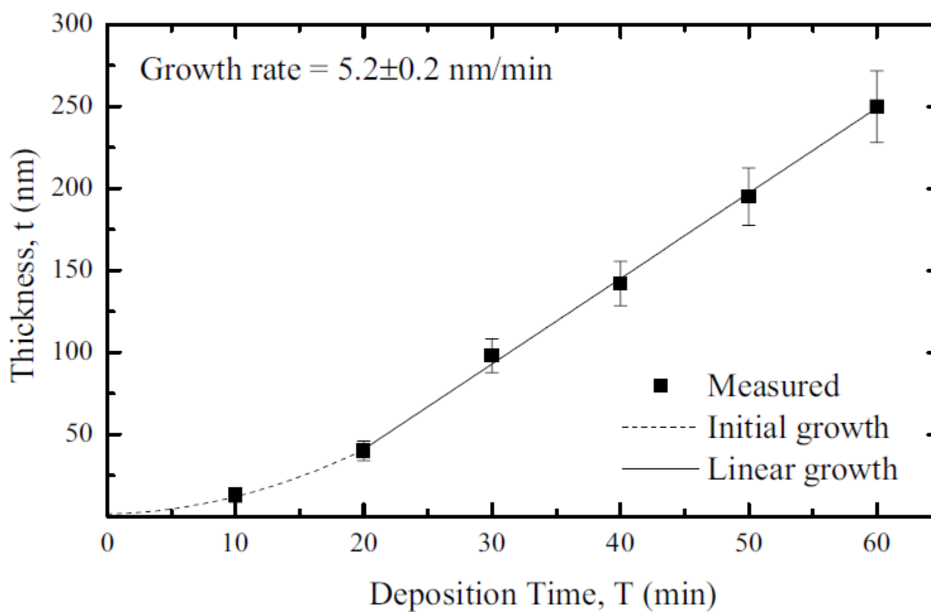

Figure 10. Deposition rate of CrO_2 thin film on TiO_2 (001) substrate. The dotted line is a guide to the eye.

It is also worth noting that CrO_2 film deposition is very sensitive to the substrate surface condition. The TiO_2 substrate must be cleaned very carefully, otherwise film quality is compromised. Prior to the deposition of both CrO_2 and VO_2 films, the TiO_2 substrates are ultrasonically cleaned using organic solvents such as acetone and isopropanol, and then treated with 20% dilute hydrofluoric acid to remove any possible impurities on the surface.

2.1.2 Magnetron Sputtering

Magnetron sputtering is a physical vapor deposition (PVD) method used to deposit thin films. As compared to chemical vapor deposition methods, physical vapor deposition methods such as sputtering can easily deposit materials with very high melting points and the sputtered materials can adhere well to the substrates. This sputtering technique is also very compatible with high vacuum applications, which makes it possible to deposit thin films of high structural and compositional quality. However, this method is much more complex than chemical vapor deposition method since the deposition process can be influenced by many factors. Another drawback of the sputtering method is that it may introduce contamination since it is difficult to control where the target atoms go and the inert sputtering gases may be incorporated into the deposited film as impurities. Moreover, it is difficult to replicate the film stoichiometry of multi-component materials from a target of specific composition.

The working principle of magnetron sputtering is shown in the Fig. 11. With high voltage and low pressure, inert sputtering gas molecules such as argon (Ar) are ionized into electrons and positive ions, and the resulting ionized state of Ar^+ forms plasma. The Ar^+ ions with high kinetic energy transfer their energy to the target surface molecules and eject species from target to deposit onto the substrate. When Ar^+ ions hit the target surface, secondary electrons are generated. To confine these secondary electrons and improve the deposition efficiency, cylindrical magnets with a configuration of alternating north and south poles are mounted under the target.

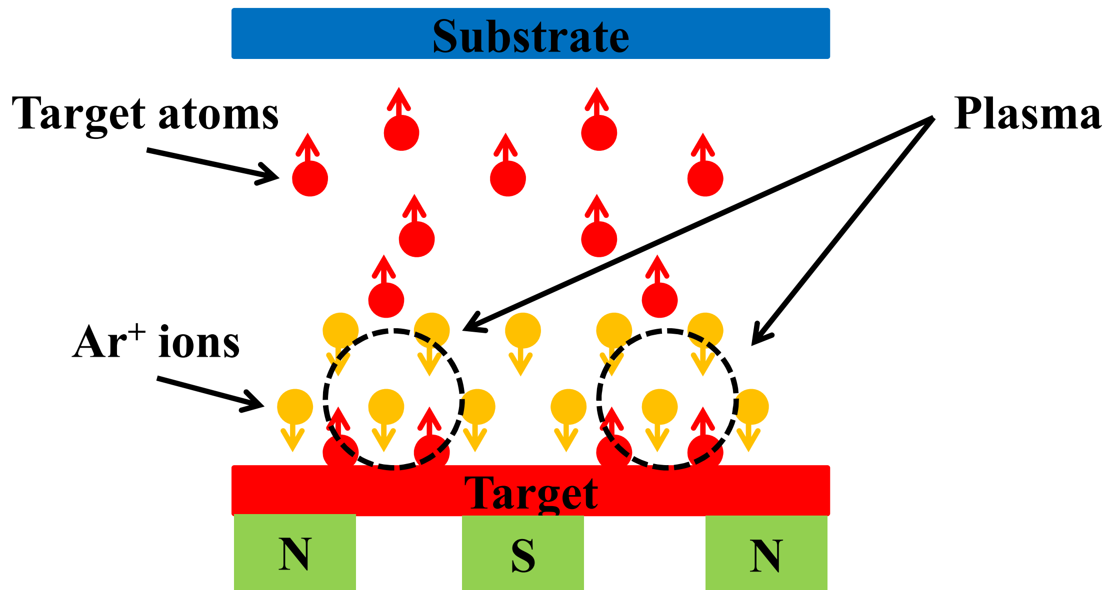

Figure 11. Working principle of magnetron sputtering.

In our device fabrication process, the top electrode (Co) and insulation layer (SiO_2), which separates the top and bottom electrodes, are deposited using a home-made magnetron sputtering system (called Shirley). Ru is also deposited on top of the Co surface to protect it from oxidizing and for wire bonding. Radio frequency (RF) voltage is applied to sputter SiO_2 on the substrate while direct circuit (DC) voltage is used for Co and Ru deposition. The deposition rate of both SiO_2 and Ru is about 2.0 nm/min and the deposition rate of Co is about 2.5 nm/min, with base pressure of about 5×10^{-7} Torr and Ar pressure during deposition of 5×10^{-3} Torr.

2.1.3 UV-photolithography

UV-photolithography is used to pattern the bottom and top electrode, and to define the tunnel junctions during our device fabrication process. Photolithography can transfer a designed pattern from a photomask to a layer of photoresist on the substrate, which can be further used to make desired thin film patterns. There are several advantages of photolithography technology.

The pattern size defined by optical lithography can be as small as a few microns, and can be scaled down to tens of nanometers using e-beam lithography. Exact control over the shape and size can also be achieved by photolithography method. In addition, it is a very cost-efficient method to create patterns over an entire surface. However, a flat substrate and extremely clean operating condition are required for this technology.

A typical photolithography process usually includes several steps in sequence: (1) Spin-coat the photoresist on top of the film and followed by a soft bake that can increase pattern resolution. (2) Align the mask on the top of the applied photoresist. (3) Expose the photoresist to UV light and develop the patterned photoresist. Sometimes a post-bake after exposure is desirable to harden the photoresist. (4) Etch the photoresist-masked films with various etching techniques, such as ion milling or reactive etching (5) Lift-off the photoresist with photoresist remover such as AZ-100 or acetone. Because acetone is very volatile, when using it as the photoresist remover, a residue of re-deposited photoresist may be left. In this case, an immediate subsequent rinse with isopropyl alcohol is recommended to remove the resist-contaminated acetone residual.

The chemical properties of photoresist can be changed when irradiated with UV light.[52] Two types of photoresist are often used in device fabrication, positive photoresist and negative photoresist. In our work, positive photoresist Shipley 1818 (Rohm and Hass Electronic Materials LLC) is used to define the bottom electrode and junction, and negative photoresist AZ 5214 (AZ Electronic Materials) is applied to pattern the top electrode. For a positive photoresist, the chemical bonds in the polymer are broken when exposed to UV light and they can easily dissolve

in a MF 319 developer (Rohm and Hass Electronic Materials LLC). Thus, the part of photoresist that covered by photomask remains. On the other hand, negative resists are polymerized when applying UV light and become less soluble in a developer. In this case, the part of photoresit covered by photomask is removed when exposed to UV light. The illustration of dry etching using (a) positive photoresist and (b) negative photoresist during a photolithography process is shown in Fig. 12.

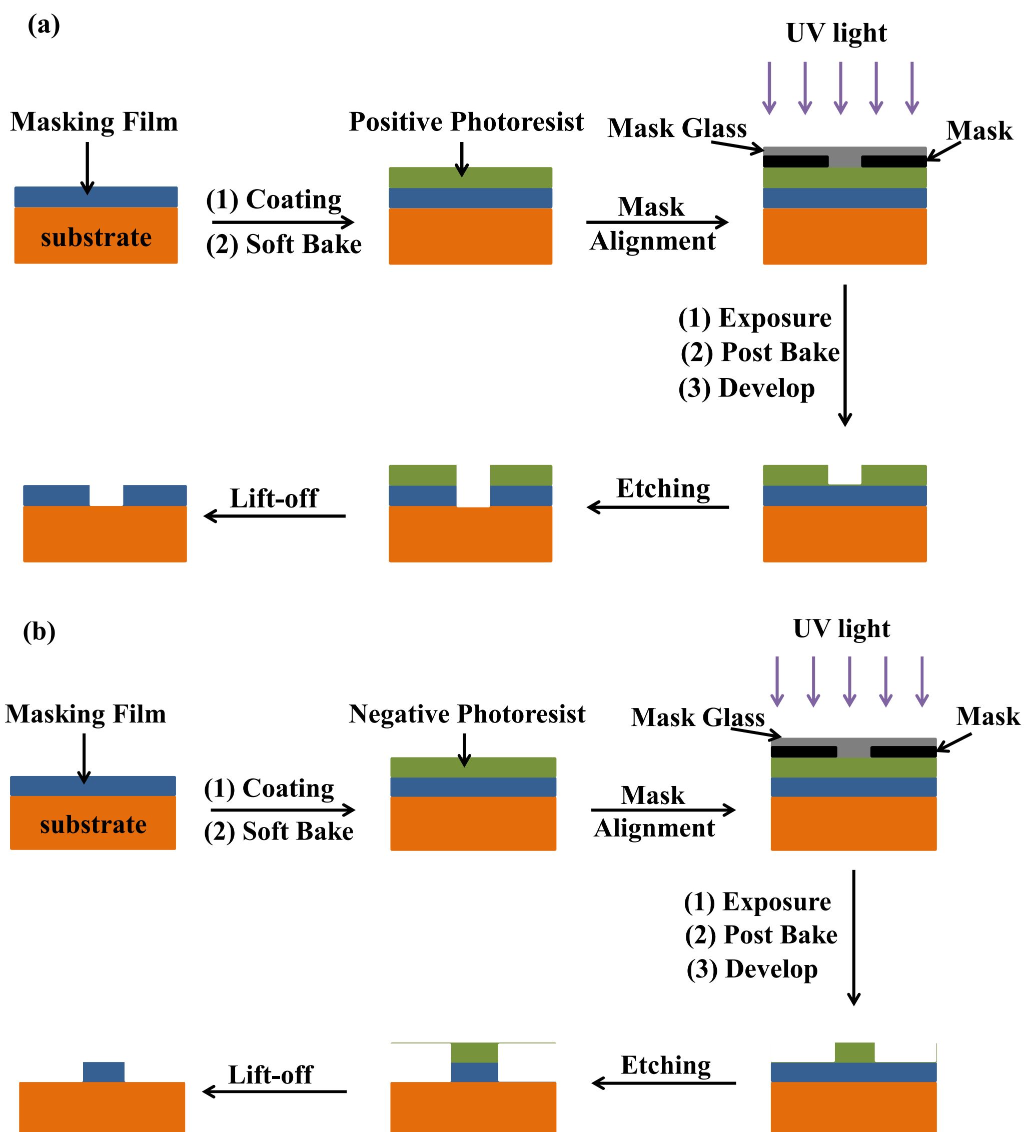

Figure 12. Dry etching using (a) Positive photoresist and (b) Negative photoresist during a photolithography process.

2.1.4 Ion milling

Ion milling is a universal dry etching method to remove materials from the sample. As compared to wet etching process, this dry etching method has very high precision and reproducibility. It can effectively etch some chemically inert materials, such as platinum, which are very hard to be removed by other etching method, and can also avoid a common problem in wet etching method that the sides of the film are easily eaten away.

The working principle of ion milling is shown in Fig. 13. The electrons produced by plasma neutralizer are attracted by a positively charged beam voltage grid. These electrons then travel in circles in a plasma chamber and collide with Ar molecules to produce ion plasma under the influence of RF magnetic field. When the produced ion plasma is sufficient, a suppressor with negative voltage is used to extract the ions from the plasma chamber. These extracted Ar ions are accelerated towards the film and recombined with electrons from the neutralizer on the way, which helps to reduce the charges built up on the patterned film. The neutralized Ar molecules bombard on the top surface of the film to remove the materials. The etching rate depends on the beam energy, density of the etched materials and the incident angle. Keeping the incident angle at 45° achieves the highest etching rate. The work plate rotates during the milling process to ensure that the ion beam bombards the sample surface uniformly. In this dissertation work, ion milling is used to etch part of the CrO_2 and VO_2 films to define the junction in our device. The multilayer structure is put into the ion miller with applied photoresist to protect its underlying materials during the etching process.

Structural damage remains a major problem during ion milling process since the high energy transferred from the ion beam can result in surface damage cracks in the films. In addition, a sub-stoichiometric surface can form since the light atoms are more easily to be removed. This can cause unwanted conductivity of the oxide substrate and thus increase the complications in the subsequent electrical measurement. One possible solution of this problem is to anneal the surface. Another problem of ion milling is the re-deposition of etched materials back onto the surface since it is a physical etch process. The re-deposition of metallic materials on the side of the insulating barrier layer can cause shorting of the barrier layer and lower the TMR and GMR values of the device. To minimize the re-deposition, the structure is switched to low angles after the initial 45° milling to remove the redeposit on the side of the barrier layer.

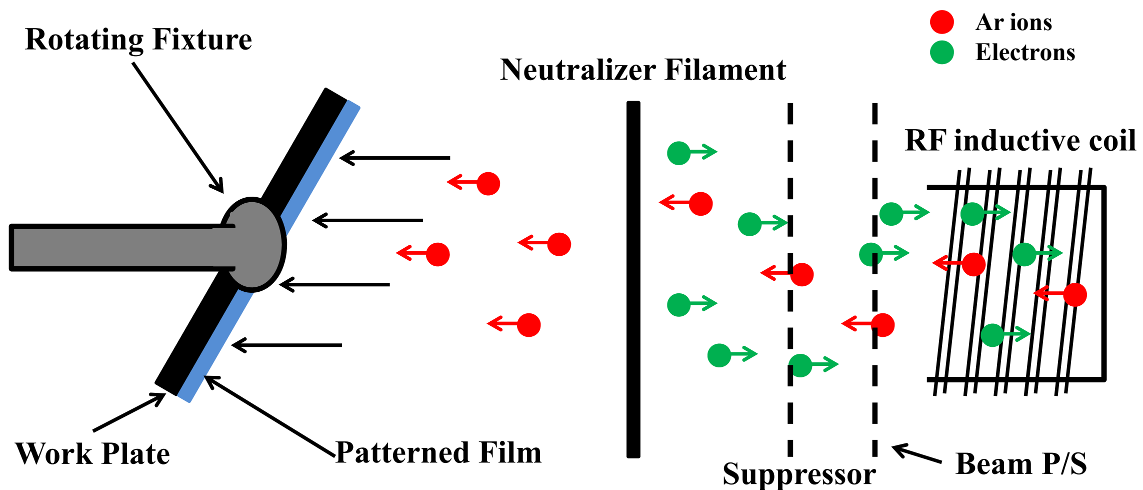

Figure 13. Working principle of ion milling.

2.2 Structural and morphology characterization

In this section, the principles of X-ray diffraction (XRD) and X-ray reflection (XRR) are introduced. XRD is a powerful tool in composition and structure characterization of the thin film

while XRR can be used to determine the thickness and interface roughness of the film. In addition, atomic force microscopy (AFM) is used to study the film morphology.

2.2.1 X-ray diffraction (XRD) and X-ray reflection (XRR)

X-ray diffraction is a non-destructive technique to obtain information about chemical composition, structure and physical properties of thin films. A typical X-ray diffractometer includes three basic elements: an X-ray source, a sample stage and an X-ray detector, as shown in Fig. 14. Electrons are produced by heating a filament (tungsten in our Philips Xpert machine) in a cathode ray tube and accelerated towards a target by applying a high voltage (about 45 kV). Characteristic X-ray spectra are then produced when electrons have sufficient energy to bombard inner shell electrons of target materials (a Cu block with K_{α}=0.1541 nm in our case). These X-rays are directed at the sample and the diffracted X-rays are recorded by a detector. The sample rotates at an angle θ with the incident X-ray beam, while the X-ray detector rotates at an angle of 2θ.

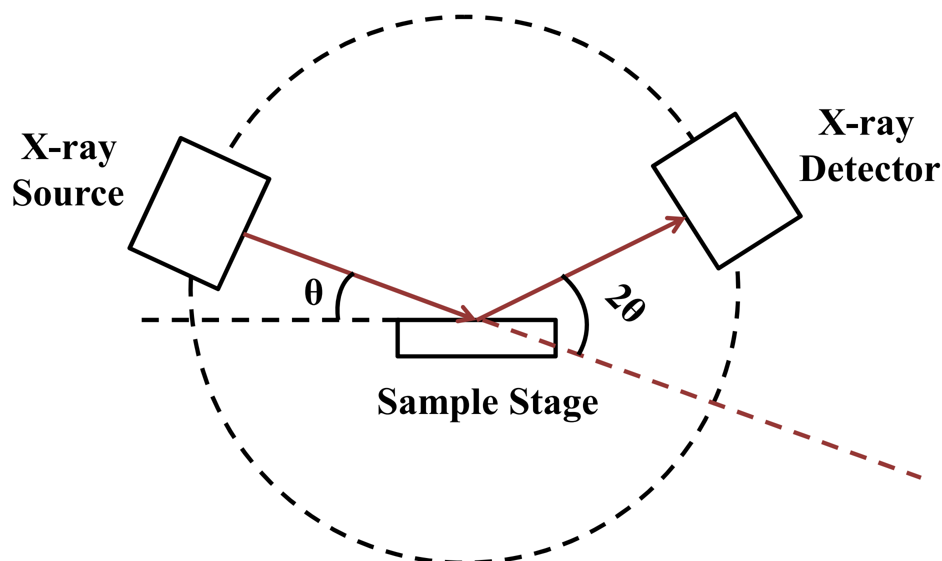

Figure 14. Schematic drawing of X-ray diffractometer.

The incident X-rays interacts with the sample. A constructive interference (a diffracted X-ray) is detected when conditions satisfy Bragg's Law [53]:

$$n\lambda = 2d \sin\theta \tag{2.1}$$

where λ is the wavelength of electromagnetic radiation (λ=0.1541 nm for CuK_{α} source), d is the lattice spacing of the sample and θ is the diffraction angle. The principles of Bragg's Law and an XRD plot of a CrO_2 film on (001) oriented TiO_2 substrate are shown in Fig. 15. X-ray diffraction technique is also used to determine substrate-induced strain and lattice parameters of CrO_2 (001) films in our work.

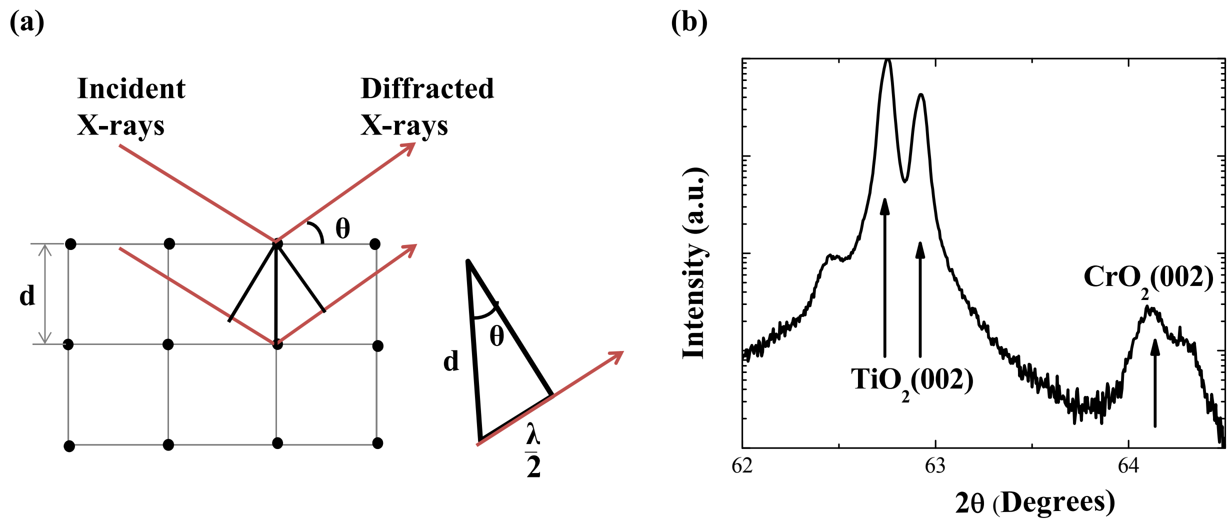

Figure 15. (a) Schematic drawing for the principles of Bragg's Law and (b) An example of XRD plot of a CrO_2 (001) film on TiO_2 substrate.

X-ray reflection technique is used to determine the film thickness, film density and interface roughness with high precision. When the incident X-rays are directed at the sample at glancing angles (incident angle θ>critical angle θ_c), X-rays can penetrate materials. The beam is reflected from both air/film and film/substrate interfaces. The reflected beams from top and bottom surface of the film interfere constructively to form periodicity of the sets of peaks in XRR plot. At low angles, the path difference Δ can be obtained by [54]:

$$\Delta = 2t\sqrt{\theta_n^2 + 2\delta} \tag{2.2}$$

where t is film thickness, θ_n is peak position in radian in nth oscillation and δ is dispersion coefficient of the materials. The principle of XRR and an XRR plot of a Co film deposited on a Si substrate are shown in Fig. 16.

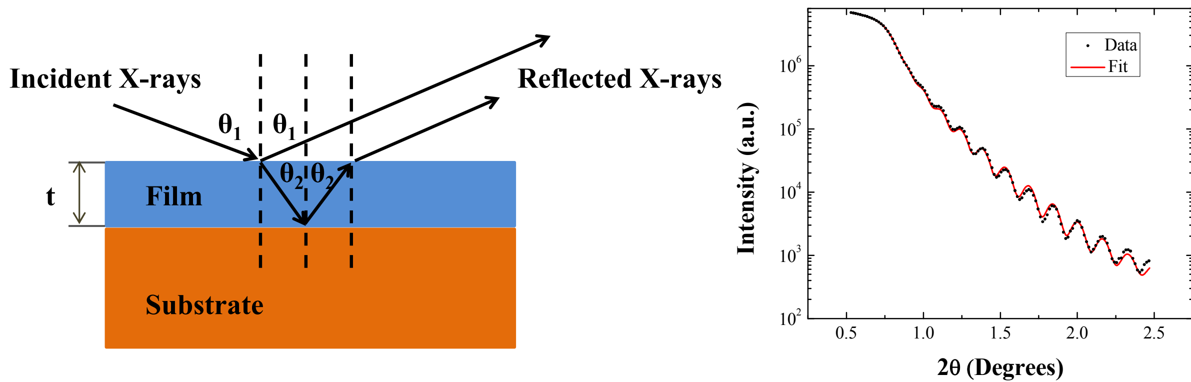

Figure 16. (a) Schematic drawing illustrating the principles of XRR and (b) An example of XRR plot of a Co film of 50 nm thickness on SiO_2 substrate.

2.2.2 Atomic force microscopy (AFM)

Atomic force microscopy (AFM) is a scanning probe technique to measure the surface morphology of the thin films with very high height resolution. In AFM system, a very sharp tip is located on a cantilever to scan the sample surface. When the distance between the tip and sample surface is large, there is no deflection of the tip. However, the tip is deflected at a certain distance due to van der Waals attractive force as the tip moves close to the surface. When the distance between the tip and surface is further decreased, the Coulomb repulsion from the surface molecules becomes dominant and forces the tip to deflect in the opposite direction. The deflection can be monitored by an optical method in which a laser is reflected from the back of the cantilever on to a photo detector. The schematic drawing of an AFM system is shown in Fig. 17. (a).

Generally, there are two imaging modes of an AFM system. One is contact mode (also called static mode) in which the tip is directly in contact with the sample surface. In this mode, the force can be kept at a pre-set value and the deflection is maintained constant by using a feed-back loop. The risk of this mode is that the tip may collide with the surface and damage the sample surface and the tip itself. To solve this problem, alternative tapping mode (also called dynamic mode) is utilized. In tapping mode, the tip does not contact the sample surface but the cantilever oscillated near its resonance frequency instead. A constant oscillation frequency can be achieved by adjusting the average tip-to-sample distance, through which a topographic image of the sample surface can be constructed. All the AFM images in this work are taken under tapping mode. An AFM image taken from the surface of VO_2 film on TiO_2 (001) substrate is shown in Fig. 17. (b).

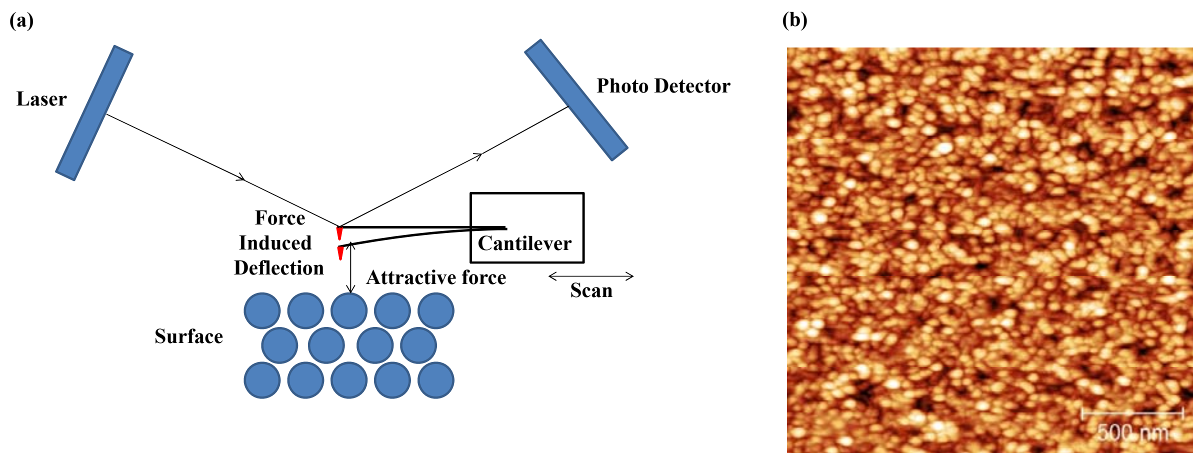

Figure 17. (a) Schematic drawing of AFM system and (b) An example of AMF image of a VO_2 film on TiO_2 (001) substrate (tapping mode is used and image size is 2 μm ×2 μm).

2.3 Magnetic measurements

Magnetic properties of the thin films in our work are measured by using vibrating sample magnetometer (VSM), alternating gradient magnetometer (AGM) and superconducting quantum

interference device (SQUID). In this section, the principles of these two measurement techniques are illustrated.

2.3.1 Vibrating sample magnetometer (VSM)

Vibrating sample magnetometer (VSM) is used to measure the magnetic properties and magnetic anisotropy of materials based on Faraday's law of induction, which indicates that electric current can be produced by magnetic flux change in a closed circuit. In a VSM system, the two poles of an electromagnet produce a uniform magnetic field that can magnetize the placed sample to induce a dipole moment. This induced dipole moment then creates an induced alternating voltage on the pick-up coils, while the sample is vibrating along the vertical z-axis (at a frequency of about 85 Hz in our DMS 1660 VSM). The pick-up voltage is proportional to the sample's magnetic moment. The electric signal in pick-up coils is then amplified and converted to the magnetic moment of the sample. Through measuring varying external magnetic field and corresponding magnetic moment of the sample, a magnetic hysteresis loop of the sample can be obtained. The schematic drawing is illustrated in Fig. 18.

The sample in the VSM system can be rotated with respect to the field and the detector. This feature enables the VSM with capability of readily measuring in-plane magnetic hysteresis loops as a function of different angle. Typically, the resolution of a VSM is about 10 μemu with scalar coils mode and can reach about 1 μemu with vector coils mode. Our VSM system adopts vector coils mode, in which four pairs of coils are fixed 90 degree apart around the sample.

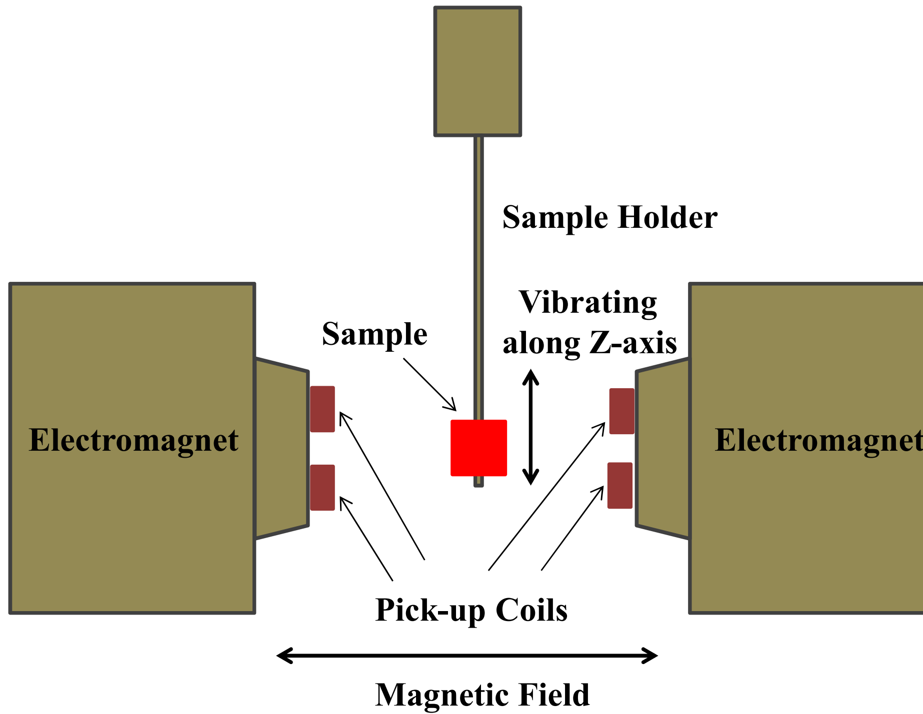

Figure 18. Schematic drawing of VSM system.

2.3.2 Alternating gradient magnetometer (AGM)

Alternating gradient magnetometer (AGM) is a sensitive instrument to measure the magnetic properties of materials. Its schematic drawing is shown in Fig. 19. In AGM system, an alternating gradient field is applied to the sample and this field can generate an alternating force with the same frequency on the sample if it has a magnetic moment. The induced force is sensed by a sensitive force balance made of piezoelectric material mounted at the other end of the sample holder, which subsequently transfers the induced force to a piezo-voltage proportional to the magnetic moment of the sample. Basically, the working principle of AGM is opposite to the VSM, in which mechanical vibrations induce an AC magnetic field.

The two primary advantages of AGM are its high speed and high sensitivity. It usually takes only a few minutes to complete a magnetic hysteresis loop. The resolution of AGM system can

reach as high as about 10^{-8} emu, which is 1000 times more sensitive than VSM system. However, the biggest drawback of AGM system is that it is difficult to measure the magnetic moment of soft materials accurately. For soft magnetic materials measurement, unwanted magnetic reversal is usually produced when applying the gradient field, which reduces the sensitivity.

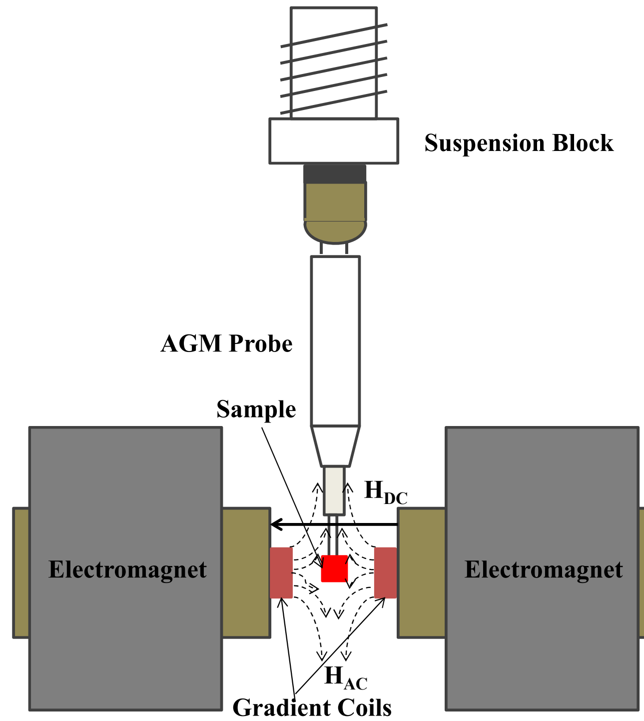

Figure 19. Schematic drawing of AGM system.

2.3.3 Superconducting quantum interference device (SQUID)

Superconducting quantum interference device (SQUID) is another commonly used magnetometer to measure the magnetic properties of materials. As compared to VSM, it has higher sensitivity and can measure the magnetic moment of the materials more accurately. Another advantage of SQUID is that it can measure the magnetic moment of materials at different temperatures readily. In our SQUID system, magnetic moment can be measured from 4 K to 350 K with applied magnetic fields as high as 5 T. However, cryogenic refrigeration with

liquid helium is needed for SQUID measurement. A SQUID magnetometer works based on the Josephson effect and its schematic drawing is shown in Figure 20. The tunneling current I produced by the two parallel superconducting junctions is related to the magnetic flux as the following expression:

$$I = I_0 \frac{\sin(\pi\phi / \phi_0)}{\pi\phi / \phi_0} \tag{2.3}$$

where ϕ is the total magnetic flux and ϕ_0 is the flux quantum ($\phi_0 = \frac{h}{2e} \approx 2.07 \times 10^{-15} Wb$). I_0 is a constant and depends only on the temperature and structure of the Josephson junctions. The high sensitivity of SQUID technique to the changes of magnetic flux results in its high sensitivity to the changes of the magnetic moment of the testing materials.

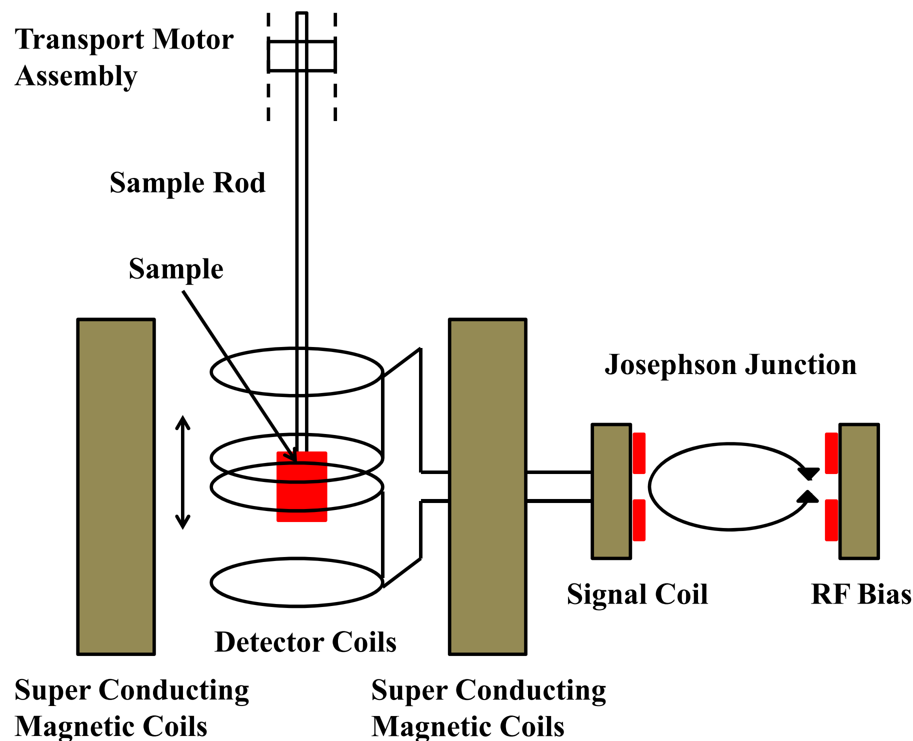

Figure 20. Schematic drawing of the SQUID magnetometer.

2.4 Transport property measurements

Electrical and magneto-transport properties of thin films and device junctions are measured using a home-made transport property measurement system. The schematic drawing of this transport system is illustrated in Fig. 21. To measure the resistance change of a thin film as a function of temperature (R-T measurement), the temperature of the sample is controlled from 4.2K to 400K by a heater attached on the back of the holder and a temperature sensor placed besides the sample. Liquid nitrogen or helium is used to achieve low temperatures. To measure the magneto-resistance of the junctions (M-R measurement), the electromagnet can produce magnetic field up to 1500 Oe.

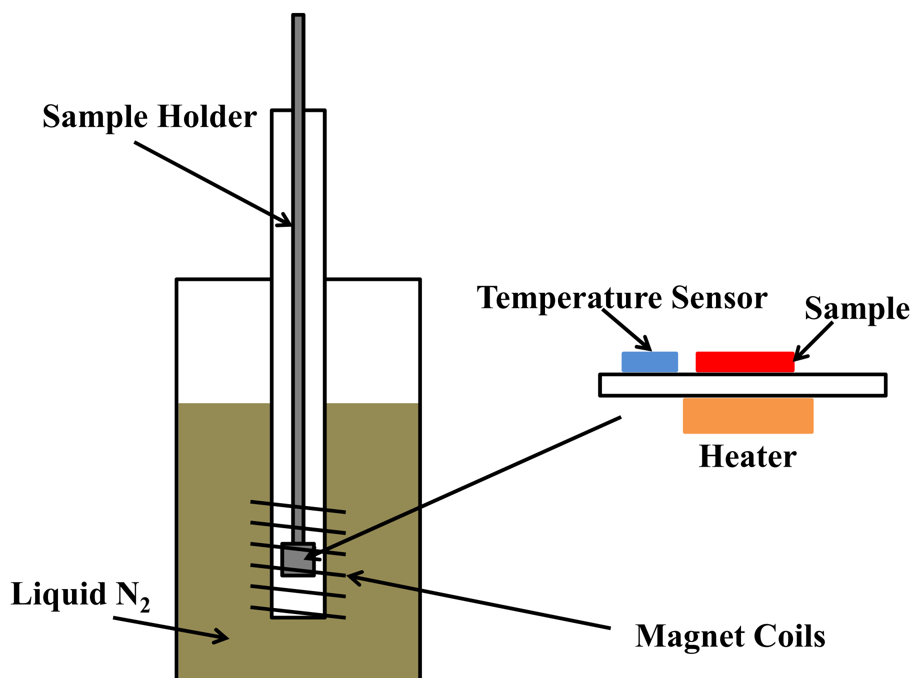

Figure 21. Schematic drawing of home-made transport measurement system.

To obtain a more accurate resistance during measurement, a four-point probe method is used to minimize the influence of constant resistances. A Voltmeter is connected to two top and bottom leads while a power source and an Ammeter are connected to two different top and

bottom electrode leads. If the limit of the voltmeter impedance is much higher than the circuit being measured, there is virtually no current passing through the voltage bridge and the measured voltage is then very close to the voltage drop across the junction itself. This four-point probe method and its electrical circuit are illustrated by Fig. 22.

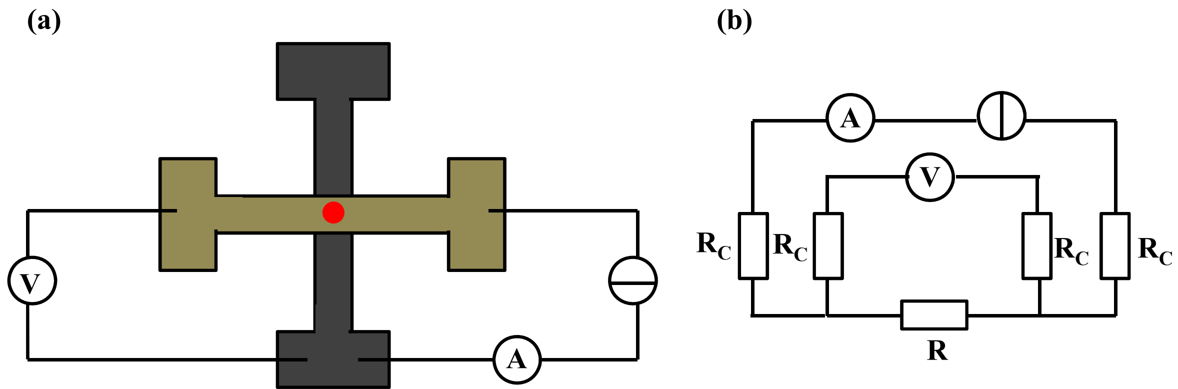

Figure 22. (a) Diagram of four-point probe methods for a measurement junction and (b) Electrical circuit diagram of four-point probe method.

CHAPTER 3

CrO_2 THIN FILMS ON (001)-ORIENTED TiO_2 SUBSTRATES

Part of this chapter is reprinted with permission from "Structural and Magnetic Properties of Epitaxial CrO_2 Thin Films Grown on TiO_2 (001) Substrates", Xueyu Zhang, Xing Zhong, P. B. Visscher, P. LeClair and A. Gupta, *Appl. Phys. Lett.*, **2013**, 102, 162410. Copyright 2013, AIP Publishing LLC.

3.1 Introduction

As mentioned in the first chapter, the efficiency of magnetoelectronic devices can be significantly improved by the adoption of half-metallic ferromagnets which exhibit a very high degree of spin polarization. Chromium dioxide (CrO_2) ,with almost 100% spin polarization near the Fermi level, is one of the well studied half-metallic materials used in spintronics.[37,39] In addition, CrO_2 possesses a relatively high Curie temperature (about 398 K), which is desirable for device applications. These two unique features, high spin polarization as long with high Curie temperature, make CrO_2 an attractive candidate material for constructing ferromagnetic layers of magnetic tunnel junctions and a model system for studying half-metals.[55-57]

Although CrO_2 is a meta-stable material, a reliable method has been developed for heteroepitaxial growth of CrO_2 thin films on rutile TiO_2 substrates by atmospheric chemical vapor deposition (APCVD).[58] In previous work, the structural and magnetic properties of epitaxial CrO_2 films grown on (100) and (110)-oriented TiO_2 substrates have been thoroughly investigated by our group and other research groups.[50,58-61] Remarkably, CrO_2 (100) films

are strained due to large lattice mismatch with the substrate and their magnetic anisotropy shows a strong variation with thickness and temperature, while CrO_2 (110) films are essentially strain-free and have little anisotropy dependence with thickness.[50,60,61] However, there are very limited studies on the structural and magnetic properties of CrO_2 (001) thin films.[62,63] In CrO_2 (001) films, the magnetocrystalline easy axis (c-axis) is perpendicular to the film surface, which is different from both CrO_2 (100) and CrO_2 (110) films. This unique feature of CrO_2 (001) films may lead to a quite different behavior of magnetic anisotropy. In addition, an unusual strain-induced surface effect, which may result in an anti-ferromagnetic transition layer between the film and the substrate, is suggested by first-principle calculation carried out on CrO_2 (001) thin films grown on TiO_2 substrates.[62]

In this chapter, the growth of high quality epitaxial CrO_2 (001) films, along with their structural characterization and a comprehensive study of the magnetic properties, are reported. The observed magnetic properties can potentially be exploited for the applications of CrO_2-based spintronic devices.

3.2 Structures of CrO_2 thin films on TiO_2 (001) substrates

The CrO_2 (001) thin films studied in this chapter are prepared in our APCVD system. The growth conditions are similar to those reported for CrO_2 (100) and CrO_2 (110) films [50,58,60,61], which were discussed in chapter 2. The X-ray diffraction scans of CrO_2 (001) films with various thicknesses are performed using a Phillips X'pert diffractometer and plotted in Fig. 23 (a). Since no peaks other than CrO_2 (002) and TiO_2 (001) are observed when the film surface was set normal to the incident plane (ranges where there are no peaks are omitted), the

deposited CrO_2 (001) films are confirmed to be epitaxial and phase-pure. The out-of-plane strain in CrO_2 (001) films gradually relaxes with increasing film thickness, similar to the behavior of CrO_2 (100) films.[50]

Off-axis diffraction scans have been carried out on the (101) planes by tilting the film appropriately to determinate the in-plane lattice parameters as shown in Fig. 23 (b). The diffraction peak positions are calibrated using TiO_2 lattice parameters provided by the substrate manufacturer. The lattice parameters of a 100 nm film are calculated to be a=b=(0.448±0.001) nm and c=(0.291±0.001) nm. Compared with bulk values (a=b=0.442 nm and c=0.292 nm) [64], the lattice of this film is found to be expanded by about 1.4% along the in-plane *a*- and *b*-axis directions due to the lattice mismatch between the film and substrate. This in-plane tension consequently induces a compression of about 0.4% along the out-of-plane *c*-axis. These in-plane and out-of-plane values represent the average of the strain across the whole film. For a thicker film of 250 nm, the average in-plane strain is reduced to 0.84% while the out-of-plane strain is decreased to 0.1%.

The epitaxy and growth texture of the film can be further confirmed by performing a ϕ-scan on the film of 100 nm thickness with the surface tilted to sample the (101) lattice planes, as shown in Fig. 23 (c). A four-fold symmetry for the film is observed, having the same texture as the substrate. The full width at half maximum of the ϕ-scan peak is about 1.1°, indicating a well-oriented film.

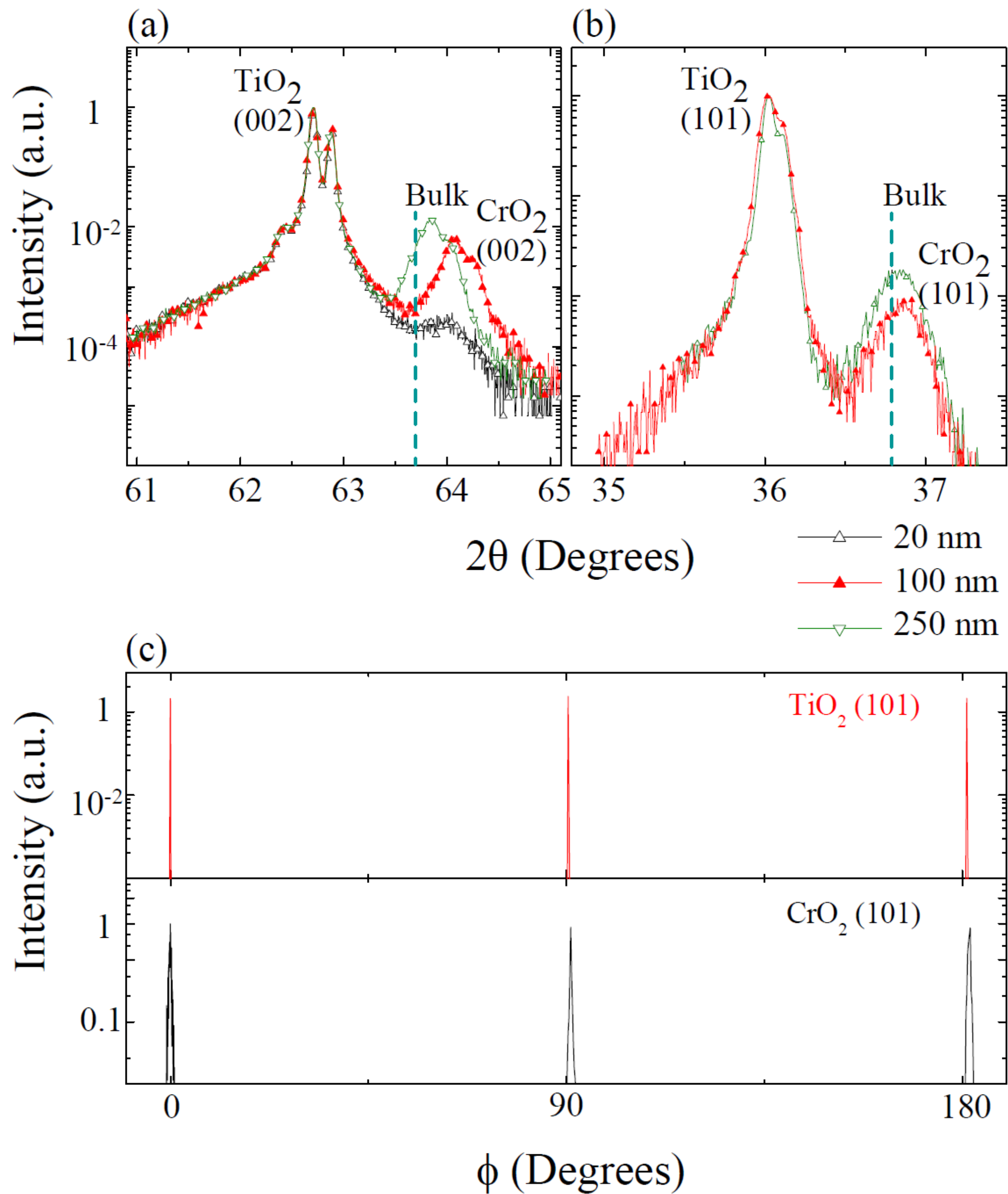

Figure 23. (a) XRD patterns using CuK-α radiation of CrO_2 (001) films with various thicknesses from 20 to 250 nm. (b) Off-axis XRD patterns for (101) peaks from the film and the substrate. Dotted lines represent the bulk 2θ peak positions for CrO_2 (002) and (101) planes. No peaks observed for 2θ angles are omitted from the plot. (c) ϕ-scan of a 100 nm film when it is tilted to sample the (101) planes.

3.3 Magnetic properties of CrO_2 thin films on TiO_2 (001) substrates

The out-of-plane and in-plane magnetic hysteresis (M-H) curves of the CrO_2 (001) thin films are performed by AGM. Fig. 24 shows the reduced magnetization-field curves with the external field applied along the out-of-plane direction for CrO_2 (001) thin films of various thicknesses. The CrO_2 (001) thin films exhibit an out-of-plane hard axis due to the relative weak perpendicular anisotropy and dominating demagnetization effect. To better understand the magnetic behavior of the films, a simple Stoner-Wohlfarth model is used to explain the out-of-plane magnetic hysteresis loops of CrO_2 (001) film, in which the film is treated as an ensemble of independent particles.

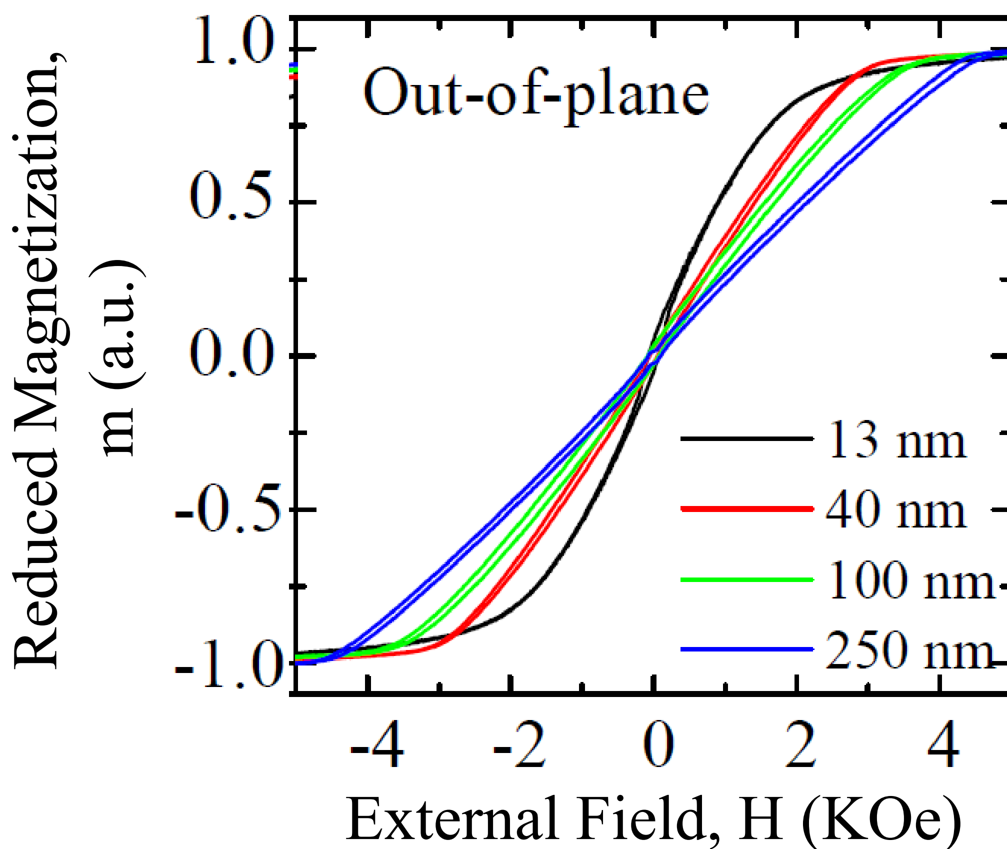

Figure 24. Reduced magnetization-field (H-M) curves when the external field is applied out-of-plane for CrO_2 (001) thin films of various thickness from 13 nm to 250 nm.

A distribution of effective anisotropy fields (H_k^{eff}) can be extracted from the second derivative of the monotonic increasing part of the out-of-plane M-H curves from 0 to saturation field based on Barandiaran's equation as [65]:

$$P(|H_k^{eff}|) = -|H_k^{eff}| \frac{d^2 m}{dH^2}\bigg|_{H=|H_k^{eff}|} \tag{3.1}$$

To reduce the noise from calculating the second derivatives, a Savitzky-Golay filter is often applied to smooth the acquired data points.[66,67] However, one drawback of this method is that artifacts in the derivative may be introduced. To address this problem, an alternate approach is used in this work. Provided that the remanence is subtracted from the M-H curve, a relation between the cumulative distribution function (CDF) of P and the first derivative of the M-H curve can be obtained by integrating both sides of Barandiaran's equation (3.1) from 0 to $|H_k^{eff}|$:

$$CDF(|H_k^{eff}|) = \int_0^{|H_k^{eff}|} PdH = m - |H_k^{eff}| \frac{dm}{dH}\bigg|_{H=|H_k^{eff}|} \tag{3.2}$$

where PdH is the probability of finding particles with $|H_k^{eff}|$ in the interval [H, $H+dH$] and m is the reduced magnetization. It is worth noting that we replace H_k^{eff} in the original Barandiaran's equation with $|H_k^{eff}|$ in our derived equation since H_k^{eff} is a negative value in our case (the uniaxial *c*-axis is the hard axis). This alternative method only requires the first derivative, making it much less noisy than the second derivative method. Therefore, the Savitzky-Golay smoothing is no longer necessary and artifacts in the derivatives are significantly reduced.

We assume that the anisotropy field of the film is normally distributed, then the *CDF* can be given by [68]:

$$CDF(H_k^{eff}) = \frac{1}{2}(1 + erf(\frac{H_k^{eff} - \langle H_k^{eff} \rangle}{\sqrt{2\sigma^2}})) \quad (3.3)$$

where $\langle H_k^{eff} \rangle$ is the mean effective anisotropy field of the film, *erf* is the error function and σ^2 is the variance. By fitting the *CDF* as shown in Fig. 25, which is experimentally extracted from Equation 3.2 to Equation 3.3, we can determine the values of $\langle H_k^{eff} \rangle$ of different thicknesses and further obtain the thickness dependence of the mean effective anisotropy constant K_{eff}.

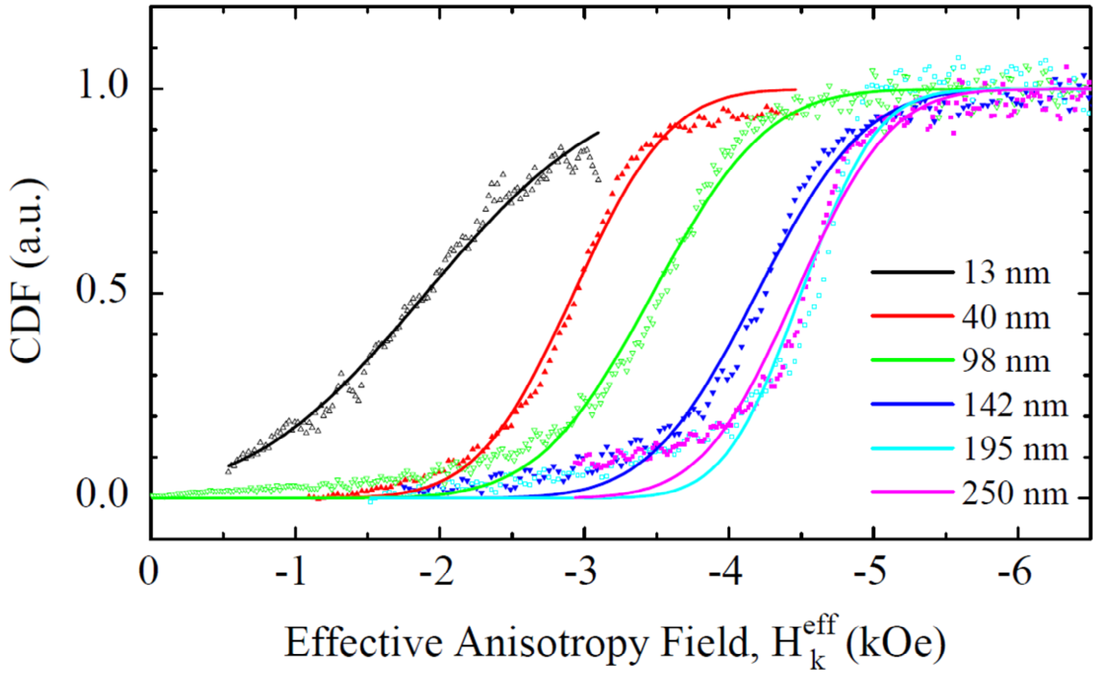

Figure 25. Extracted (dots) and fitted (lines) CDF curves of various thicknesses from 13 nm to 250 nm.

The Stoner-Wohlfarth free energy *E* of the system can be related to the mean effective anisotropy constant K_{eff} by Equation 3.4 if only the first order uniaxial anisotropy is considered as:

$$E = K_0 + K_{eff} \sin^2 \theta - M_s H \cos \theta \quad (3.4)$$

where θ is the angle between the magnetization and the uniaxial axis (*c*-axis) and M_s is the saturation magnetization. The saturation magnetization (M_s) of the CrO_2 (001) film at room temperature is determined to be (433±15) emu/cm^3 (the area of the films is 5×5 mm^2) by fitting the saturated moment as a function of film thickness as shown in Fig. 26. K_{eff} can be determined from Equation 3.5 since both M_s and $\langle H_k^{eff} \rangle$ are already known from previous calculations:

$$K_{eff} = \frac{M_s \langle H_k^{eff} \rangle}{2} \tag{3.5}$$

The mean effective anisotropy K_{eff} consists of two components, namely, shape anisotropy and non-shape anisotropy [69]:

$$K_{eff} = K + K_d \tag{3.6}$$

where K is the non-shape anisotropy and K_d is the shape anisotropy. K_d is straightforwardly determined to be (-1.2±0.1)$\times 10^6$ erg/cm^3 from $K_d = -2\pi M_s^2$.

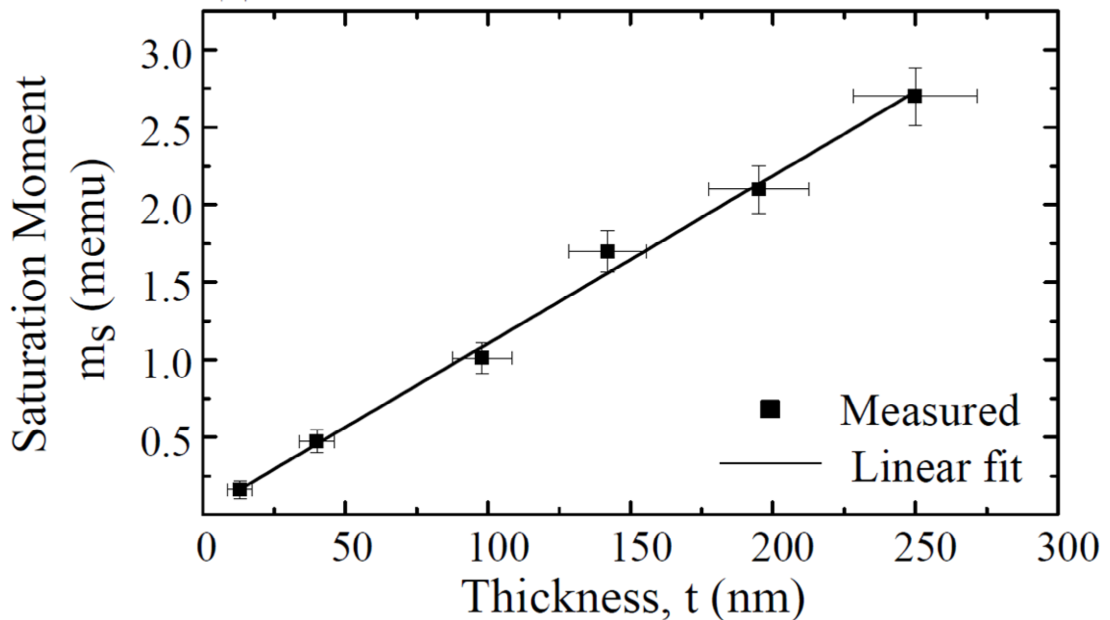

Figure 26. Saturation moment of CrO_2 (001) films as a function of thickness.

The non-shape anisotropy K of the film is assumed to consist of two terms originating from magnetocrystalline (K_c) and strain (K_σ) anisotropy: $K=K_c+K_\sigma$. For a simple model, we assume that there is a thin layer near the film-substrate interface in which most of the film strain is localized. Above this layer, the film is uniform and strain-free. The thickness of this strained layer is estimated to be about 40 nm in CrO_2 (100) films.[50] Compared to CrO_2 (100) films, we expect a thinner strained layer in our CrO_2 (001) films since a larger lattice mismatch between TiO_2 substrate and CrO_2 film along c-axis than along a- and b-axis (3.91% vs 1.44%) [58] can results in relatively weaker strains in CrO_2 (001) films. It is this layer that produces a strain anisotropy, which probably imitates the surface anisotropy due to symmetry breaking.[70] The resulting strain anisotropy is inversely proportional to the film thickness t [71,72]: $K_\sigma=K_s/\mathrm{t}$, where K_s is a surface anisotropy constant. Therefore, the total non-shape anisotropy K can be expressed as:

$$K = K_c + \frac{K_s}{t} \tag{3.6}$$

K of various thicknesses can be extracted from the out-of-plane M-H curves, which is plotted in Fig. 25. Furthermore, we can take Equation 3.6 to fit the data in Fig. 27, from which the first order magnetocrystalline anisotropy K_c can be determined to be $(2.2\pm0.5)\times10^5$ erg/cm^3 , which agrees with literature values quite well.[59,73,74] The surface anisotropy K_s can also be obtained from this fitting and found to be (0.9±0.2) erg/cm^2. If we let $K_s/t=K_c$, a characteristic thickness of about 40 nm can be determined, below which the surface anisotropy exceeds the magnetocrystalline anisotropy. This characteristic thickness agrees well with our assumption that strain is mostly interfacial. It is also comparable with a reported result for CrO_2 (100) film, whose critical thickness for strain-induced easy axis switching is about 55 nm.[50] The characteristic thickness explains the magnetic behavior in our M-H hysteresis loops that a large

shape anisotropy pins the easy axis in the film plane but a trend of being more easily magnetized perpendicularly for thinner films.

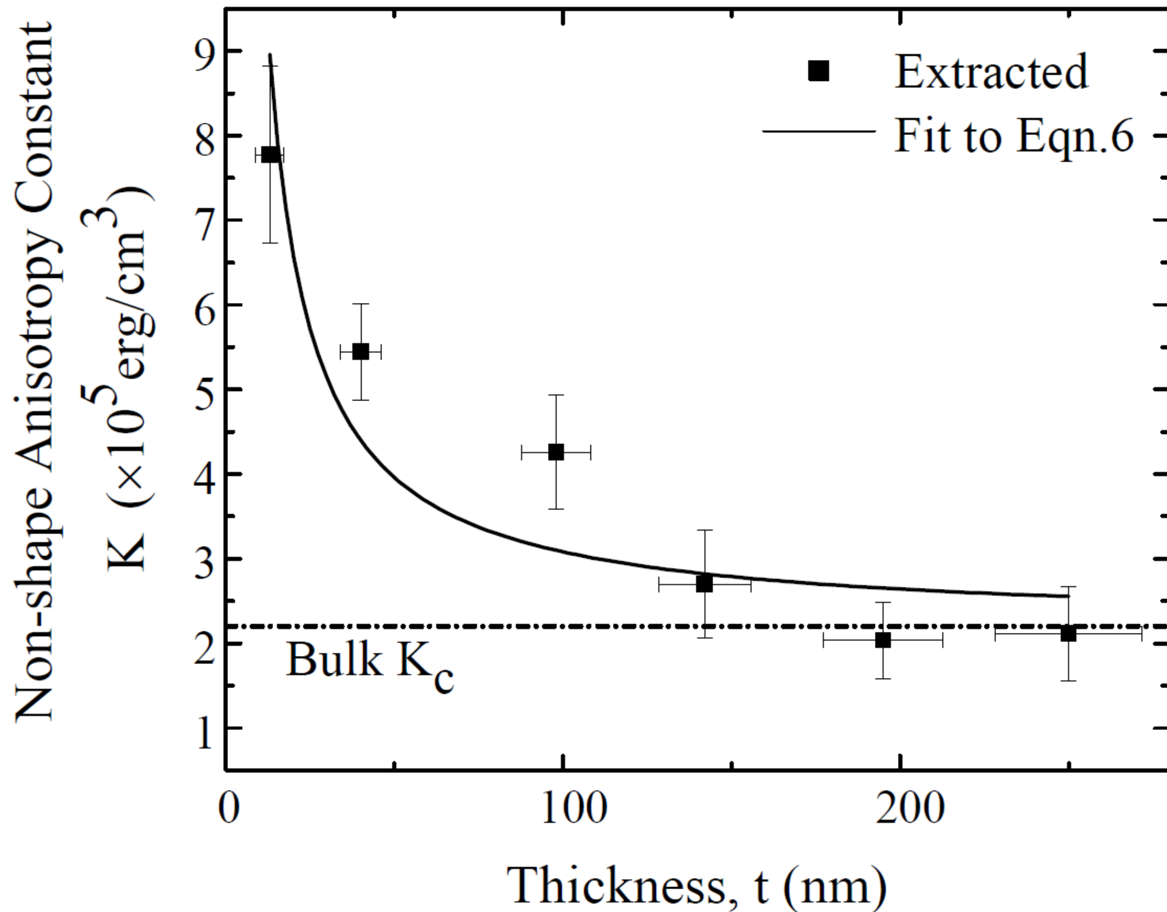

Figure 27. Extracted (dots) and fitted (lines) non-shape anisotropy constants for CrO_2 (001) films of various thickness from 13 to 250 nm.

The extracted distribution of H_k^{eff} may originate from either a varying local demagnetizing field caused by film roughness, and/or perhaps a distributed strain across the film. This makes our Stoner-Wohlfarth model inadequate to explain the hysteresis observed in measured out-of-plane M-H curves since possible domain nucleation and formation in the film are neglected. One explanation of the observed hysteresis could be that the domain boundaries in CrO_2 (001) films can readily move with an out-of-plane field but need re-nucleation after being saturated.[75] On

the other hand, the tails in the extracted CDF curves derived from the presumed normal distributions in the low $\left|H_k^{eff}\right|$ regions indicates a locally decreased demagnetizing field in the thicker films, which can be possibly caused by domain structures or other asymmetrical modulations to local demagnetization factors and non-Gaussianity in the strain distribution.

As we assume a Stoner-Wohlfarth model that considers each particle is independent, an easy plane parallel to the film surface would be expected, in which the in-plane magnetic moment should be able to switch with a small external field. However, this expectation is in contrast with the magnetic behavior of in-plane M-H curves of CrO_2 (001) films shown in Fig. 28. The saturation fields of in-plane hysteresis loops are above 1 kOe for all investigated film thicknesses. Stripe domain patterns, which are often observed in thin film materials with relatively weak perpendicular anisotropy ($\left|(K_c + K_\sigma)/K_d\right| < 1$) , could be one possible explanation for this unusual behavior. Within these stripe domains, the in-plane magnetization oscillates out-of-plane periodically in a flux-closed manner.[70] The saturation field of in-plane M-H curves are significantly larger for thinner film (t<40 nm), which is caused by a larger K_σ to maintain the magnetization perpendicular. It is worth nothing that the magnetic behaviors at various measurement angles within the surface plane are identical since the lattice mismatch between the film and substrate along *a*- and *b*-axis are the same, which is another difference from CrO_2 (100) and (110) thin films.

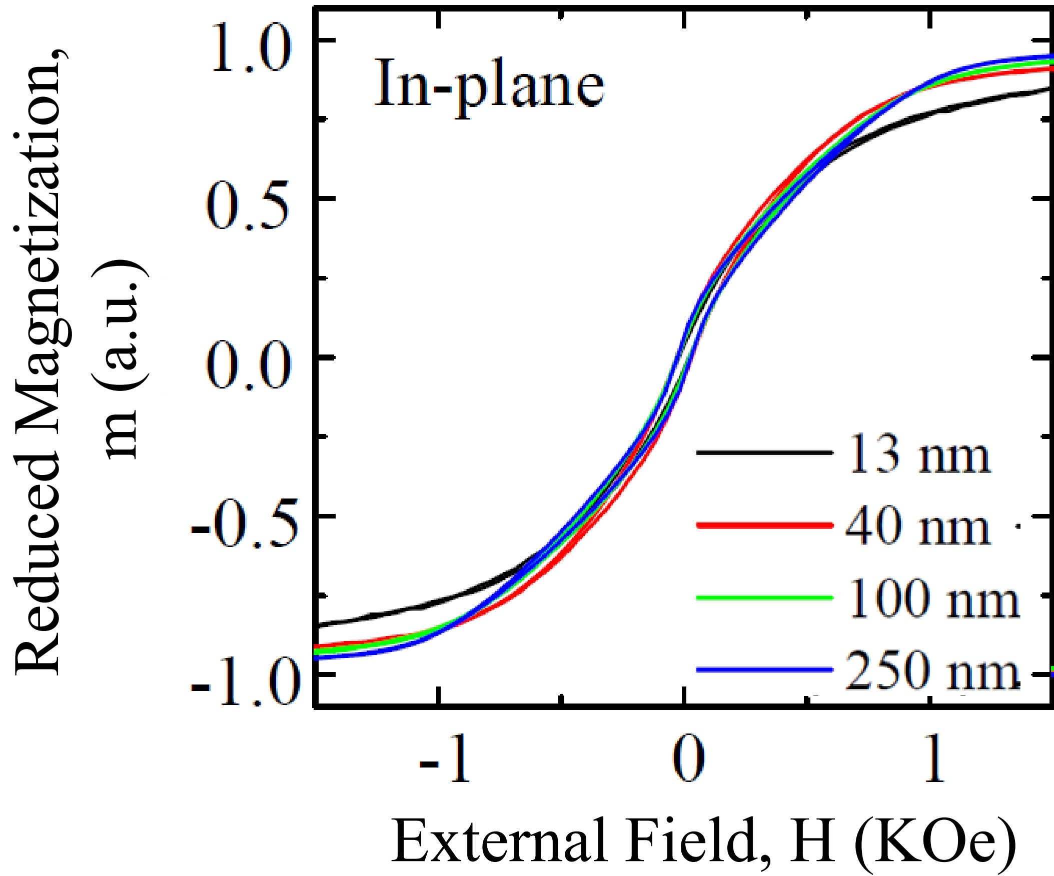

Figure 28. Reduced magnetization-field (M-H) curves when the external field is applied in-plane of CrO_2 (001) thin films with various thickness from 13 nm to 250 nm.

3.4 Conclusion

In summary, epitaxial CrO_2 thin films have been deposited on TiO_2 (001) substrates with our APCVD system. The rutile structure of the CrO_2 (001) films is slightly expanded along the in-plane *a*- and *b*-axis due to lattice mismatch with the substrate while it is compressed along the out-of-plane *c*-axis as a result of elastic deformation. With increasing film thickness, the averaged strain in the films gradually relaxes. The magnetization of the CrO_2 (001) films is determined to be (433±15) emu/cm^3 at room temperature, which is about 10% smaller than the bulk value (483 emu/cm^3).

Because of the competition among shape anisotropy, magnetocrystalline anisotropy and surface anisotropy, CrO_2 (001) thin films show quite distinct magnetic behavior from CrO_2 (100) and CrO_2 (110) thin films. The magnetic hard axis of the CrO_2 (001) thin films is found to be out-of-plane. A Stoner-Wohlfarth model with a normal distribution of H_k^{eff} is assumed to explain the out-of-plane magnetic behavior of the CrO_2 (001) thin films. With this model, the shape anisotropy constant K_d is determined to be $(-1.2\pm0.1)\times10^6$ erg/cm^3, while the magnetocrystalline anisotropy constant K_c and the surface anisotropy constant K_s are fitted to be $(2.2\pm0.5)\times10^5$ erg/cm^3 and (0.9 ± 0.2) erg/cm^2, respectively. However, this model is insufficient to explain small hysteresis observed in out-of-plane M-H curves partly due to lack of considering possible domain nucleation and the interactions between the particles in the films. The CrO_2 (001) thin films are found to be in-plane isotropic with identical magnetic behaviors at various measurement angles within the surface plane. The observed in-plane M-H hysteresis curves may result from stripe of vortex domain structures with an almost closed flux in the remanent state.

CHAPTER 4

VO_2 THIN FILMS AND CrO_2/VO_2 HETEROSTRUCTURES ON (100), (110) AND (001)-ORIENTED TiO_2 SUBSTRATES

4.1 Introduction

Vanadium oxide is a versatile material that can exist in thirteen different polymorphs, ranging from V_5O_9 to V_2O_5.[76] Among these polymorphs, vanadium dioxide (VO_2) has been extensively investigated for a long time and is still an active research area, primarily due to its metal-insulator transition (MIT) that occurs just above room temperature. VO_2 behaves as a good conductor in the rutile structure at high temperatures while it acts as an insulator in its monoclinic phase at low temperatures.[77] This abrupt change in its dielectric property makes VO_2 an intriguing candidate for use as a barrier layer in spintronic devices that may exhibit novel phenomena, such as a switch between TMR and GMR effect at different temperatures.

For practical purposes, the transition temperature of the device should be close to room temperature. The transition temperature of VO_2 is proportionately related with the length of the *c*-axis.[78] In this section, we will discuss the properties of VO_2 thin films deposited on top of (100), (110) and (001)-oriented TiO_2 substrates in our APCVD system. Their structural and MIT characteristics are investigated to determine the most desirable substrate to grow VO_2 thin films with transition temperature close to room temperature.

As discussed in chapter 3, CrO_2 is a good candidate for use as the ferromagnetic layer in GMR or TMR devices. Since both CrO_2 and VO_2 have the same rutile (or related monoclinic) crystal structure, the lattice mismatch between them is relatively small. As a result of the good compatibility between CrO_2 and VO_2, it is possible to grow CrO_2/VO_2 heterostructures, which is of critical importance for constructing our CrO_2/VO_2/Co device. In our work, the CrO_2/VO_2 heterostructures are grown on (100), (110) and (001)-oriented TiO_2 substrates, and their magnetic and electrical properties are investigated.

4.2 VO_2 thin films on (100), (110) and (001)-oriented TiO_2 substrates

VO_2 thin films are deposited on TiO_2 (100), (110) and (001) substrates by our APCVD system as described in chapter 2. X-ray diffraction is used to characterize the lattice parameter and the phase purities of these differently oriented films.

A peak is observed around 39.9° in the XRD pattern of VO_2 films grown on TiO_2 (100) substrates that can be identified as the (200) planes of VO_2 as shown in Fig. 29 (a). To determine the epitaxy of the deposited VO_2 thin films, rocking curve measurements are carried out by scanning with fixed 2θ at the corresponding peak position. The full width at half maximum (FWHM) is determined to be 0.030° from the rocking curve, which indicates a high crystalline quality of the VO_2 (100) thin films. The Bragg peak of VO_2 (110) film is around 27.9° as shown in Fig. 29 (b), and the FWHM of its rocking curve is determined to be 0.034°. For VO_2 thin films grown on TiO_2 (001) substrates, the XRD plot shows that the VO_2 (002) peak is around 65.3° and the FWHM is about 0.040° as shown in Fig. 29 (c). From the XRD patterns, it is confirmed

that the epitaxial VO_2 can be successfully grown on these three differently oriented TiO_2 substrates by our APCVD system.

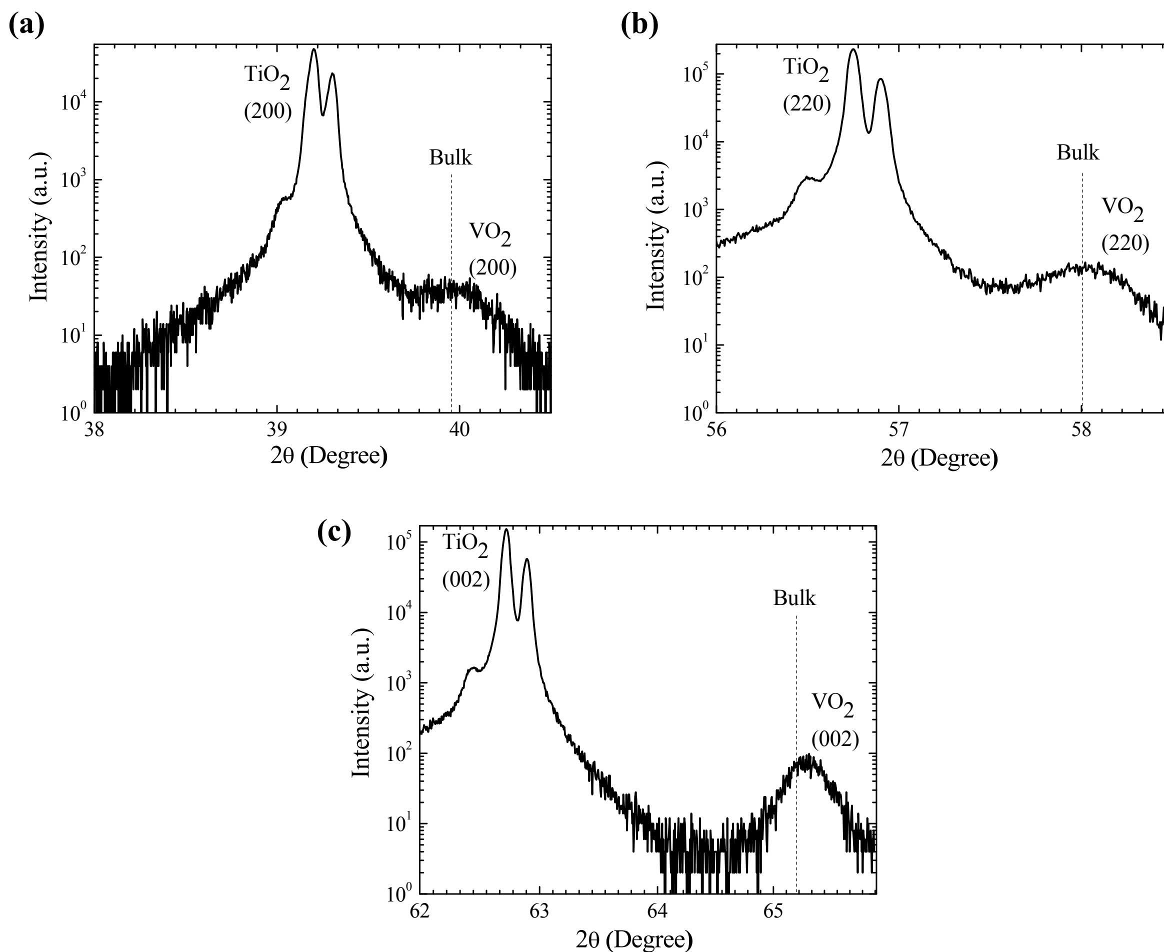

Figure 29. XRD patterns of VO_2 film on (a) (100), (b) (110) and (c) (001) TiO_2 substrates.

The surface morphology of the VO_2 films is measured by atomic force microscopy (AFM), as shown in Fig. 30. The roughness of VO_2 films deposited on (100), (110) and (001)-oriented TiO_2 substrates with similar thickness (about 30 nm) are 2.8 nm, 1.2 nm and 2.5 nm, respectively. The results indicate that the surface of VO_2 (110) films is much smoother than (100) and (001)-oriented films, and suggest that VO_2 (110) may be a more desirable barrier layer for use in spintronic devices. Basically, the surface roughness of the films with the three orientations

increases with increasing film thickness, as shown in Fig. 31. The roughness of VO_2 (100) and (001) films show a linear relationship with film thickness, while the roughness of VO_2 (110) thin films shows a sharp increase when film thickness is above 30 nm.

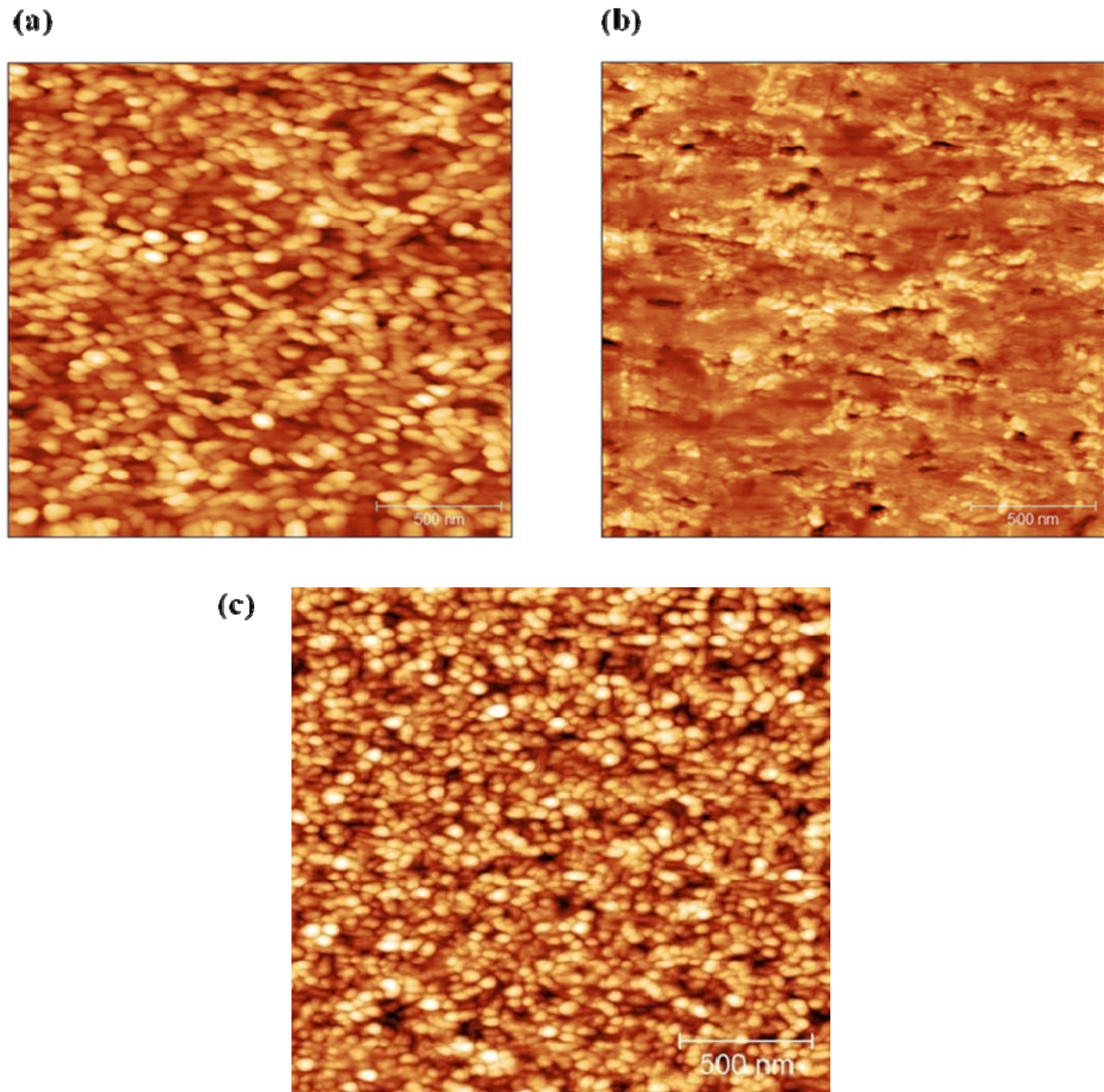

Figure 30. AMF image of VO_2 films on (a) (100), (b) (110) and (c) (001) TiO_2 substrate. The three different oriented films have the same thickness of about 30 nm.

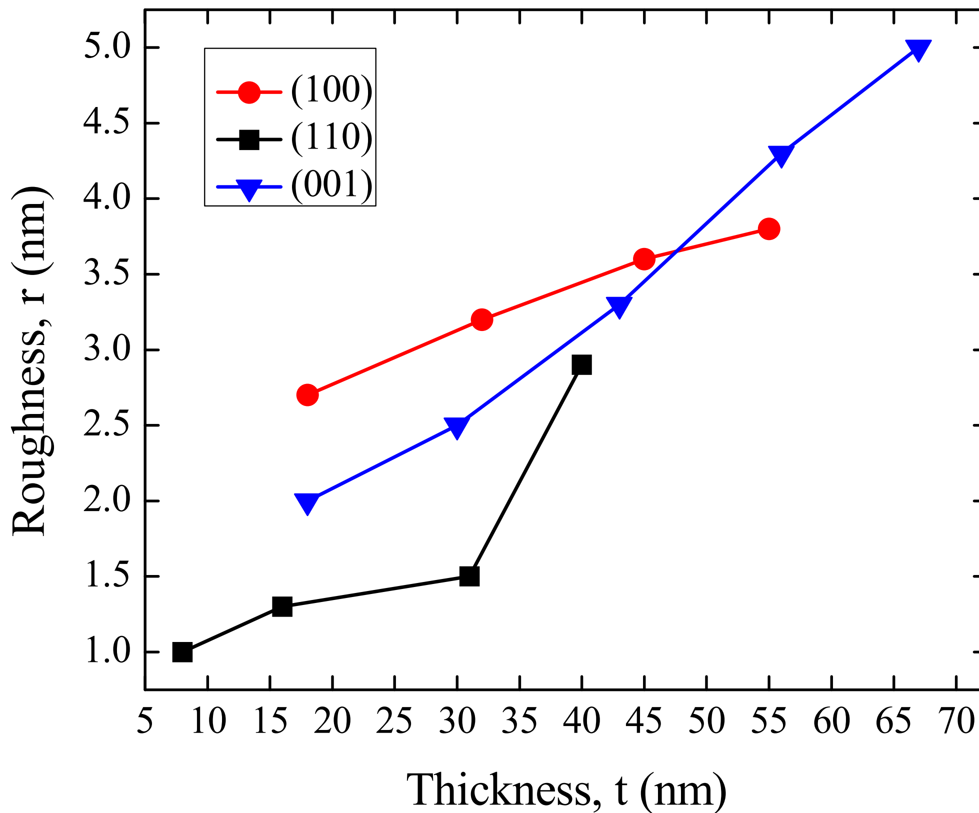

Figure 31. Roughness as a function of film thickness for VO_2 thin films on TiO_2 substrates with various orientations.

To study the MIT features of VO_2 thin films, resistance-temperature measurements for the VO_2 films of different orientations are performed, as shown in Fig. 32. Both the heating up and cooling down curves are recorded to study the hysteresis of transition. Sharp resistance changes of the (100), (110) and (001)-oriented VO_2 thin film that result from the MIT around a critical temperature can be observed. It is found that the VO_2 (001) thin films have the lowest transition temperature of about 312°C, which is very close to the room temperature, among the three differently oriented VO_2 films. This may be explained by the fact that the *c*-axis in VO_2 (001) films is contracted, while it expands in VO_2 (100) and (110) films. As a result, the distance between the V^{4+} and V^{4+} ions along the *c*-axis of CrO_2 (001) films is reduced, which forms direct overlap of the *d* orbitals. The resulting increased width of the *d* band stabilizes the metallic phase

of the rutile structure. Therefore, with the reduced *c*-axis, the transition temperature of the VO_2 (001) thin films decreases.[78]

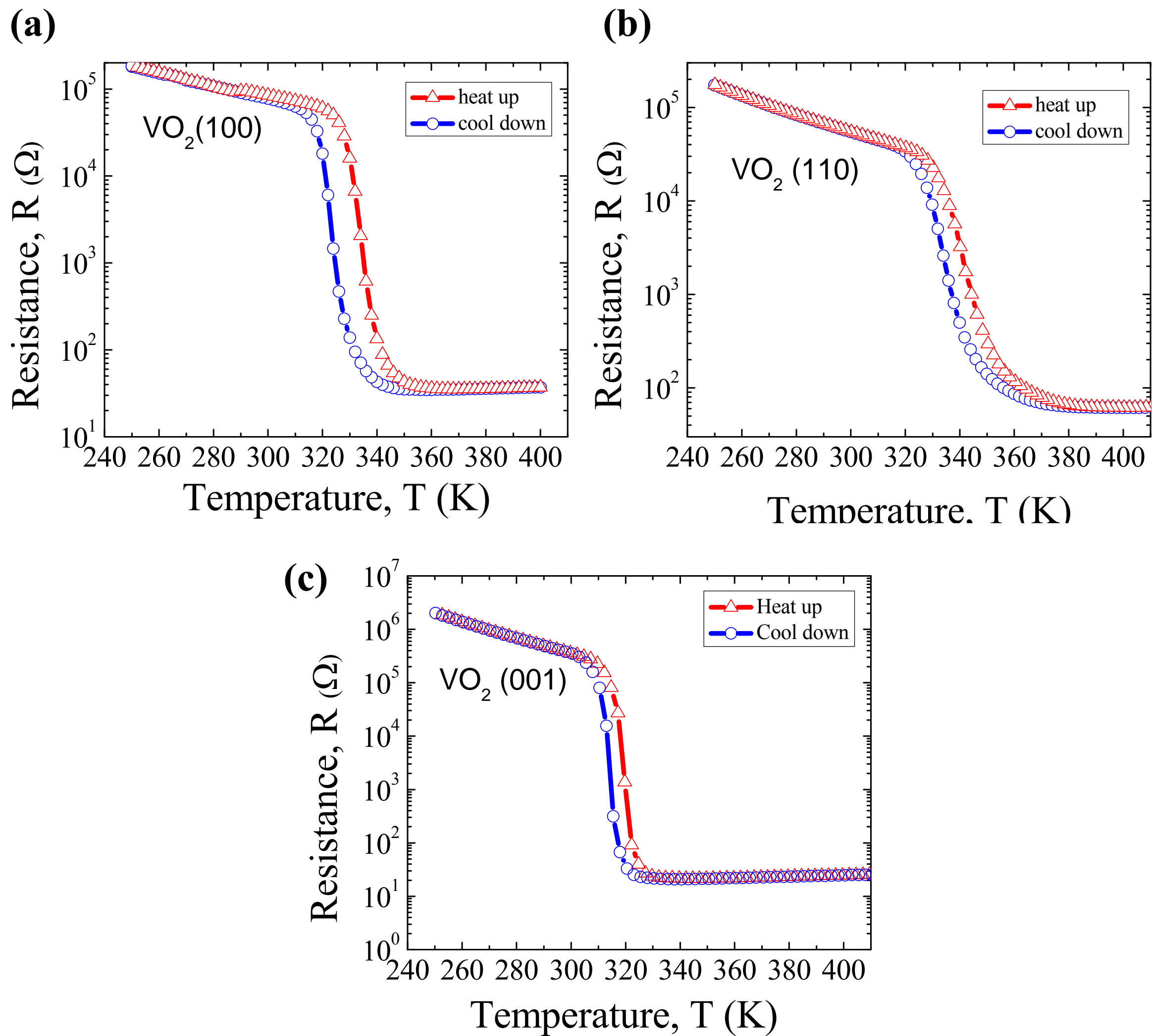

Figure 32. Resistance as a function of temperature of VO_2 thin films on (a) (100), (b) (110) and (c) (001) TiO_2 substrates. The thickness of all films is about 30 nm.

A comparison of the electrical transition properties of the differently oriented VO_2 thin films of about 30 nm thickness is listed in Table 1. At the transition temperature, the resistance changes (ratio) can be as much as a factor of 5500 for (100)-oriented films, 2000 for (110)-oriented films, and more than 17000 for (001)-oriented films. The VO_2 (001) film has the most

significant resistance change near the transition temperature and the narrowest hysteresis width of about 5 K.

Table 1. Comparison of the metal-insulator-transition properties of differently oriented VO_2 thin films of 30 nm thickness.

VO_2 Thin Film	Transition Temperature, T (K)		Hysteresis Width, T (K)	Resistance Change Ratio, ΔR
	Heating	Cooling		
(100)	328	318	10	5500
(110)	331	325	7	2000
(001)	312	301	5	17000

4.3 CrO_2/VO_2 heterostructures on (100), (110) and (001)-oriented TiO_2 substrates

VO_2, CrO_2 and TiO_2 are materials with rutile structure and their lattice parameters are close to each other, which makes it possible to grow CrO_2/VO_2 heterostructures on top of TiO_2 substrates. Table 2 lists the lattice parameters of these three rutile oxides.[60,78] The growth of CrO_2/VO_2 heterostructures is one of the fundamental steps for fabricating our target spintronic device. Both the deposition of CrO_2 on (100), (110) and (001)-oriented TiO_2 substrates and the growth of VO_2 on top of the CrO_2 film surface are carried out in our APCVD system.

As mentioned in chapter 2, the deposition temperature of VO_2 thin films is between 380°C to 450°C. When we grow VO_2 film on top of CrO_2 film, this temperature may be sufficiently high to decompose the deposited CrO_2 thin film. If the CrO_2 thin film decomposes, the

magnetoresistance of our target device will decrease sharply since the CrO_2 material is used as the spin-polarized ferromagnetic layer.

Table 2. Lattice parameters of Rutile VO_2, CrO_2 and TiO_2 materials. Taken from ref. [60,78]

Materials	a (nm)	c (nm)	d_{110} (nm)
VO_2	0.4554	0.2858	0.3220
CrO_2	0.4421	0.2916	0.3126
TiO_2	0.4593	0.2959	0.3248

To test the extent of decomposition of CrO_2 thin films, VSM measurements are performed to obtain the magnetization of CrO_2/VO_2 bilayer structures on (100), (110) and (001)-oriented TiO_2 substrates, as shown in Fig. 33. The thickness of the CrO_2 layer for all types of bilayer structures is about 50 nm. Based on the saturation magnetic moment obtained from the M-H curves, the magnetization of each bilayer structure can be derived according to:

$$M = \frac{m}{s \times t} \tag{4.1}$$

where M is the magnetization of the structure, m is the saturation magnetic moment, s is the film surface area (5×5 mm^2 for our sample) and t is the thickness of the CrO_2 layer of the hetero-structure. The magnetization of (100) and (001) bilayer structures are determined to be 320 emu/cc and 200 emu/cc respectively, both of which are reduced significantly from the bulk value of pure CrO_2 film (about 450 emu/cc). In contrast, the magnetization of the CrO_2 layer (about 440 emu/cc) in CrO_2/VO_2(110) bilayer structures is nearly the same as that of pure CrO_2 film,

suggesting that little decomposition of CrO_2 layers occurs in the process of growth of bilayer structure.

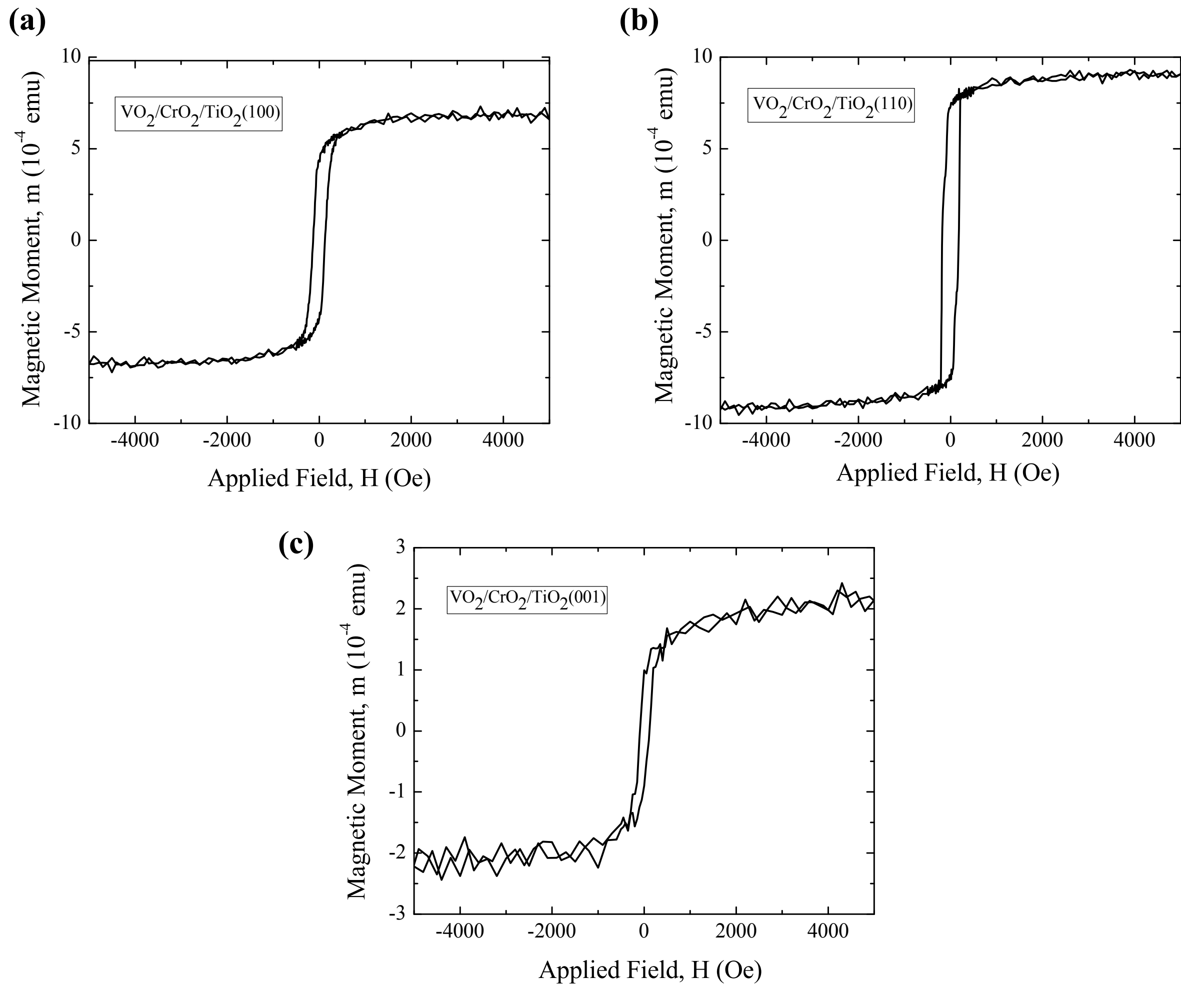

Figure 33. Magnetic hysteresis loops of CrO_2/VO_2 bilayer structures on (a) (100), (b) (110) and (c) (001) TiO_2 substrates. The thickness of CrO_2 layer for all bilayer structures is about 50 nm.

In addition, the surface roughness of CrO_2/VO_2 (110) bilayer structures is about 1.5 nm and is much smoother than the surface of (100) and (001)-oriented bilayer structures with similar thicknesses of CrO_2 and VO_2. The comparison of the properties of the three types of bilayer structures is summarized in Table 3. By comparing these properties, we consider that TiO_2 with

(110) orientation would be a better substrate choice for the fabrication of the designed spintronic devices.

Table 3. Comparison of film roughness and magnetization of CrO_2/VO_2 structures on (100), (110) and (001)-oriented TiO_2 substrates..

CrO_2/VO_2	Thickness of CrO_2 layer, t (nm)	Thickness of VO_2 layer, t (nm)	Roughness, r (nm)	Magnetization, M (emu/cc)
(100)	50	30	10.2	320
(110)	50	30	1.5	440
(001)	50	30	5.5	200

4.4 Conclusion

We have successfully deposited VO_2 single layers as well as CrO_2/VO_2 bilayers on (100), (110) and (001)-oriented TiO_2 substrates with our CVD systems. For single layers, VO_2 (001) films exhibit the lowest transition temperature (about 312 K) and the largest resistance change - as much as 17000 times around the transition temperature - both of which are desirable properties for device applications. These characteristics can be partially explained by the reduced length of the *c*-axis in VO_2 (001) films, which can increase the overlap of *d* orbitals of V^{4+} ions along the *c*-axis. The increased width of *d* bands makes it easier for the film to convert to the metallic phase from the monoclinic phase, and as a result decreases the transition temperature. However, the VO_2 (110) films have much smoother surface, which are more desirable for device fabrication.

In addition, CrO_2/VO_2 bilayer structures on (100), (110) and (001)-oriented TiO_2 substrates are investigated in this chapter. The CrO_2/VO_2 (110) heterostructures show nearly the same magnetization as the ones for pure CrO_2 film, suggesting that there is no or very little decomposition of CrO_2 layers when constructing the bilayer structures. Furthermore, the CrO_2/VO_2 (110) structures have a much smoother surface compared with CrO_2/VO_2 (100) and (001) structures. In summary, the TiO_2 (110) substrates are considered as a better substrate choice for fabricating the designed CrO_2/VO_2-based devices.

CHAPTER 5

SPIN TRANSPORT IN CrO_2-BASED MAGNETIC TUNNEL JUNCTIONS

5.1 Introduction

In recent years, magnetic tunnel junctions (MTJs) have been studied intensively for various applications, including hard disk drives, magnetic sensors and memory devices.[26,28,29] MTJs usually consist of two ferromagnetic electrodes separated by a thin insulating barrier layer. The relative magnetization orientation of the two ferromagnetic electrodes can be switched between parallel and anti-parallel alignments, resulting in a significant resistance change of the junction. This phenomenon is commonly referred as tunneling magnetoresistance (TMR) because electrons pass through the insulating barrier by means of quantum tunneling. To enhance TMR effects of the junctions, materials with high spin polarization are preferred for the ferromagnetic electrodes. As mentioned in Chapter 3, CrO_2, a known half-metal, shows a spin polarization of nearly 100%.[39] Therefore, CrO_2-based MTJs are fabricated with the intention of realizing high TMR effect in the devices. One of the commonly used barrier layers in CrO_2-based MTJs is Cr_2O_3.[79,80] Since CrO_2 is a metastable phase, its surface can be easily reduced to form a Cr_2O_3 layer when exposed to air. Other barrier materials that have been investigated in CrO_2-based MTJs include various rutile oxides, such as TiO_2, RuO_2 and SnO_2.[81-83] However, there is no reported work on CrO_2-based junctions with VO_2 barrier. As mentioned in Chapter 4, the metal-insulator transition (MIT) property of VO_2 can be exploited for introducing new device functionalities.

In this chapter, MTJs with a natural barrier layer ($CrO_2/Cr_2O_3/Co$) are fabricated as reference junctions to rule out any possible artifacts arising from the fabrication processing and measurement setup. Subsequently, CrO_2-based MTJs with VO_2 as the barrier layer ($CrO_2/VO_2/Co$) are fabricated using a similar method. Furthermore, their barrier height, transport and magnetic properties are investigated.

5.2 Device fabrication

The fabrication of the designed CrO_2-based MTJs is a multi-step process. Basically, there are three steps to fabricate the devices. The first step is to grow and pattern the bottom CrO_2 electrode on top of the TiO_2 (110) substrate. The VO_2 barrier layer is then deposited on top of the bottom electrode and the junction is defined by photolithography and ion milling. The last step is to grow and pattern the top Co electrode on top of the barrier layer. The details of the fabrication process is described in the following.

(1) Growth of bottom electrode

Before we deposit the bottom CrO_2 electrode on top of TiO_2 substrate, we first define the substrate by applying the first photomask with the bottom electrode patterns and the positive photoresist (PR) 1818. Then SiO_2 of about 60 nm thickness, an insulator used to separate the bottom and top electrode, is deposited by RF sputtering. The photoresist is lifted off using acetone as solent. Our process takes advantage of the selective growth of CrO_2. Since growth of CrO_2 is very sensitive to the substrate, its growth only occurs on top of the clean TiO_2 substrate, and no CrO_2 is grown on the SiO_2 surface. This selective growth process of the bottom CrO_2 electrode is shown in Fig. 34 (a).

(2) Define junctions

Defining junctions is a critical step during the fabrication process and can determine the device performance to a large extent. After the bottom CrO_2 electrode has been grown, the VO_2 barrier layer is deposited on top of it, and then defined by applying the second photomask with small junction patterns using the positive photoresist AZ 1818. The barrier layer, which is not covered by photoresist, is removed by ion milling. An additional SiO_2 layer of about 40 nm is grown for support and to ensure that the bottom and top electrode are electrically isolated. The photoresist is then removed by using acetone. The second step of defining junctions is shown in Fig. 34 (b).

(3) Growth of top electrode

The last step of the device fabrication process is to deposit and define the top Co electrode. In this step, a third photomask with top electrode patterns and photoresist AZ 5214 are used to define the top electrode. Co is then deposited by magnetron sputtering on top of the barrier layer. A capping layer of Ru is deposited to protect Co from oxidizing in the air. Finally, the photoresist and the film above it are lifted off. The third step of the top electrode growth is illustrated in Fig. 34 (c).

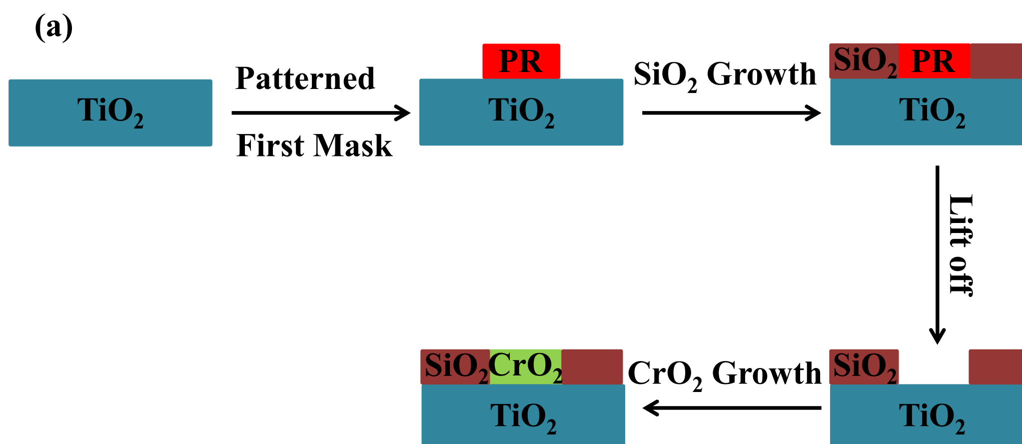

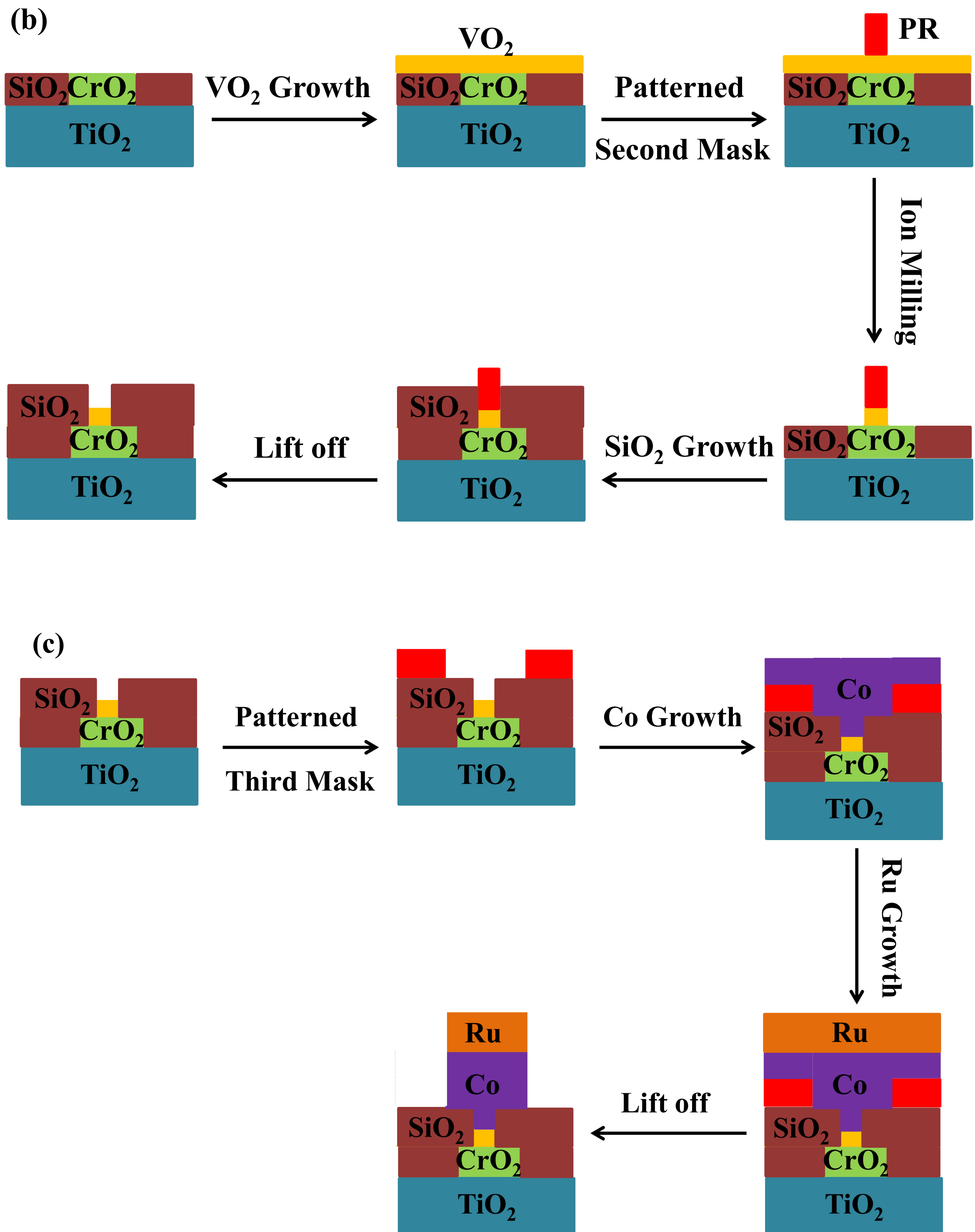

Figure 34. The fabrication process of the CrO_2-based MTJs (a) Growth of bottom electrode, (b) Define of junction and (c) Growth of top electrode.

5.3 Spin Transport in $CrO_2/Cr_2O_3/Co$ Junctions

The barrier layer Cr_2O_3 in the $CrO_2/Cr_2O_3/Co$ junction is antiferromagnetic with a Neel temperature of 307 K.[84] Since CrO_2 is a metastable phase, the more stable Cr_2O_3 phase can be grown on its surface naturally. In our fabrication process, a post-annealing step is used to speed up the growth rate of Cr_2O_3. The patterned CrO_2 sample is placed in one atmosphere oxygen environment at an annealing temperature of 450 °C for about 20 minutes to form a 3 nm Cr_2O_3 layer. In this thesis work, the thicknesses of the bottom (CrO_2) and top (Co) electrodes of the junctions are kept constant at 50 nm and 60 nm, respectively.

The bottom electrode resistance of the $CrO_2/Cr_2O_3/Co$ junction decreases with decreasing temperature, as shown in Fig. 35. The resistance of the electrode near room temperature (285 K) is about five times more than the resistance at liquid nitrogen temperature (78 K). The temperature dependence of the bottom electrode resistance is very similar to that of pure CrO_2 thin film, indicating that the metallic characteristic of CrO_2 is retained during the device fabrication process.

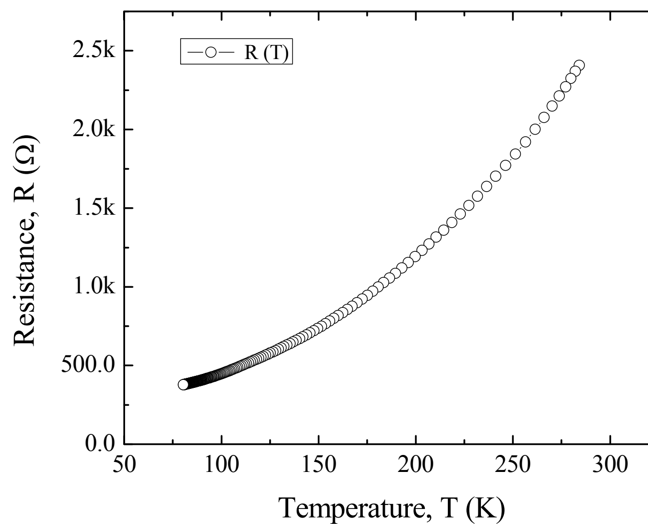

Figure 35. Temperature dependence of the bottom electrode resistance for $CrO_2(110)/Cr_2O_3/Co$ junction.

The temperature dependence of the junction resistance is shown in Fig. 36. The current is applied along the magnetocrystalline easy axis of a square-shaped junction with a dimension of 8×8 μm^2. The resistance of the junction increases as the temperature decreases, which is opposite to the bottom electrode's behavior and presents one signature of defect-mediated tunneling transport.

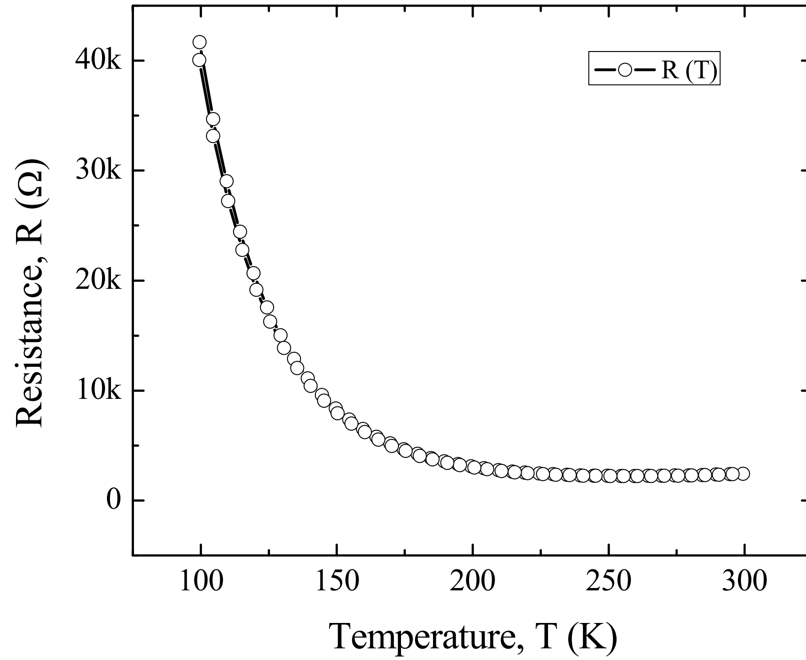

Figure 36. Temperature dependence of the junction resistance in a 8×8 μm^2 $CrO_2(110)/Cr_2O_3/Co$ junction.

The field dependence of the tunneling resistance in $CrO_2(110)/Cr_2O_3/Co$ junction with a dimension of 8×8 μm^2 is measured at 78 K with 1 mV bias. The TMR observed in this junction is about -1.2%, as shown in Fig. 37. This TMR value agrees well with the previously reported result [80], and thus rules out any possible artifacts resulting from the processing and measurement setup. The negative TMR suggests that lower resistance is obtained in the anti-parallel configuration of the junction. For negative TMR value to be exhibited, one of the electrodes must have negative spin polarization. As reported before, the spin polarization of

bottom CrO_2 electrode is about +98% at low temperatures.[37] Therefore, the negative TMR in the device is attributed to the spin polarization of the top Co electrode. The sign of the Co spin polarization depends on the selective tunneling of *s*- or *d*-electrons across the barrier layer. For *s*-electrons, the spin polarization of Co is about +40%, while it is about -80% for *d*-electrons.[85] Traditionally, it is believed that Co has positive spin polarization across Al_2O_3 barriers, in which pure *s* electron tunneling dominates. However, it has been confirmed that negative Co spin polarization can exist in $CrO_2/Cr_2O_3/Al_2O_3/Co$ junctions.[86] In these junctions, the combination of *s*- or *d*-electrons tunneling with different decay rates leads to about -40% spin polarization. It is the negative spin polarization of top Co electrode that leads to a negative TMR in our MTJ.

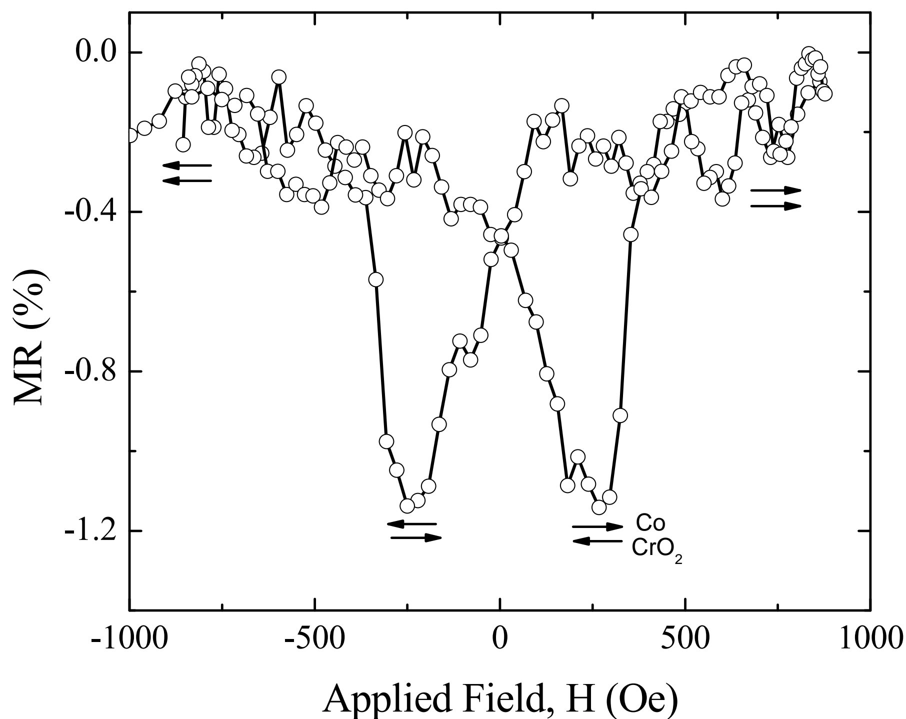

Figure 37. TMR of a 8×8 μm² $CrO_2(110)/Cr_2O_3/Co$ junction measured at 78 K.

Although oriented growth of Cr_2O_3 occurs on the CrO_2 bottom electrode, it is not a good choice as barrier layer for obtaining high TMR effects due to its anti-ferromagnetic property that

can lead to strong spin scattering. To better preserve the spin polarization in the tunneling process, MTJs based on non-magnetic VO_2 rutile oxide barrier layer, are fabricated, and their transport properties are investigated in the following section.

5.4 Spin transport in $CrO_2/VO_2/Co$ junctions

Rutile oxides are considered to be ideal candidates for barrier layer when constructing CrO_2-based MTJs due to their good structural compatibility with the bottom CrO_2 electrode. Many of the rutile oxides can grow epitaxially on CrO_2 and provide small interface roughness between the barrier layer and electrodes, which may result in higher TMR effects. A series of CrO_2-based MTJs with rutile oxide barrier have been reported, such as $CrO_2/TiO_2/CrO_2$, $CrO_2/SnO_2/Co$ and $CrO_2/RuO_2/CrO_2$.[81-83] However, no work has been reported on CrO_2-based MTJs with VO_2 barrier. As discussed in Chapter 4, VO_2 is a versatile material that exhibits a unique MIT behavior, which may provide new functionalities to the designed MTJs. In this section, the TMR and I-V characteristics, as well as M-H hysteresis loops of the CrO_2-based MTJs with VO_2 barrier, are investigated.

5.4.1. TMR

The resistance of the bottom electrode in $CrO_2/VO_2/Co$ junction increases as a function of temperature as shown in Fig. 38 (a), indicating a similar trend as in pure CrO_2 thin films as well as bottom electrode in $CrO_2/Cr_2O_3/Co$ MTJs. This observation indicates the metallic-like transport mechanism in the bottom CrO_2 electrode. In contrast, the resistance of the junction with a dimension of 8×8 μm^2 gradually decreases by a factor of about 26, from 78 K to 285 K, suggesting a tunneling-like transport across the barrier, as shown in Fig. 38 (b). It is worth noting

that a drop of resistance occurs around 340 K, the transition temperature of VO_2, which is an evidence of MIT in the barrier layer, as shown in the inset of Fig. 38.

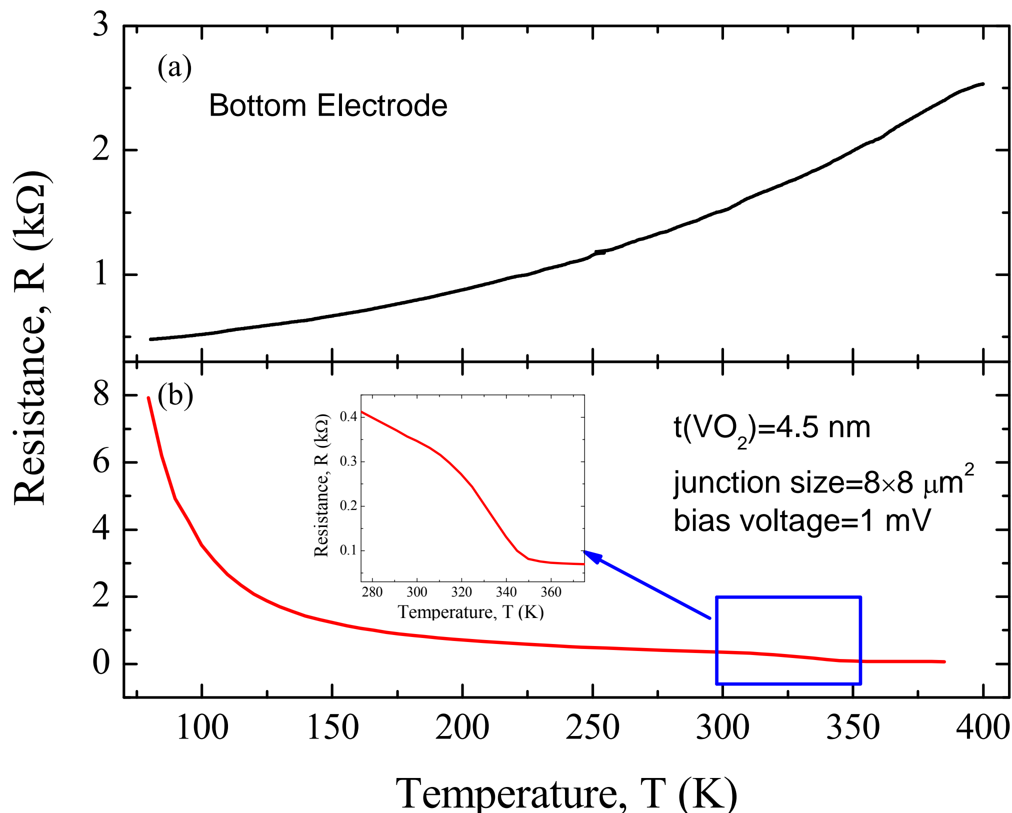

Figure 38. Bottom electrode and junction resistance of CrO_2/VO_2 (4.5 nm)/Co MTJ as a function of temperature. The insert shows a resistance drop around 340 K.

A TMR of about -2% (in a 8×8 μm^2 junction) is observed at 78 K with a DC bias of 0.4 mV applied along the easy axis of the junction, as shown in Fig. 39 (a). Since CrO_2 is a half-metal and has only majority electrons at the Fermi level, it possesses a positive spin polarization. Therefore, the negative resistance change of the junction is attributed to the negative spin polarization of the top Co electrode as in the CrO_2/Cr_2O_3/Co devices. However, as the applied bias is increased up to about 340 mV, the sign of TMR is reversed and a positive TMR of about 0.2% is observed, as shown in Fig. 39 (b).

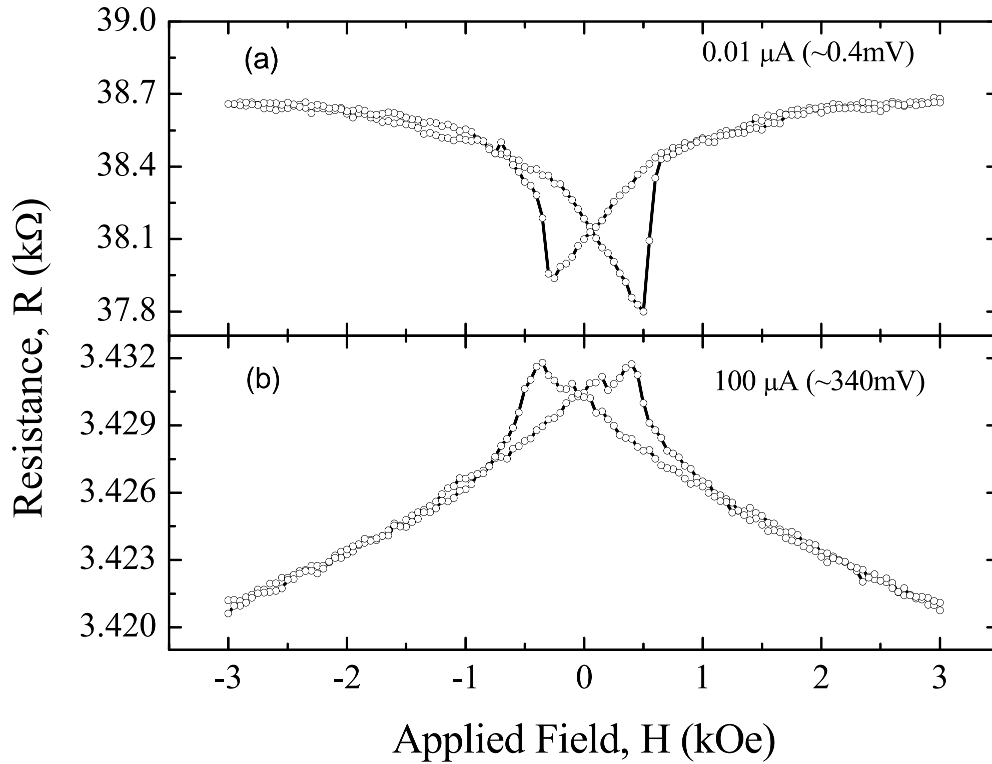

Figure 39. TMR of CrO_2/VO_2 (4.5 nm)/Co junction ($8\times8\ \mu m^2$) with applied voltage of (a) 0.4 mV and (b) 340 mV.

The bias dependence of TMR for MTJs with a 4.5 nm VO_2 barrier is shown in Fig. 40. In general, the TMR (negative) of the junction decreases with increasing applied bias voltage, and a TMR sign inversion (from negative to positive) occurs when the bias voltage reaches a specific threshold (about 125 mV in this case). The drop of TMR with bias voltage suggests that spin-flip scattering likely occurs inside the barrier or across the barrier-electrode interface.[87] In principle, the spin-flip scattering inside the barrier may be caused by impurities such as Cr ions or oxygen vacancies. The Cr ions can result from diffusion at the CrO_2/VO_2 interface, while the oxygen vacancies occur naturally in VO_2 barrier because of its semiconductor properties.[83] Due to the distribution of electrostatic potentials, the impurity energy levels are not fixed to one of the electrodes but float with the applied bias, which could lead to a TMR reversal when the

applied bias voltage exceeds a specific threshold.[88] The spin-flip scattering at interfaces mainly comes from magnon excitations. Since spin-flip processes are largely forbidden in the bottom CrO_2 electrode due to its half-metallic nature, the magnon excitation mainly arises from the top Co electrode. Another possibility is the shifting of Fermi level of one electrode relative to another due to the presence of a bias voltage. This shifting allows new states that are below the Fermi level to be accessed for tunneling. In this case, the spin polarization should relate to the integral of DOS of all accessible states instead of the DOS just on the Fermi level.[87, 88]

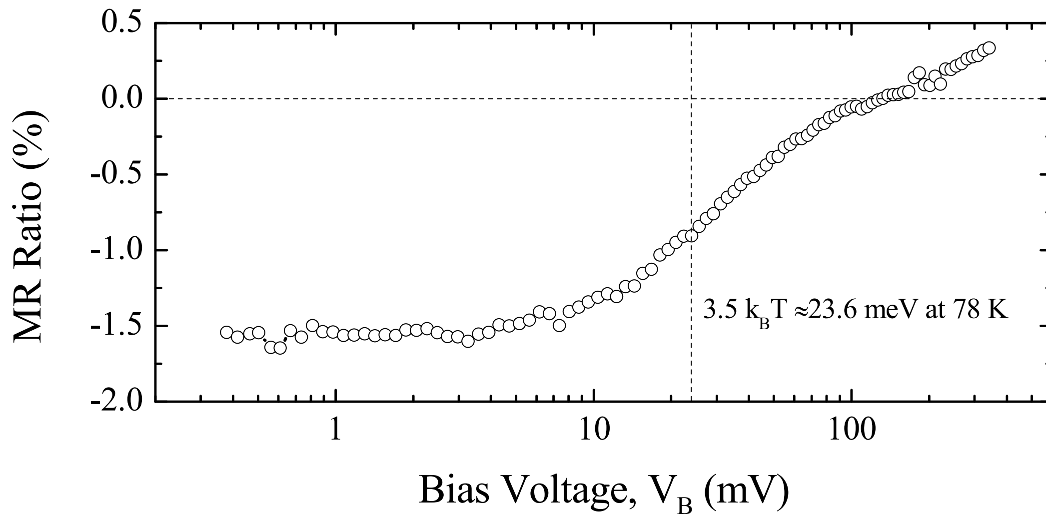

Figure 40. Bias dependence for a MTJs of 8×8 μm^2 with 4.5 nm epitaxial VO_2 barrier, at T=78 K.

The temperature dependence of TMR for $CrO_2/VO_2/Co$ MTJs with a 4.5 nm barrier is shown in Fig. 41. The highest TMR is about -5% at 4 K and the TMR value decreases to less than -1% at 100 K. When the temperature increases above 100 K, TMR for the junction becomes too small to be observed. The rapid drop of TMR with increasing temperature indicates strong spin-flip scattering process occurs at higher temperature. This drop-off behavior is very similar to that observed in $CrO_2/Cr_2O_3/Co$ junctions, which is generally considered as a result of magnetic disordering caused by thermal excitations of spin waves.[79]

If we assume the spin polarization of CrO_2 and Co are about 98% and -40%, respectively, the expected TMR for this junction should reach as high as about -57% according to the Julliere's model.[18] However, the TMR observed in our junction, even at 4 K, is far below the expected value. This is another evidence of strong spin-flip scattering process inside the barrier layer or across the interface, which can significantly reduce the TMR.

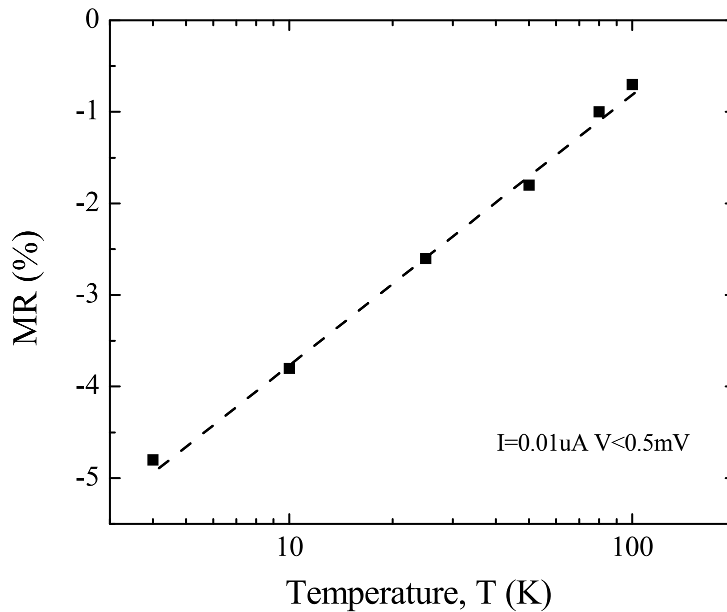

Figure 41. Temperature dependence for MTJs of 8×8 μm^2 with 4.5 nm epitaxial VO_2 barrier, for $V<0.5$ mV.

The TMR of the $CrO_2/VO_2/Co$ MTJs as a function of barrier layer thickness have also been investigated, as shown in Fig. 42 (a). As expected for tunneling, the junction resistance on a log scale increases almost linearly with the barrier thickness, as shown in Fig. 42 (b). The error bars represent the uncertainty in the thickness obtained from XRR measurements and junction resistance from R-T measurements. The highest TMR value is obtained when the barrier layer is about 4.2 nm. Subsequently, the TMR remains negative but decreases in magnitude as the VO_2

barrier thickness increases. When the barrier thickness reaches about 5.5 nm, the TMR reverses sign and has a small positive value.

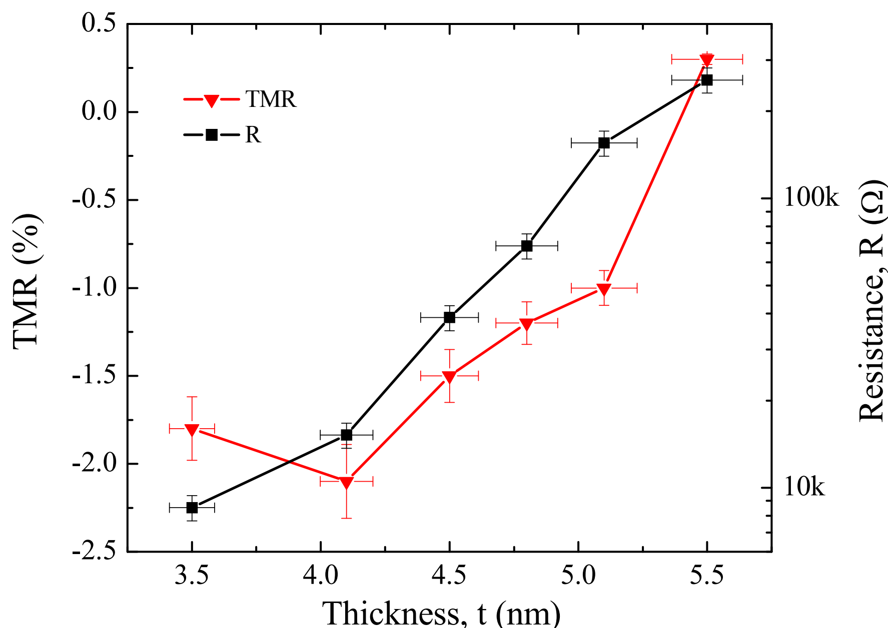

Figure 42. Thickness dependence of TMR in $CrO_2/VO_2/Co$ MTJs (8×8 μm^2), measured at 78 K with 1 mV bias voltage. The error bars represent the uncertainty of thickness obtained from XRR measurement and junction resistance from R-T measurement.

Although the underling mechanism is not very clear at this point, the TMR sign inversion as a function of thickness may be related to the properties of barrier and barrier-electrode interface. When the barrier thickness is low, there may still be part of the natural barrier Cr_2O_3 that is not completely covered by VO_2. The Co/Cr_2O_3 interface plays a major role and results in a negative spin polarization of Co due to the dominating *d*-like electrons through sdσ bonding at the Co/Cr_2O_3 interface.[83,88] On the other hand, the Co is in contact with VO_2 exclusively when the barrier thickness is high. The spin polarization of Co changes to a positive value likely due to the dominating *s*-like electrons through ssσ bonding Co/VO_2 interface. A similar behavior can be found in $CrO_2/SnO_2/Co$ junctions.[83] The thickness dependence of TMR in $CrO_2/VO_2/Co$

suggests that not only the amplitude of the spin polarization but even the sign of it are closely related to the barrier materials. Therefore, a detailed study of the barrier becomes important to gain a better understanding of the magnetoresistance properties of $CrO_2/VO_2/Co$ MTJs.

5.4.2. Barrier height

Studying the current through the device as a function of applied voltage (I-V curves), can provide valuable information about the tunneling characteristics of our $CrO_2/VO_2/Co$ junctions. Unlike ohmic resistors, a tunneling junction typically displays a nonlinear I-V curve. Fig. 43 illustrates a schematic energy diagram of the junction with zero bias, in which the energy levels of the two electrodes (CrO_2 and Co) are the same. Barrier height (φ) is the difference between potential at the surface and in the bulk of the barrier and is usually affected by the type of electrode with which the barrier is in contact. Barrier asymmetry ($\Delta\varphi$) is caused by the different work functions of CrO_2 and Co. The barrier thickness is noted as *d*. In this section, both Simmons [89] and Brinkman [90] models are applied to estimate the barrier height of $CrO_2/VO_2/Co$ junctions.

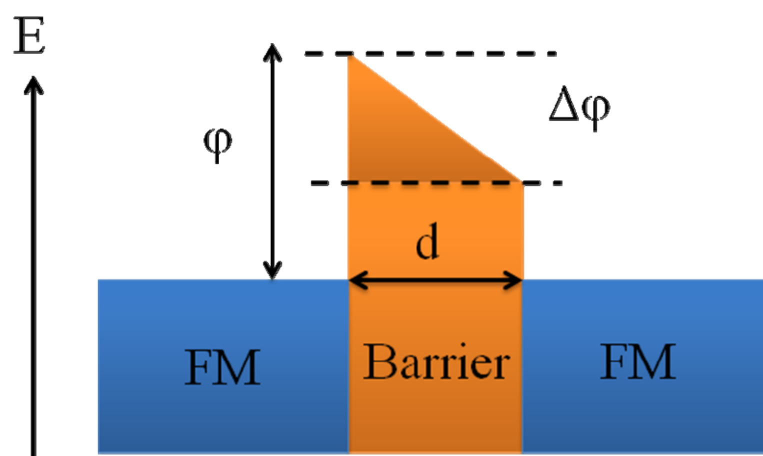

Figure 43. Schematic energy diagram with barrier height φ, barrier asymmetry Δφ and barrier thickness *d*.

The Simmons model [89] considers a rectangular-shaped barrier ($\Delta\varphi=0$) between the two ferromagnetic electrodes. A symmetrical conductance spectrum is expected for this model. In low bias condition, the current density J can be simplified as a polynomial function of bias voltage:

$$J = \beta(V + \gamma V^3) \tag{5.1}$$

where β and γ are constants and can be expressed as a function of barrier height φ (in eV) and barrier thickness d (in nm) of the junction:

$$\beta = \frac{3}{2d}\left(\frac{e}{\hbar}\right)^2 (2m\varphi)^{1/2} \exp\left[-\left(\frac{4\pi d}{\hbar}\right)(2m\varphi)^{1/2}\right] \tag{5.2}$$

$$\gamma = \frac{\pi m}{3\varphi(ed/\hbar)^2} \tag{5.3}$$

where m is the mass of electron and $\hbar$ is the reduced Planck's constant. The two constants β and γ can be obtained by fitting equation 5.1 to the experimental data, and thus φ and d can be calculated by solving both equation 5.2 and 5.3. For our $CrO_2/VO_2/Co$ junction, the current density against bias voltage is fitted poorly by the Simmons model as shown in Fig. 44. The barrier height and thickness are estimated to be 0.51 eV at 78 K and 3.0 nm by this method.

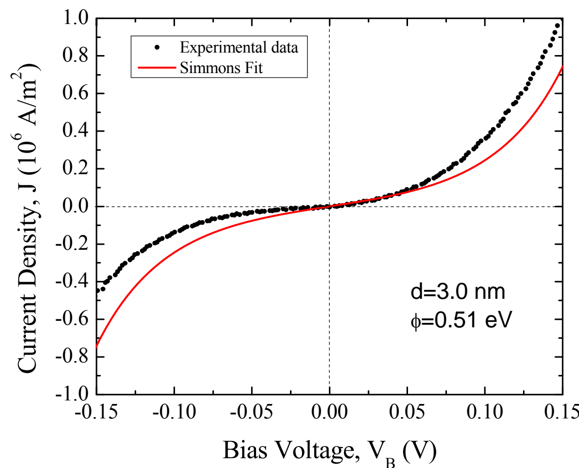

Figure 44. Simmons fitting of the current density against the bias voltage of a 8×8 μm^2 junction.

The poor fitting may result from the assumption in Simmons model that the barrier of the junction is symmetrical and has identical Fermi energies in the two ferromagnetic electrodes. In fact, there is an energy mismatch between the two Fermi levels of the electrodes (CrO_2 and Co) in our junctions. To address this issue, another model referred to as the Brinkman-Dynes and Rowel (BDR) model [90] is applied to estimate the barrier height and thickness for the asymmetric $CrO_2/VO_2/Co$ junction.

The Brinkman model assumes a trapezoidal-shaped barrier, which is more suitable for an asymmetric junction. For this model, the conductance of the junction can be expressed as:

$$\frac{dI}{dV} = A + BV + CV^2 \tag{5.4}$$

By integrating both sides of equation 5.4, the current against bias voltage can be obtained:

$$I = AV + B\frac{V^2}{2} + C\frac{V^3}{3} \tag{5.5}$$

where A, B and C are constants and can be obtained by fitting the experimental data. The barrier height and thickness can thus be calculated from these constants based on the following expressions:

$$d^2 = -5.368\sqrt{\frac{C}{A}}\ln(1.747\times 10^{-10}\sqrt{\frac{C}{A}}) \tag{5.5}$$

$$\varphi = 0.0328(\frac{A}{C})d^2 \tag{5.6}$$

The current of the junction as a function of bias voltage fitted by the Brinkman model is shown in Fig. 45. According to this model, φ and d are determined to be 0.12 eV and 5.4 nm. Similar values of φ and d (0. 14 eV and 5.0 nm), are obtained by fitting the conductance (extracted from the I-V curve) against bias voltage, as shown in Figure 46. Compared to the

Simmons model, the Brinkman model agrees quite well with the experimental data, primarily because the barrier asymmetry is captured by the quadratic term of the equation. The barrier asymmetry $\Delta\varphi$ from the two fittings are -0.062 eV and -0.060 eV, respectively. Based on the obtained results, effective barrier height ($\varphi+\Delta\varphi/2$) is calculated to be 0.11 eV and 0.09 eV. The low barrier height may be caused by the defects in the barrier, which is introduced by oxygen vacancies.

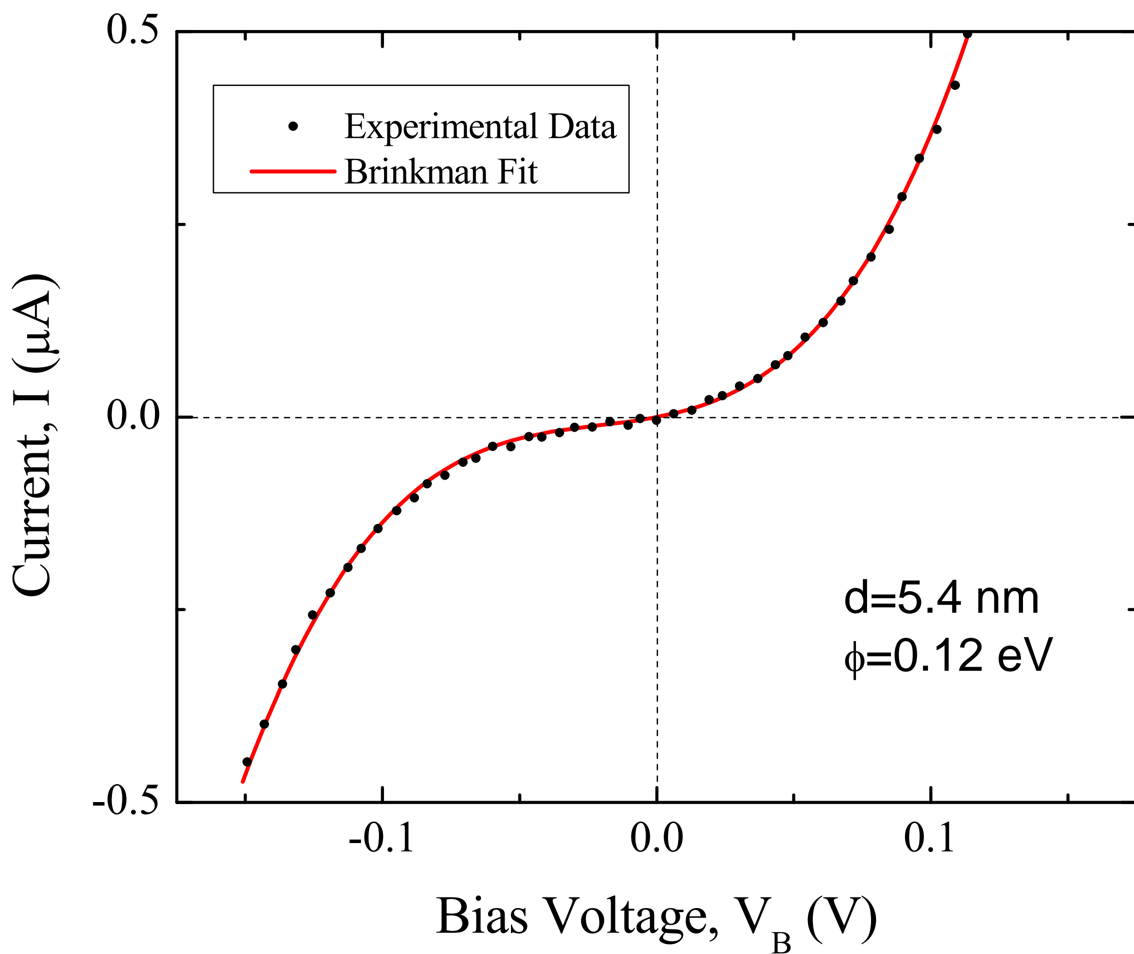

Figure 45. Brinkman fitting of the current against the bias voltage of a 8×8 μm^2 junction.

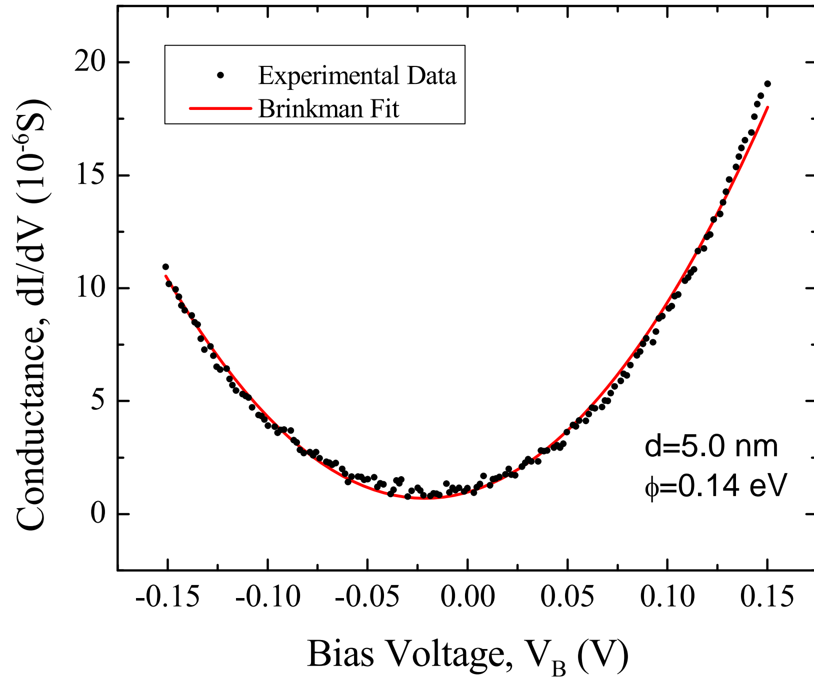

Figure 46. Brinkman fitting of the conductance against the bias voltage of a 8×8 μm^2 junction.

5.4.3. M-H loops

In order to verify that the bottom CrO_2 electrode and top Co electrode can switch independently, the magnetic characteristics of the CrO_2 (50 nm) /VO_2 (4.5 nm)/Co (60 nm) junction with a dimension of 8×8 μm^2 has been studied by the M-H hysteresis loops at different temperatures as shown in Fig. 47. As expected, the hysteresis loops of the junction at different temperatures display a double switching behavior. The switching fields for the top and bottom electrodes are different due to the different coercivity of CrO_2 and Co. The switching field of CrO_2 changes very little at different temperatures, indicating no or very small changes of the magnetic property of the bottom electrode. In contrast, the switching field of Co increases gradually as the temperature decreases and becomes asymmetrical below 150 K. The asymmetric switching field characteristics with decreasing temperature may result from partial oxidation of

the top Co electrode that produces an anti-ferromagnetic coupling. Partial intermixing between the Co electrode and the capping layer (Ru) possibly can also result in formation of an anti-ferromagnetic layer at the interface.

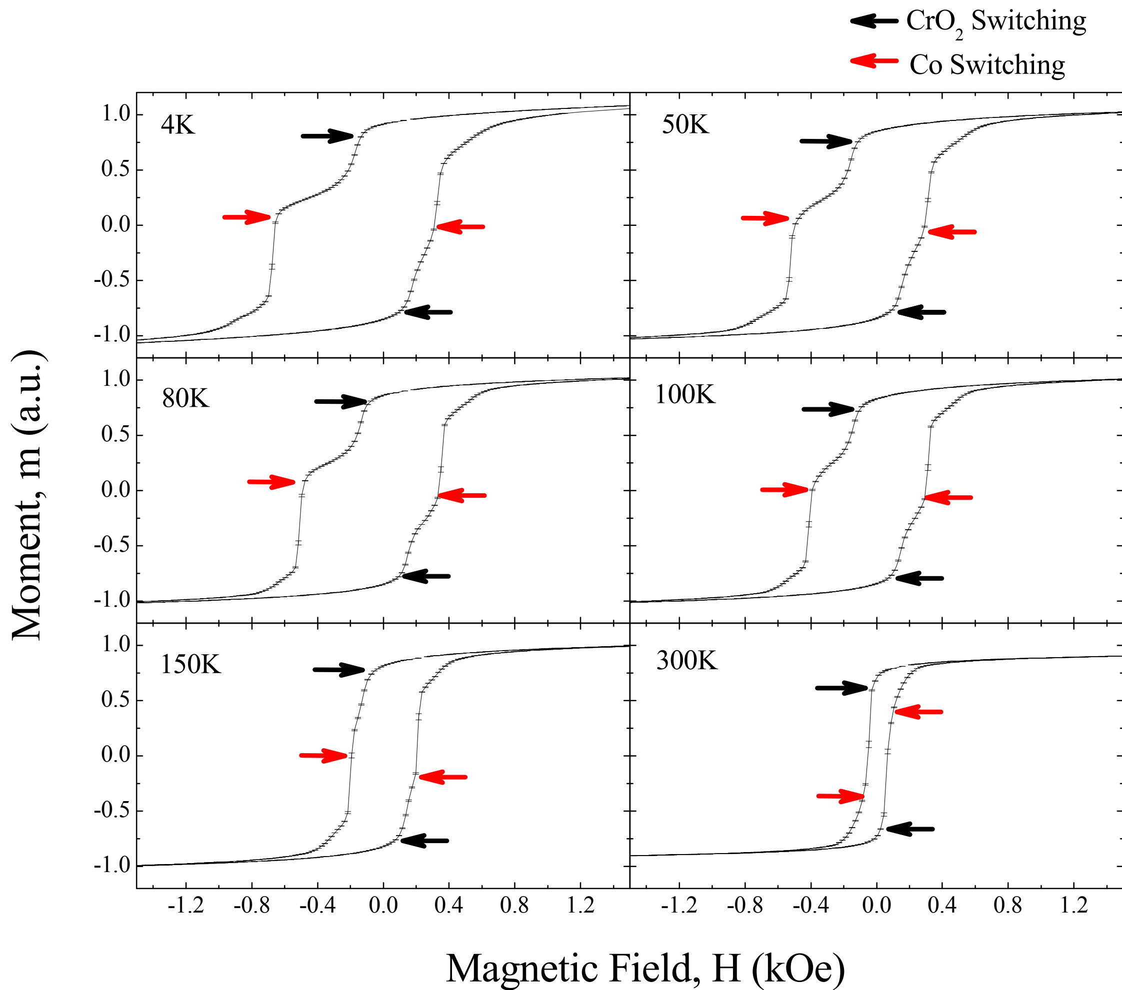

Figure 47. Hysteresis loops of $CrO_2/VO_2/Co$ junction at different temperatures.

5.5 Conclusion

In this chapter, both of the $CrO_2/Cr_2O_3/Co$ and $CrO_2/VO_2/Co$ MTJs have been successfully fabricated, and their transport properties have been studied. The results of our fabricated $CrO_2/Cr_2O_3/Co$ junction are comparable with the literature results, assuring no artifacts from the

complicated processing steps and measurement setup. The junction resistance of $CrO_2/VO_2/Co$ as a function of temperature shows a rapid drop of resistance around 340 K, the critical temperature of VO_2 thin film for metal-insulate transition. The bias dependence of TMR for the $CrO_2/VO_2/Co$ shows both the amplitude and sign of TMR are affected by the applied bias voltage. The TMR of the junction also displays strong temperature dependence. A TMR of about -5% is obtained when the temperature decreases to about 4 K. As the temperature increases, additional spin scattering events occur in the barrier and across the barrier interfaces, leadings to a rapid drop of TMR. Both the amplitude and the sign of the TMR of the junction also depend on the barrier thickness. The barrier height of the junction is estimated by two models, Simmons and Brinkman models. The Simmons model does not fit well with the experiment data due to its assumption of a symmetrical barrier. The Brinkman model is more realistic to estimate the barrier height of the $CrO_2/VO_2/Co$ junctions. Both the current and conductance versus bias voltage are fitted well by the Brinkman model. The barrier height obtained from the current and conductance fitting are very close to each other (0.12 eV in current fitting and 0.14 eV in conductance fitting). Double switching hysteresis loops of the junction are observed at different temperatures. The switching field of CrO_2 is nearly unaffected by the temperature. In contrast, the asymmetrical switching field of Co below 150 K suggests that partial oxidation of Co may have occurred during processing.

CHAPTER 6

SUMMARY

Spintronic devices with high magnetoresistance are desirable for the development of magnetic recording and memory technology. According to the Julliere's model, high spin polarization of the ferromagnetic layers is essential to enhancing the magnetoresistance effect of magnetic tunnel junction-based devices. In addition, the barrier layer of the tunnel junction plays a critical role in the spin-dependent tunneling processes. Therefore, the material choices for both the electrodes and the barrier layer are important for spintronic device research.

Chromium dioxide (CrO_2) is an experimentally confirmed half-metal with spin polarization as high as 98% at low temperatures. It is thus an ideal material for use as ferromagnetic electrode in investigating the properties of novel spintronic devices. In the first part of the thesis, I studied the structural and magnetic properties of CrO_2 thin films grown on TiO_2 substrates. Since CrO_2 thin films on (100) and (110)-oriented substrates have been investigated intensively in the previous work from our group, my work mainly focused on the CrO_2 thin films grown on TiO_2 (001) substrates to provide a systematic study of CrO_2 thin films grown on TiO_2 substrates of different orientations. Since the *c*-axis is perpendicular to the film, the structural and magnetic properties of CrO_2 (001) films are expected to be different from those of CrO_2 (100) and (110) films. Epitaxial CrO_2 (001) thin films have been successfully grown by our APCVD method. The CrO_2 (001) thin films are observed to be slightly expanded along the in-plane *a*- and *b*-axes but

compressed along the out-of-plane *c*-axis. The CrO_2 (001) films exhibit an out-of-plane magnetic hard axis due to the strong demagnetization effect. The out-of-plane magnetic behavior of the CrO_2 (001) thin films is studied using the simple Stoner-Wohlfarth model. Assuming a normal distribution of effective anisotropy field H_k^{eff} , the shape (K_d) and non-shape (both magnetocrystalline K_c and surface K_s) anisotropy are fitted. However, since the Stoner-Wohlfarth model neglects possible domain nucleation processes and interactions between grains within the films, it fails to explain the small hysteresis observed in the out-of-plane M-H loops and the high saturation field (over 1 kOe) in the in-plane M-H loops. The unexpectedly high saturation field of the in-plane hysteresis may result from stripes or vortex domain structures with an almost closed flux in the remanent state, which is not uncommon under the weak perpendicular anisotropy condition.

Vanadium dioxide (VO_2) can be switched between a metallic state and an insulating state by various means, including temperature change, optical irradiation, electric field or strain. In addition, VO_2 is closely lattice-matched with CrO_2 due to their similar rutile structure, and can thus be grown heteroepitaxially on top of CrO_2. These desirable features make VO_2 a promising material for use as the barrier layer in CrO_2-based MTJs. In the second part of this dissertation, we have successfully grown VO_2 thin films on (100), (110) and (001)-oriented TiO_2 substrates and have studied their transport properties. The lowest transition temperature (about 312 K) and largest resistance change (about 17000 times) during the MIT are observed in VO_2 (001) thin films, which can be explained by the compressive strain along the *c*-axis and the resulting increased width of *d* bands of V^{4+} ions. The growth of CrO_2/VO_2 heterostructures is a key step towards fabrication of magnetic tunnel junction devices, such as $CrO_2/VO_2/Co$. Since CrO_2 is a

metastable phase, it can be easily reduced to Cr_2O_3 when exposing to air. It is thus important to ensure that little or no decomposition of CrO_2 occurs during the VO_2 deposition when fabricating the CrO_2/VO_2 heterostructures. The magnetic hysteresis loops of the three differently oriented heterostructures show that the magnetization of only the CrO_2 (110) layer remains almost unchanged after VO_2 deposition, suggesting that TiO_2 (110) substrate is a better choice for device fabrication.

On the foundation of the first two parts, CrO_2-based magnetic tunnel junctions with Cr_2O_3 and VO_2 as barrier layers are fabricated, and their transport properties are investigated in the last part of work. To rule out any artifacts arising from the processing or measurement setup, $CrO_2/Cr_2O_3/Co$ junctions have been fabricated first as a reference since their magnetoresistance properties have previously been reported. Our CrO_2/Cr_2O_3-based junctions show the similar transport properties to those reported in the literature. We have subsequently fabricated $CrO_2/VO_2/Co$ junctions using a similar process and investigated their properties. The junction resistance of the $CrO_2/VO_2/Co$ device decreases as the temperature increases, suggestive of a defect-mediated tunneling process. The tunnel magnetoresistance (TMR) of the junctions show a strong bias voltage, temperature and barrier thickness dependence. As the applied bias voltage increases, the TMR of the junction decreases rapidly and shows a sign reversal when the bias voltage reaches a certain level. The TMR also shows a rapid drop with increasing temperature, indicating that spin scattering processes likely occur both inside the barrier and across the interfaces. The amplitude and the sign of the TMR also depend on the barrier thickness, suggesting the importance of the barrier materials. Two models, Simmons and Brinkman, are used to estimate the barrier height of the junctions. The Simmons model does not give a good

agreement with the experimental data because of its assumption of a symmetrical barrier. The Brinkman model is more realistic for our $CrO_2/VO_2/Co$ junctions and provides a good agreement with the experimental data. Using by the Brinkman model, the barrier height obtained from both the current and conductance vs. bias voltage curves (0.12 eV and 0.14 eV), are very close to each other. The magnetic hysteresis of the junction exhibits a double switching behavior due to the different coercivity of the two electrodes. The switching field changes little for the bottom CrO_2 electrode with different temperatures. In contrast, the switching field of the top Co electrode increases as the temperature decreases and shows an exchange bias effect below 150 K, suggesting that partial oxidation may have occurred at the Co surface.

In this dissertation work, we have studied the properties of two promising materials (CrO_2 and VO_2) and further used them in the fabrication of MTJs with intention of achieving high TMR effects. However, as shown in the work, the highest TMR of our $CrO_2/VO_2/Co$ junctions at 4 K is only about -5%, which is far below the prediction from the Julliere's model. From our work, it has been concluded that the transport property of junctions not only depends on the materials used for bottom electrode, but also on the property of barrier layer and interface between the barrier and electrodes. Although the barrier height of the junction has been estimated using two models, very limited interface information is obtained from the present work. In the future, more work can be focused on the characterization of the interfaces, such as using X-ray photoelectron spectroscopy (XPS) technique, to obtain surface information. The chemical nature of the barrier can be further studied by inelastic electron tunneling spectroscopy (IETS). It would be helpful to study the possible intermixing between the barrier and the bottom electrode by transmission

electron microscopy (TEM) and to obtain information about the structural transformation of the natural Cr_2O_3 layer on top of CrO_2 on deposition of VO_2.

REFERENCES

[1]. G.E.Uhlenbeck, S. Goudsmit, *Naturwissenschaften*, **1925**, 47, 953.

[2]. S. Goudsmit, G.E.Uhlenbeck, *Physica*, **1926**, 6, 273.

[3]. M.N. Baibich, J.M. Broto, A. Fert, F.N. Van Dau, F. Petroff, P. Etienne, G. Creuzet, A. Friederich, J. Chazelas, *Phys. Rev. Lett.*, **1988**, 61, 2472.

[4]. J. Barnaś, A. Fuss, R.E. Camley, P. Grünberg, W. Zinn, *Physical Review B*, **1990**, 42, 8110.

[5]. G.A. Prinz, *Physical Today*, **1995**, 48, 58.

[6]. S.A. Wolf, D.D. Awschalom, R.A. Buhrman, J.M. Daughton, S.v. Molnar, M.L. Roukes, A.Y. Chtchelkanova, D.M. Treger, *Science*, **2001**, 294, 1488.

[7]. I. Žutić, J. Fabian, S. Das Sarma, *Rev. Mod. Phys.*, **2004**, 76, 323.

[8]. I. Appelbaum, B. Huang, D.J. Monsma, *Nature*, **2007**, 447, 295.

[9]. J.S. Moodera, L.R. Kinder, T.M. Wong, R. Meservey, *Phys. Rev. Lett.*, **1995**, 74, 3273.

[10]. T. Miyazaki, N. Tezuka, *J. Magn. Magn. Mater.*, **1995**, 151, 403.

[11]. M. Tondra, J.M. Daughton, D. Wang, R.S. Beech, A. Fink, J.A. Taylor, *J. Appl. Phys.*, **1998**, 83, 6698.

[12]. S. Parkin, J. Xin, C. Kaiser, A. Panchula, K. Roche, M. Samant, *Proc. IEEE*, **2003**, 91, 661.

[13]. S.S.P. Parkin, M. Hayashi, L. Thomas, *Science*, **2008**, 320, 190.

[14]. M.I. Dyakonov, ed. S.S.i.S.S. Science. 2008: Springer-Verlag Berlin Heidelberg.

[15]. N.F. Mott, *Proc. Roy. Soc.*, **1936**, 156, 368.

[16]. T. Valet, A. Fert, *Physical Review B*, **1993**, 48, 7099.

[17]. G. Binasch, P. Grünberg, F. Saurenbach, W. Zinn, *Physical Review B*, **1989**, 39, 4828.

[18]. M. Julliere, *Phys. Lett. A*, **1975**, 54, 225.

[19]. T. Miyazaki, N. Tezuka, *J. Magn. Magn. Mater.*, **1995**, 139, L231.

[20]. W.H. Butler, X.G. Zhang, T.C. Schulthess, J.M. MacLaren, *Physical Review B*, **2001**, 63, 054416.

[21]. J. Mathon, A. Umerski, *Physical Review B*, **2001**, 63, 220403.

[22]. M. Bowen, V. Cros, F. Petroff, A. Fert, C.M. Boubeta, J.L. Costa-Kramer, J.V. Anguita, A. Cebollada, F. Briones, J.M. de Teresa, L. Morellon, M.R. Ibarra, F. Guell, F. Peiro, A. Cornet, *Appl. Phys. Lett.*, **2001**, 79, 1655.

[23]. S. Yuasa, T. Nagahama, A. Fukushima, Y. Suzuki, K. Ando, *Nat Mater*, **2004**, 3, 868.

[24]. S.S.P. Parkin, C. Kaiser, A. Panchula, P.M. Rice, B. Hughes, M. Samant, S.-H. Yang, *Nat Mater*, **2004**, 3, 862.

[25]. S. Ikeda, K. Miura, H. Yamamoto, K. Mizunuma, H.D. Gan, M. Endo, S. Kanai, J. Hayakawa, F. Matsukura, H. Ohno, *Nat Mater*, **2010**, 9, 721.

[26]. J. Daughton, J. Brown, E. Chen, R. Beech, A. Pohm, W. Kude, *IEEE Trans. Magn.*, **1994**, 30, 4608.

[27]. R. Meservey, P.M. Tedrow, *Phys. Rep.*, **1994**, 238, 173.

[28]. X. Jiang, R. Wang, S. van Dijken, R. Shelby, R. Macfarlane, G.S. Solomon, J. Harris, S.S.P. Parkin, *Phys. Rev. Lett.*, **2003**, 90, 256603.

[29]. X. Lou, C. Adelmann, S.A. Crooker, E.S. Garlid, J. Zhang, K.S.M. Reddy, S.D. Flexner, C.J. Palmstrom, P.A. Crowell, *Nat Phys*, **2007**, 3, 197.

[30]. B. Dieny, V.S. Speriosu, S. Metin, S.S.P. Parkin, B.A. Gurney, P. Baumgart, D.R. Wilhoit, *J. Appl. Phys.*, **1991**, 69, 4774.

[31]. S.S.P. Parkin, D. Mauri, *Physical Review B*, **1991**, 44, 7131.

[32]. J.W.F. Egelhoff, P.J. Chen, C.J. Powell, D. Parks, G. Serpa, R.D. McMichael, D. Martien, A.E. Berkowitz. *Specular electron scattering in metallic thin films*. 1999. San Diego, California (USA): AVS.

[33]. D.C. Ralph, M.D. Stiles, *J. Magn. Magn. Mater.*, **2008**, 320, 1190.

[34]. G. Engels, J. Lange, T. Schäpers, H. Lüth, *Physical Review B*, **1997**, 55, R1958.

[35]. R.A. de Groot, F.M. Mueller, P.G.v. Engen, K.H.J. Buschow, *Phys. Rev. Lett.*, **1983**, 50, 2024.

[36]. A. Yanase, K. Siratori, *J. Phys. Soc. Jpn.*, **1984**, 53, 312.

[37]. K. Schwarzt, *J. Phys. F: Met. Phys.*, **1986**, 16, L211.

[38]. J.S. Parker, S.M. Watts, P.G. Ivanov, P. Xiong, *Phys. Rev. Lett.*, **2002**, 88, 196601.

[39]. A. Anguelouch, A. Gupta, G. Xiao, D.W. Abraham, Y. Ji, S. Ingvarsson, C.L. Chien, *Physical Review B*, **2001**, 64, 180408.

[40]. K.A. Yates, W.R. Branford, F. Magnus, Y. Miyoshi, B. Morris, L.F. Cohen, P.M. Sousa, O. Conde, A.J. Silvestre, *Appl. Phys. Lett.*, **2007**, 91, 172504.

[41]. F.J. Morin, *Phys. Rev. Lett.*, **1959**, 3, 34.

[42]. P.B. Allen, R.M. Wentzcovitch, W.W. Schulz, P.C. Canfield, *Physical Review B*, **1993**, 48, 4359.

[43]. J.B. Goodenough, *J. Solid State Chem.*, **1971**, 3, 490.

[44]. E.M. Heckman, L.P. Gonzalez, S. Guha, J.O. Barnes, A. Carpenter, *Thin Solid Films*, **2009**, 518, 265.

[45]. R. Balu, P.V. Ashrit, *Appl. Phys. Lett.*, **2008**, 92, 021904.

[46]. A. Pergament, A. Velichko, *Thin Solid Films*, **2010**, 518, 1760.

[47]. F.A. Chudnovskii, *Sov. Phys. Tech. Phys.*, **1976**, 20, 999.

[48]. S.J. Moss, A. Ledwith, *Chemistry of the Semiconductor Industry*. 1987: Springer.

[49]. S. Ishibashi, T. Namikawa, M. Satou, *Mater. Res. Bull.*, **1979**, 14, 51.

[50]. G. Miao, G. Xiao, A. Gupta, *Physical Review B*, **2005**, 71, 094418.

[51]. M.B. Sahana, G.N. Subbanna, S.A. Shivashankar, *J. Appl. Phys.*, **2002**, 92, 6495.

[52]. S.A. Campbell, *The Science and Engineering of Microelectronic Fabrication*. 2001: Oxford University Press.

[53]. C. Kittel, *Introduction to Solid State Physics*. 2004: Wiley.

[54]. M. Tolan, *X-ray Scattering from Soft-Matter Thin Films*. 1999: Springer.

[55]. J.S. Kouvel, D.S. Rodbell, *J. Appl. Phys.*, **1967**, 38, 979.

[56]. T. Leo, C. Kaiser, H. Yang, S.S.P. Parkin, M. Sperlich, G. Guntherodt, D.J. Smith, *Appl. Phys. Lett.*, **2007**, 91, 252506.

[57]. L. Chioncel, H. Allmaier, E. Arrigoni, A. Yamasaki, M. Daghofer, M.I. Katsnelson, A.I. Lichtenstein, *Physical Review B*, **2007**, 75, 140406.

[58]. X.W. Li, A. Gupta, G. Xiao, *Appl. Phys. Lett.*, **1999**, 75, 713.

[59]. F.Y. Yang, C.L. Chien, E.F. Ferrari, X.W. Li, G. Xiao, A. Gupta, *Appl. Phys. Lett.*, **2000**, 77, 286.

[60]. K.B. Chetry, M. Pathak, P. LeClair, A. Gupta, *J. Appl. Phys.*, **2009**, 105, 083925.

[61]. M. Pathak, H. Sato, X. Zhang, K.B. Chetry, D. Mazumdar, P. LeClair, A. Gupta, *J. Appl. Phys.*, **2010**, 108, 053713.

[62]. X. Huang, X.H. Yan, Z.H. Zhu, Y.R. Yang, Y.D. Guo, *J. Appl. Phys.*, **2011**, 109, 064319.

[63]. P.G. Ivanov, K.M. Bussmann, *J. Appl. Phys.*, **2009**, 105, 07B107.

[64]. W.H. Cloud, D.S. Schreiber, K.R. Babcock, *J. Appl. Phys.*, **1962**, 33, 1193.

[65]. J.M. Barandiaran, M. Vazquez, A. Hernando, J. Gonzalez, G. Rivero, *Magnetics, IEEE Transactions on*, **1989**, 25, 3330.

[66]. A. Savitzky, M.J.E. Golay, *Ana. Chem.*, **1964**, 36, 1627.

[67]. Z. Lu, P.B. Visscher, J.W. Harrell, *J. Appl. Phys.*, **2008**, 103, 07F507.

[68]. C. Walck, *Hand-book on statistical distributions for experimentalists*. **2007**: Internal Report SUF-PFY/96-01.

[69]. B. Cullity, C. Graham, *Introduction to Magnetic Materials* **2009**, Wiley-IEEE Press.

[70]. A. Hubert, R. Schafer, *Magnetic Domains*, **1998**, Springer.

[71]. C. Chappert, P. Bruno, *J. Appl. Phys.*, **1988**, 64, 5736.

[72]. A. Yamaguchi, S. Ogu, W.-H. Soe, R. Yamamoto, *Appl. Phys. Lett.*, **1993**, 62, 1020.

[73]. D.S. Rodbell, *J. Phys. Soc. Jpn.*, **1966**, 21, 1224.

[74]. E. Wohlfarth, *Handbook of Magnetic Materials: A Handbook on the Properties of Magnetically Ordered Substances*. **1980**: North-Holland.

[75]. J.J. Becker, *J. Appl. Phys.*, **1968**, 39, 1270.

[76]. N. Rama, M.S. Ramachandra Rao, *Solid State Commun.*, **2010**, 150, 1041.

[77]. A. Zylbersztejn, N.F. Mott, *Physical Review B*, **1975**, 11, 4383.

[78]. Y. Muraoka, Z. Hiroi, *Appl. Phys. Lett.*, **2002**, 80, 583.

[79]. A. Gupta, X.W. Li, G. Xiao, *Appl. Phys. Lett.*, **2001**, 78, 1894.

[80]. M. Pathak, D. Mazumdar, V. Karthik, X. Zhang, K.B. Chetry, S. Keshavarz, P. LeClair, A. Gupta, *J. Appl. Phys.*, **2011**, 110, 053708.

[81]. A.M. Bratkovsky, *Appl. Phys. Lett.*, **1998**, 72, 2334.

[82]. G.X. Miao, A. Gupta, H. Sims, W.H. Butler, S. Ghosh, G. Xiao, *J. Appl. Phys.*, **2005**, 97, 10C924.

[83]. G.X. Miao, P. LeClair, A. Gupta, G. Xiao, M. Varela, S. Pennycook, *Appl. Phys. Lett.*, **2006**, 89, 022511.

[84]. T.R. McGuire, E.J. Scott, F.H. Grannis, *Physical Review*, **1956**, 102, 1000.

[85]. E.E. Fullerton, J.S. Jiang, S.D. Bader, *J. Magn. Magn. Mater.*, **1999**, 200, 392.

[86]. S. Cardoso, C. Cavaco, R. Ferreira, L. Pereira, M. Rickart, P.P. Freitas, N. Franco, J. Gouveia, N.P. Barradas, *J. Appl. Phys.*, **2005**, 97, 10C916.

[87]. J.S. Moodera, J. Nassar, G. Mathon, *Annu. Rev. Mater. Sci.*, **1999**, 29, 381.

[88]. E.Y. Tsymbal, A. Sokolov, I.F. Sabirianov, B. Doudin, *Phys. Rev. Lett.*, **2003**, 90, 186602.

[89]. J.G. Simmons, *J. Appl. Phys.*, **1963**, 34, 1793.

[90]. W.F. Brinkman, R.C. Dynes, J.M. Rowell, *J. Appl. Phys.*, **1970**, 41, 1915.